AREA PHOTOMETRY WITH
A MULTI-DIODE ARRAY

by

STEFAN WLADYSLAW MOCHNACKI

B.Sc.(Hons.), University of Canterbury (N.Z.), 1970

M.Sc., University of Canterbury (N.Z.), 1971

A THESIS SUBMITTED IN PARTIAL FULFILLMENT OF

THE REQUIREMENTS FOR THE DEGREE OF

DOCTOR OF PHILOSOPHY

in

THE FACULTY OF GRADUATE STUDIES

(Department of Geophysics and Astronomy)

We accept this thesis as conforming

to the required standard

THE UNIVERSITY OF BRITISH COLUMBIA

October 1977

In presenting this thesis in partial fulfilment of the requirements for an advanced degree at the University of British Columbia, I agree that the Library shall make it freely available for reference and study. I further agree that permission for extensive copying of this thesis for scholarly purposes may be granted by the Head of my Department or by his representatives. It is understood that copying or publication of this thesis for financial gain shall not be allowed without my written permission.

Stefan Wladyslaw Mochnacki

Department of ASTRONOMY and GEOPHYSICS.

The University of British Columbia
2075 Wesbrook Place
Vancouver, Canada
V6T 1W5

Date 3 NOV. 1977.

ABSTRACT

An area photometer using a RETICON RA50x50 multi-diode array as the detector has been developed and used to observe the central regions of stellar systems. Computer programmes have been written to handle the recording of data and the subsequent analysis of images. A sequential image processing language called FIRM was developed for use with an IBM 370 under MTS. A theoretical analysis of the response of diode arrays to Gaussian star images shows that the light from a star can be integrated if the seeing diameter is greater than 2.0 times the diode centre to centre spacing. Aliasing at all frequencies is insignificant for any seeing diameter greater than about 2.5 diode spacings. Techniques for avoiding aliasing are discussed.

Images of an area approximately 40" x 40" in the centre of the Sb galaxy NGC 4736(=M94) have been obtained through blue, visual and red filters. Subtraction of a simple, circularly symmetric model with King core radius 6".0 ± 0".5 reveals a small, bar-like central structure about 20" across. This central structure is aligned perpendicularly to the major axis of the galaxy and melds into previously photographed spiral structure. A bright point-like nucleus is also seen, but it does not stand out in the colour maps. A sharp colour gradient exists at 10" radius. The reddest areas of the central region coincide roughly with patches of negative resi-

duals after model subtraction.

A simple dynamical model is constructed for the inner region of NGC 4736, and it is proposed that two spiral systems exist in this galaxy, one inside the other with the inner system rotating more rapidly if it is a two-armed spiral. This model may also apply to other galaxies. A central mass to blue luminosity ratio of 2.4 to 3.6 is obtained for a range of model parameters.

Observations of the X-ray emitting globular cluster NGC 7078(=M15) reveal a number of red giants within 15" of the centre. A map of b-r instrumental colour shows that the nuclear cusp appears to be only a little redder than the main unresolved "background" population of the cluster, but the poor seeing does not allow resolution of the cusp within 2" of the cluster centre. The colour map confirms published spectroscopic results. There is very little radial colour variation when centred circular apertures are simulated.

TABLE OF CONTENTS

LIST OF TABLES

LIST OF FIGURES

ACKNOWLEDGEMENT

This has been a long project, and many people have contributed to its completion. I wholeheartedly thank Dr. Gordon Walker, who has inspired and supervised this work, gently guiding me past rather numerous pitfalls during my tenure as a graduate student at UBC. His friendship and patience greatly contributed to making this time pleasant and, I trust, fruitful.

This project would not have been possible without the work of our electronics engineers Vern Buchholz, Dave Lane--Wright and Barclay Isherwood. Dieter Schreiber worked beyond the call of duty in the fabrication of mechanical components.

Dr. Jason Auman's persistent and thought-provoking questions motivated Chapter 3. Drs. Chris Pritchet and John Kormendy in the course of discussions taught me much about galaxies, while Drs. Tad Ulrych, Greg Fahlman and Paul Sommerville cleared away the mists of frequency space. Drs. John Glaspey and Ingemar Olson introduced me to minicomputer programming and I thank them for the use of some subroutines. Alfonso Condal willingly shared some telescope time and assisted with the observations.

Dr. Brent Tully made it possible for me to observe with him at Mauna Kea, and I thank the Institute for Astronomy at

the University of Hawaii for making their facilities available. I am very grateful to the Dominion Astrophysical Observatory, Victoria, for extensive use of their facilities. I offer no thanks to the weather, which flings rain and snow whenever I touch a telescope.

Special thanks go to Dr. John Galt and all the staff at the Dominion Radio Astrophysical Observatory, Penticton, for assistance with graphics. The outstanding service of the UBC Computing Centre is gratefully acknowledged.

I thank the University of British Columbia, and Dr. Walter Gage in particular, for the tenure of a University Fellowship.

Last, but not least, I thank my wife Kathy for her encouragement and support under trying conditions. To her I dedicate this thesis.

To Kathy

CHAPTER 1

INTRODUCTION

1.1 The Observation of Extended Systems.

Astronomical objects such as gaseous nebulae, galactic and globular star clusters, galaxies and clusters of galaxies can be studied largely from two points of view:

(i) The physical conditions and constitution of the different components of extended objects can be deduced by analysing the radiation from these objects. Examples of such studies are photometry and spectroscopy for abundance analysis and population synthesis, X-ray , infra-red and radio observations to deduce the physical nature of components, area photometry for structural mapping and so forth.

(ii) The dynamics of the components of extended objects can be studied to deduce the distribution of matter and the interaction of the components within the object. Motions in extended objects are usually observed by measuring only radial velocities, although it is possible to measure tangential (proper) motions in some nearby objects such as the Hyades cluster and the Crab Nebula to obtain a complete kinematic description.

The constitution and the dynamics of extended systems are in fact very closely intertwined. In particular I shall

consider objects in which the distribution and nature of luminous matter is powerfully governed by large-scale dynamics involving very many components. These objects are globular clusters and galaxies. Globular clusters are self-gravitating ensembles of 10^4 to 10^7 stars orbiting in the halos of galaxies, which in turn contain a total of up to 10^{13} stars. I shall ask the following question : can the projected two-dimensional brightness distributions in galaxies and globular clusters be observed and used to understand their dynamics, and vice versa?

1.2 Structure Of Globular Clusters.

Of the estimated 190±30 globular clusters in our Galaxy (Harris 1976), over 100 have been studied in greater or lesser detail (see Peterson and King 1975, Peterson 1976 for summaries). The distribution of stars has been obtained by counting individual resolved stars on plates (King *et al.* 1968; Illingworth and Illingworth 1976; Peterson 1976) and by photoelectric area photometry (King 1963, 1966b; Illingworth and Illingworth 1976; Chun 1976).

King (1962) derived an empirical relationship for the surface brightness of globular clusters . For large tidal radius , this gives $I(r) \propto r^{-2}$, analogous to Hubble's surface brightness law for galaxies.

The masses of a number of globular clusters have been

inferred from observations of velocity dispersions (Illingworth and Illingworth 1974 and references therein). A vast literature on the photometry of individual stars in globular clusters exists, but is largely outside the scope of this work.

The collection of new data in the past ten years has coincided with the development of a much more thorough theoretical understanding of globular cluster dynamics. It was long understood that most globular clusters are relaxed or brought into near equilibrium by two-body interactions (e.g. Chandrasekhar 1942) and that some stars are expelled or "evaporate" (Spitzer and Harm 1958). However, it was not until the seminal work of Michie (1963 a,b) and King (1965, 1966a) that the space distribution of stars for a globular cluster model was computed allowing for a cut-off in the velocity distribution due to stars having escaped. Such a cut-off is observed in the form of a finite radius of the cluster; this radius is sometimes called the "tidal radius" because it is caused by the interaction between the potential fields of the cluster and of the Galaxy as the cluster orbits the within the halo of the Galaxy (von Hoerner 1957, with correction by King 1962). If there were no cut-off, and the velocity distribution were isotropically Gaussian, the infinite isothermal sphere would result (Chandrasekhar 1942), with $I(r) \propto r^{-1}$ for large r. Spitzer and Harm (1958) and King (1965) solved the Fokker-Planck equation to obtain the velo-

city distribution, and King (1966a) then solved Poisson's equation to derive the corresponding spatial distribution of stars within the cluster. This showed that a much steeper decrease of surface brightness was to be expected, depending on the tidal radius. Da Costa and Freeman (1976) have extended King's theory to allow for a realistic distribution of stellar masses with full equipartition of energy, whereas the earlier models assumed that the stars all had equal masses, or equivalently had energy proportional to mass. This allowed a total luminosity function to be estimated for a well-observed cluster such as M3, with a better fit to the surface brightness profile.

The surprising discovery of X-ray emission from five globular clusters (Giacconi et al., 1974; Clark, Markert and Li, 1975) has led to a search for unusual features in these clusters. It has been suggested that massive black holes may exist near their centres (e.g. Bahcall and Ostriker 1975). A number of theoretical studies have been undertaken to consider the effects such an object would have upon the spatial distribution of stars at the centre of a globular cluster or elliptical galaxy (Wolfe and Burbidge 1970, Peebles 1972, Huntley and Saslaw 1975, Frank and Rees 1976, Bahcall and Wolf 1976). The most recent studies suggest that a central cusp in the density distribution should occur, with a power law variation $n(r) \propto r^{-7/4}$. A higher velocity dispersion in the cusp is also predicted. The work of Frank and Rees (1976) indicates

an observable angular extent of about one arc second for a thousand-solar-mass black hole at the centre of a typical globular cluster. Electronographic observations by Newell et al. (1976) suggest that such an object exists in the nucleus of the X-ray globular M15 (NGC 7078), and these authors have further developed the theoretical model of Da Costa and Freeman (1976) to compute the effects of the central object upon the entire cluster.

A number of models have been proposed for the source of X-rays in globular clusters. There are two main problems :

(i) Formation of a collapsed object,

(ii) Accumulation of matter to be accreted by the collapsed object.

The object is probably not a "simple" binary containing a collapsed component (Clark 1975), but rather a more massive object such as a black hole of 100 to 1000 solar masses (Silk and Arons 1975, Bahcall and Ostriker 1975). Coalescense of stars in the nucleus may be important (Hills and Day 1976). The discovery of giant X-ray pulses from sources, some of which may be associated with the X-ray globulars, has further complicated the situation (see Bahcall and Ostriker 1976 and references therein).

The problem of globular clusters retaining sufficient gas to fall onto a condensed object within a globular cluster has most recently been reviewed by Frank and Gisler (1976), who suggest that passage through a hot gaseous galactic halo

sweeps out the gas from all but a group of a few globular clusters which includes the X-ray globulars.

The problem of X-ray emission from globular clusters is still the subject of uncertainty and controversy. Clearly, more observations of different kinds are needed. Multi-cclour observations of M15 (NGC 7078) have been made using the RETICON area photometer and will be discussed in Chapter 5 .

1.3 Structure of Galaxies.

The structure of galaxies is much more complex than that of globular clusters. The essential difference is that whereas globular clusters are relaxed by two-body interactions, stars in galaxies are much more widely spaced and close encounters between individual stars are extremely rare (except perhaps in the most central regions) . Therefore galaxies cannot be relaxed by two-body interactions. This is called the "fundamental paradox of classical dynamics" by Ogorodnikov (1965, p.119) or "Zwicky's Paradox" by Lynden-Bell (1967). It is therefore surprising that a globular cluster model for the surface brightness distribution can fit a galaxy (King 1966a). Lynden-Bell (1967) has resolved this paradox by invoking the mechanism of violent relaxation. As an elliptical galaxy is formed, the smooth gravitational field due to the ensemble of already formed stars changes, thus changing the total energies of the stars.

The violent collapse process leads to a Maxwellian distribution of energy, but with temperature proportional to particle mass, i.e. no equipartition of energy between stars takes place. Lynden-Bell's model fits nicely into the galaxy formation theory of Gott and Thuan (1976), who postulate that if stellar formation is largely complete at the point of maximum collapse of a protogalaxy, an elliptical galaxy is formed. This depends on the initial conditions of protogalaxy formation and collapse. The Gott and Thuan (1976) model of galaxy formation seems to be a very interesting compromise of the debate between Larson(1975) and Gott(1975), supporting, respectively, collapse with dissipation and collapse (or infall) without dissipation.

The Gott-Thuan model has the following features:

(i) Protogalaxies are formed from density perturbations, which pick up angular momentum from tidal interactions with other protogalaxies about the time of maximum expansion (Peebles 1969).

(ii) More dense perturbations collapse more rapidly. The higher density leads to even more rapid star formation, which is essentially complete by the time of maximum collapse. An elliptical galaxy is formed.

(iii) Less dense density perturbations collapse more slowly with even slower star formation. The clouds of gas left over at the point of maximum collapse collide with dissipation of energy and eventually form a disk. The

stars formed early in the collapse form the bulge, or halo, and the ratio of the mass of the stellar spheroidal halo to that of the disk is determined by the ratio of the mass of stars to that of the gas at the point of maximum collapse.

(iv) The tidal interaction of protogalaxies leads to a similar initial distribution of angular momentum among protogalaxies of elliptical and spiral galaxies.

It can be seen that this picture of galaxy formation explains naturally the existence of two components in galaxies: a spheroidal halo or bulge, and a disk. In ellipticals the disk is absent or insignificant, although Larson(1975) considers that disks made up of metal-enriched stars may be important inside some ellipticals.

Observationally, disk and spheroidal components have characteristics common to nearly all galaxies. De Vaucouleurs(1959) found that the spheroidal component of spirals has the same empirical surface brightness law as ellipticals:

$$\log I(r) \propto r^{1/4}, \tag{1}$$

while the outer disk has:

$$I(r) \propto \exp(-\alpha r). \tag{2}$$

King (1966a) showed that de Vaucouleurs' law closely resembles his theoretical model with $\log_{10}(r_t/r_c) = 2.2$,

where r_t = tidal radius, r_c = core radius. This is the model which King showed to be appropriate for the elliptical galaxy NGC 3379.

It should be noted that no account has been taken of the "lens" or non-exponential disk seen in some galaxies by Freeman (1975) and Kormendy (1976). No account has been taken of the theoretical instability of "cold" disk systems in the absence of a massive halo (Peebles and Ostriker 1973), a problem of great importance in current galactic research.

Surface brightness measurements do not necessarily correspond to the distribution of mass because the mass-to-light ratio is a priori unknown. It is here that kinematic observations become very important, and it is also here that serious pitfalls occur.

Rotation curves , which correspond to measurements of radial velocity along the (apparent) major axes of galaxies, should in principle allow the determination of the run of density in rotating axisymmetric systems. The use of rotation curves to deduce the structure of external galaxies was pioneered by Burbidge et al. (1959) and Brandt (1960) using both optical and 21-centimetre radial velocity observations. The multiple-spheroid models of Burbidge et al. (1959), inspired by work on our own Galaxy by, for example, Schmidt (1956), were superseded by the spheroid-disk models of Toomre (1963) which have a relatively simple analytical form.

Some of the models used for fitting to radial velocity curves have been rather devoid of physical content and lack even an empirical basis. At the same time the observations have been too "noisy" and incomplete to reliably apply a true inversion technique.

A number of the earlier analytical models were reviewed by Perek (1962). It was not until Freeman's (1970) notable work on the disks of spiral galaxies that a model with an empirical basis was formulated for dynamical studies: the disk with an exponential surface density law. Spheroid and exponential disk models have been used by Nordsieck (1973a, b), Warner et al. (1973), Emerson and Baldwin (1973), Rots (1975), Yoshizawa and Wakamatsu (1975) and Monnet and Simien (1977). A large amount of work has been done using a combination of Toomre's (1963) disk model and the Burbidge et al. (1959) model for the spheroid, including the very important work on density waves (Shu et al. 1971; Roberts et al. 1975 and references therein). Unfortunately, the rotation curve in disks often reaches a maximum, or turnover, at about the limit of observations, leading to a large extrapolation for the outer unobserved region if a Toomre model is used (see Roberts 1975, Baldwin 1975). This extrapolation, combined with observations of low accuracy, led to the suggestion that the mass-to-luminosity ratio rises sharply in the outer regions of spiral galaxies. This question has been carefully examined by Warner et al. (1973),

Emerson and Baldwin (1973) and Baldwin (1975), who find little evidence for the mass-to-luminosity ratio varying by much in the disks of M31 (NGC 224) and M33 (NGC 598). However, more recent observations extending to further radii show that in some galaxies at least there really appears to be no turnover of the rotation curve, indicating a large amount of unseen matter at large radii (Roberts 1975; Krumm and Salpeter 1977).

Freeman (1970) pointed out that the B-V colour index shows little variation in the inter-arm regions of disks, and therefore concluded that the mass to blue light ratio does not change much across the disks of spirals. This has been strongly supported by the detailed photometry of six late spiral galaxies by Schweizer (1976). It is well known that element abundances in both the spheroidal and disk components show a radial variation in most galaxies (see van den Bergh 1975 for a review), and this could have some effect on the mass to luminosity ratios. Likewise the ratio of gas to stars changes radially in the disks of galaxies such as M33 (Warner et al. 1973). Nevertheless, as a starting point in this work it will be assumed that the mass to luminosity ratio is constant in the disk (excluding the arms which contain a very young, very luminous population in addition to the older disk population).

How does the mass to luminosity ratio of disks vary from galaxy to galaxy? The data are still very uncertain. Nordsieck (1973b) found that M/L decreased for later, bluer

galaxies, but this included the arm population. Schweizer (1976) found that the disk colours fell in a narrow range between B-V = +0.7 (typical of old galactic clusters) and B-V = +0.9 (typical of giant elliptical galaxies).

Freeman's (1970) remarkable result of a very narrow range of extrapolated central blue surface brightnesses for disks (B(0) = 21.65 ± 0.30 s.d.) would tend to suggest that the central surface density also has a small range. Freeman's result may be largely coincidental and only apparent due to superposition of the spheroid on the disk (Kormendy 1976). I shall tentatively accept Freeman's results since galaxies with little spheroidal contribution still display the exponential disk.

What can be said about the mass-to-luminosity ratios of spheroidal components? Two principal approaches have been used so far to deduce the masses and hence mass-to -luminosity ratios of elliptical galaxies and the bulges of spirals: population synthesis by fitting models to spectral scanner observations, and application of the virial theorem to measurements of the velocity dispersion. Optical rotation curves have also been used, and the limitations of this method will be discussed later. Recent applications of population synthesis methods (Faber 1971; O'Connell 1974, 1976; Pritchet 1975; Williams 1976; Turnrose 1976) demonstrate the great difficulty in determining the mass to luminosity ratio from spectrum scans over a limited range of wavelenths: the light

is dominated by giants while the mass is dominated by dwarfs. This should not be a problem for velocity dispersion measurements, since the less massive stars should have the same velocity dispersion as the more massive ones except in the very densest nuclear regions of some galaxies (Lynden-Bell 1967). However, it is known that velocity dispersions at the centre of a galaxy may not be representative of the galaxy as a whole (Poveda 1958, Poveda et al. 1960, Morton and Chevalier 1972, Aarseth and Saslaw 1972). Wilson (1975) has shown that using a more sophisticated model for elliptical galaxies, a sharp decrease of the velocity dispersion with distance away from the nucleus is to be expected and that elliptical galaxy masses may have been overestimated by a factor of three. Using a simpler model, Ruiz and Schwarzschild (1976) obtain a similar result for the bulges of spiral galaxies. Observations of this effect are still inconclusive, since the surface brightness drops off so rapidly away from the nucleus in spheroidal systems. Rotation curves for M94 (=NGC 4736) (Chincarini and Walker 1967), NGC 3115 (Williams 1975) and NGC 4697 (Bertola and Cappacioli 1975) have been measured without a significant change in velocity dispersion being noted. Faber and Jackson (1976) find a higher velocity dispersion in the nuclei of NGC 3115 and possibly in M31 than in the outer parts of these galaxies, but this may be due to the existence of a dynamically independent nucleus (Light et al. 1974, Ruiz 1976). The existence of multi-component spheroidal systems is especially important for

some barred systems (de Vaucouleurs 1974). The formation of a dynamically separate nucleus composed of normal stars may be due to the tidal disruption and accumulation of globular clusters with small initial perigalactica (Tremaine, Ostriker and Spitzer 1975; Tremaine 1976a,b).

Despite these difficulties, and the problems of deriving velocity dispersions from broadened composite spectral lines, application of Fourier transform techniques has allowed the systematic determination of masses and mass to luminosity ratios of the nuclear regions of a representative sample of galaxies (Faber and Jackson 1976; Sargent et al. 1977; Williams 1977). These authors find that the luminosity L is proportional to the velocity dispersion v to the fourth power:-

$$L \propto v^4 \quad . \tag{3}$$

Faber and Jackson (1976) find some evidence for a relationship:

$$\mathcal{M}/L_B \propto L_B^{\frac{1}{2}} \quad , \tag{4}$$

but Sargent et al. (1977) argue that relation (3) implies that all ellipticals have the same mean mass-to-luminosity ratio. Williams (1977) finds mass to luminosity ratios ranging from 1 to 15 , with similar ranges for spirals and ellipticals. The results to date, therefore, are still rather rough concerning the mean values of mass to luminosity ratio

for spheroidal systems, and very little indeed is known for the variation of M/L with radius, except that there are serious discrepancies between results from the galaxies themselves and from double and multiple (Turner 1976, Williams 1977).

The use of rotation curves could in principle allow the deduction of the distribution of density as a function of radius in a rotating spheroidal system (Burbidge et al. 1959). As noted earlier, this can work well using radial velocity observations of neutral and ionized hydrogen in the disks of spiral galaxies. However, there is a serious problem when one attempts to use the stellar absorption line radial velocities in a spheroidal system. In a disk system, the tangential (or orbital) velocity dominates, since the velocity dispersion is quite low and the orbital velocity is high, i.e. the disk is "cold" . In a spheroidal system, however, the radial motions are dominant, and hence the mean , or stream, velocity of stars near a point is less than the circular orbital velocity for that point. This has been made very clear by Ruiz and Schwarzschild (1976). It is therefore, necessary to fit a detailed model computed using techniques such as those of Prendergast and Tomer (1970), Wilson (1975) , Hunter (1975,1977), and Ruiz and Schwarzschild (1976). The mean rotation curve derived from stellar motions cannot be used as the circular orbital rotation curve. In fact, the concept of "pressure support" of Burbidge et al. (1959) as

outlined by Burbidge (1975) may apply more to stars than to the gas except in the very nucleus itself, since most of the gas in a rotating galaxy should be in a disk and rotating in a roughly circular path unless there is an outward motion of possibly explosive origin (see, for example , Sanders and Bania 1976). Pellet (1976) has observed a large difference between the absorption and emission line rotation curves for M31. Unfortunately, there is usually little gas, especially neutral hydrogen, in the inner regions of any but the latest Hubble types (Sc, Scd and IrrI ; see Faber and Gallagher (1976) for review and references) and until very recently radio observations of HI were of poor angular resolution. Therefore there is little reliable rotational velocity data on the inner regions of galaxies in general. Fabry-Perot mapping of emission-line velocities provides one way of approaching the problem (Tully 1972, 1974a,b,c), but the discrepancies between the HI measurements of the rotation curve of M31 and previous measurements using optical emission lines (Emerson and Baldwin 1973) suggest that great caution must be used when attempting to derive a circular velocity curve from an observed rotation curve. Tidal interactions are a further complication.

There is a further caveat. Even when constructing a sophisticated model along the lines of Wilson (1975), it is usually necessary to assume a form for the function statistically describing the motions of the stars, called the phase

distribution function. The actual motions depend critically on the process through which the galaxy was formed (Lynden-Bell 1967). It is well known that most forms adopted for the phase function have deficiences. Hunter (1975) has devised a method for obtaining a phase distribution once the mass distribution is known. But in order to know the mass distribution from the observed rotation curve using methods such as those of Wilson (1975) and Ruiz and Schwarzschild (1976) it is necessary to assume a form for the phase distribution function. The argument becomes circular. What other means are available to deduce the distribution of mass in a galaxy? Can area photometry and hydrogen gas rotation curves be combined with simple mass distribution models to produce a reasonable description of galaxies ?

The images of spiral galaxies contain much more information than images of elliptical galaxies at any wavelength. This is due to the presence of the flat disk. Not only does the disk allow the inclination to be determined in addition to a more precise determination of the mass distribution, but it is also the site of collective motions which produce spiral structure and continued star formation. The most developed model for spiral structure invokes density waves propagating radially in the stellar and gaseous disk to generate a quasi-stationary spiral structure rotating rigidly with constant angular velocity, (see Wielen 1974, Roberts 1974, and Lin 1975 for recent reviews).

The density-wave theory of spiral structure has been applied to observations of galaxies, and models have been obtained for a number of spiral galaxies (Shu *et al.* 1971, Roberts *et al.* 1975 and references therein).

A crucial feature of the density wave theory is the occurrence of resonant orbits called *Lindblad resonances.* In particular, the inner Linblad resonance may give rise to a "dispersion ring" which could cause observable effects such as optical line emission and radio continuum emission.

The consistency of density-wave phenomena with the mass distribution in dynamical models of galaxies can be tested by combining area photometry with other observations.

1.4 The Programme.

A number of galaxies and globular clusters were chosen for observation of their nuclear regions. The intensity and colour maps of these objects were to assist in the further understanding of some of the problems of the dynamics and structure of stellar systems as outlined in this chapter. Two objects, one galaxy and one globular cluster, were chosen for detailed study. The quality of the observations and the importance of the problems they raise are the principal motivations for the work presented here.

A camera using a multi-diode array as the detector was

constructed to carry out this programme. The design, construction and development of the RETICON camera will be described in Chapter 2.

In Chapter 3, I shall discuss theoretically the spatial frequency characteristics of multi-diode detectors, with special emphasis on the problem of aliasing. Data reduction and analysis techniques will also be presented.

Observations of the Sb galaxy NGC 4736(=M94) will be presented in Chapter 4, and a simple model will be described. In Chapter 5, I shall briefly discuss observations of the globular cluster NGC 7078(=M15), while Chapter 6 will summarize the results and outline a plan for future work.

Appendix I is a manual for using the author's image processing language FIRM , and Appendix II lists the objects observed using the RETICON camera, together with the locations of data on library tapes.

CHAPTER 2

INSTRUMENT DEVELOPMENT

2.1 Choice of Detector.

Images of extended astronomical objects have traditionally been recorded on photographic plates, from which photometric information is obtained by using microdensitometers. Unfortunately, photographic techniques are not very satisfactory when a very wide range of brightness levels has to be recorded over a small area, such as in the image of a galactic nucleus. The dynamic range and spatial characteristics of photographic emulsions are well known (see, for example, Dainty and Shaw 1974). An interesting attempt by Worden (1974) to obtain seeing-limited resolution colour maps for NGC 5194 (=M51) showed that accuracies in colour index of only ±0.2 magnitudes were possible without smoothing or averaging of microdensity data.

The quantum efficiency of conventional photographic emulsions is rather low, less than 1%. Long exposures are often needed, and the sensitivity drops as exposure time increases. This is called reciprocity failure. Recent advances, such as hydrogen hypersensitization, can increase sensitivity by up to twenty times by eliminating reciprocity failure (Babcock et al. 1974), while new fine-grained emulsions such as the Kodak IIIa-J increase the information

storage capacity of photographic plates.

Electronography as opposed to direct photography has been applied to galaxies (e.g. Ables and Ables 1972), but both the observation and reduction processes are extremely laborious. Automated digital microdensitometers such as the PDS allow new problems to be tackled using modern photographic and electronographic techniques. The outer regions of galaxies have been successfully studied photographically (e.g. Kormendy 1976), but the nuclear regions are much less accessible due to the low dynamic range and low photometric accuracy of photographic emulsions at high angular resolution.

Panoramic detectors have been developed to overcome some of these problems. A major goal of this work was to develop an electronic camera to study the nuclear regions of galaxies and globular clusters at high angular resolution and with high photometric accuracy. At the time this project was begun (1972), a number of workers were using low light level television cameras for two dimensional photometry (Livingston 1973, Glaspey and Walker 1973 and references therein). These cameras generally used electron reading beam signal generating tubes as detectors, e.g. orthocon, isocon, vidicon, SEC-vidicon, etc. A particularly productive system was the Princeton SEC-Vidicon camera (Zucchino and Lowrance 1971; Lowrance, Zucchino and Williams 1974), which has been successfully used for area photometry of galaxies (Crane 1973,1975). Experience with this and other systems indicates that serious

limitations on accuracy are imposed by using an electron beam to read out the signal from the photodetecting element of the camera tube. For example, this presented serious problems in calibrating the Celescope experiment on the orbiting satellite OAO-2 (Nozawa and Davis 1971).

(i) Raster scan fluctuations or "jitter". The exact position of a picture element is uncertain because the electron beam is affected by voltage fluctuations, magnetic fields, beam bending due to picture highlights, etc. The geometric instability of electron-beam readout devices limits the photometric accuracy.

(ii) Limited dynamic range. Camera tubes using electron emission from a photo-cathode surface often have a limited dynamic range, which can be compensated for by frequent scanning and averaging of the signal. This is not the case for the silicon diode vidicon, which does have a large dynamic range.

(iii) Limited resolution and oversampling. The electron beam has a finite cross-section, and therefore adjacent picture elements overlap. A situation called over-sampling usually results and introduces photometric uncertainty (Devinney, Fischel and Klinglesmith 1975; Fischel 1976). In some tubes, such as the isocon, the resulting picture element (or "pixel") is physically very large, with considerable overlap between elements (Buchholz 1972). Strong signals often lead to charge spreading and even poorer resolution. The electric

fields of strong highlights in the target can also bend the electron beam, causing geometrical distortions and hence photometric errors.

(iv) Non-linear response. In addition to a low dynamic range, many of the electron-beam readout tubes have a non-linear response which has to be carefully calibrated (Crane 1973).

(v) Beam-discharge lag. The photocathode or target of television cameras in many cases is not completely discharged by a single sweep of the electron beam, thus leaving a "memory" of the signal. Special scans are required between the taking of images to remove lag.

(vi) Threshold effects. Very low signals in many cases are not fully detected. This requires "preflashing" as part of a preparation cycle to set up a baseline above which the response is reasonably linear. This baseline is difficult to measure.

(vii) Large bulk and difficult cooling. Most panoramic detectors have to be cooled to reduce the dark signal. The large bulk and large photocathode area of some detectors require very elaborate cooling equipment (e.g. Goldberg 1973). Temperature stability is difficult to achieve.

(viii) Poor red response. Most camera tubes have a low quantum efficiency in the red and infra-red. The silicon diode vidicon and integrated silicon diode arrays overcome this deficiency.

(ix) Mechanical and photoelectric fragility. The vacuum-tube structure of conventional television-type detectors often can rather easily be broken. Internal elements can become loose, making the tube "microphonic". Exposure to daylight will ruin most tubes which employ amplification by electron emission, acceleration or bombardment. Silicon diode vidicons and arrays do not have this problem.

The RETICON RA50x50 integrated diode array (IDA) was chosen to be incorporated into an area photometer. It embodied proven technology and the instrumentation development group at UBC was already working with one dimensional RETICON arrays. The advantages and disadvantages of the RETICON array are listed in Table I. A good review of the use of integrated diode arrays in astronomy has been published by Livingston (1976), while Weckler (1975) has given a detailed review of their principles of operation.

The RETICON uses silicon p-n junction photodiodes operating in a photon flux integrating mode (Weckler 1967). The diodes are initially charged, at a reverse potential of about 5 volts. Incident photons generate charge carriers which discharge the diodes at a rate proportional to the photon flux. Further discharging is caused by thermal leakage. The diode is re-charged at the end of the integration period, and the amount of charge required measures the integrated photon flux.

TABLE I . Advantages and disadvantages of RETICON RA50x50 compared with electron beam readout tubes and other solid-state detectors (cf. Livingston 1976).

Advantages

- Large charge storage capacity and dynamic range.
- Geometric stability and uniformity.
- Smallness of sensor elements.
- Compact size of whole detector.
- Easily cooled and recycled.
- Low driving voltages: detector can be handled in daylight.
- No threshold.
- Excellent linearity of response.
- Low dark current when cooled to dry ice or liquid N_2 temperatures.
- Very high quantum efficiency, especially in the red and infra-red.
- Wide spectral useful response (4000-10,000A°).
- Low cross-talk between elements. Uniform diode response.
- Blue response higher than CCD and CID devices.

Disadvantages

- High video line capacity leading to high read-out noise.
- Small number of sensor elements.
- Opaque masking by conductors leading to "dead spaces" between diodes.
- Loss of near infra-red response at low temperatures (< -100°C).
- Low ultra-violet response compared with photo-electric devices.

The RETICON uses a double-FET "AND" gate as a switch with each diode in the array. Each photodiode is sequentially re-charged through a single video line by being individually switched one at a time into the video line, as shown in Figure 1 (see White 1976b). The charge pulse from each photodiode is amplified and digitized using external circuitry.

The main sources of noise in IDA detectors such as the RETICON have been summarized by White(1976a,b). These are Johnson-Nyquist or "kTC" noise, shot noise, and the preamplifier noise current. Because the RA50x50 has a high video line capacitance (100 to 200 pF), the preamplifier noise current is the principal source of noise in the system. The lowest noise to be expected is equivalent to about 2000 electrons or "charge carriers" per diode per readout.

2.2 System Design.

The design of the two-dimensional RETICON camera system followed the proven principles of the image isocon and linear RETICON systems developed at UBC (Buchholz *et al.* 1973, Walker *et al.* 1974, Walker *et al.* 1976). The detector electronics were developed by V.Buchholz, the digital electronics by D.Lane-Wright and B.Isherwood, and the mechanical and optical parts by the author. The computer software was developed by the author, with some subroutines written by B.I.Olson and J.W.Glaspey. The system is illustrated in block

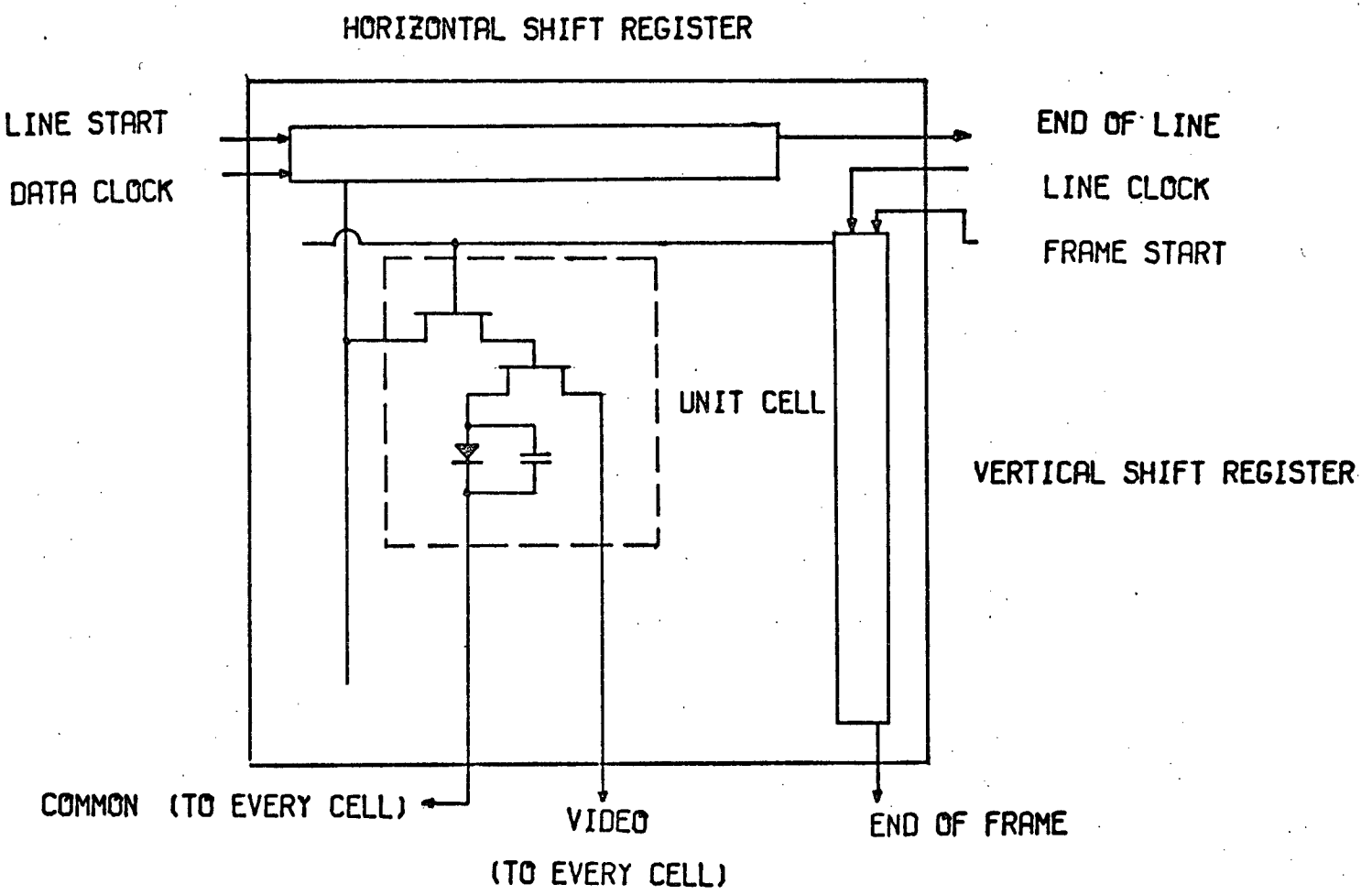

FIGURE 1. Schematic Circuit of RETICON two-dimensional diode array (after White 1976b, and Weckler, RETICON Corp.)

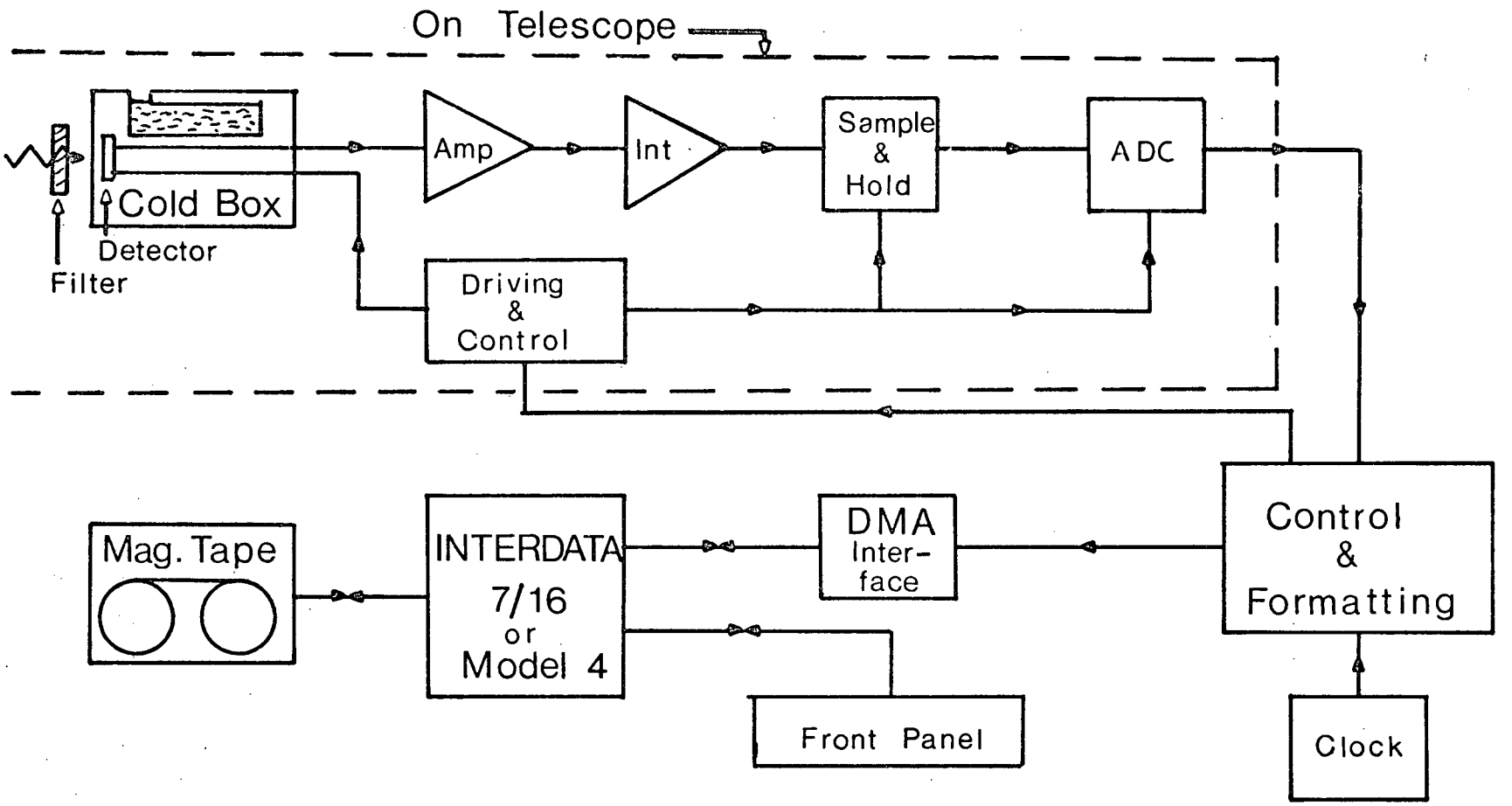

FIGURE 2. Schematic Diagram of Area Photometer.

diagram form in Figure 2.

Detector Housing and Cooling.

A standard Products for Research photomultiplier cold-box (PE-200-RF) was adapted to house the RETICON RA50x50. A cooling mixture of methanol and carbon-dioxide "dry ice" keeps the interior of the cold-box at a temperature of -76° Celsius at sea level. At the altitude of Mauna Kea, 4205 metres, the cooling slurry maintains a temperature of about -82°C. A heavy plug of epoxy doped with alumina was used to fill the space normally occupied by the photomultiplier. This plug was made so as to minimize electrical conduction and to maximize thermal conduction and thermal capacity. This was needed to minimize capacitative couplings and to maximize the temperature stability of the detector. Experience with the linear arrays had shown that the alumina-doped epoxy satisfied these requirements.

The alumina was mixed into the epoxy prior to hardening, in the proportions of 55% alumina, 34% epoxy resin and 11% hardener, by weight. The epoxy used was "Power-Bond A", produced by Industrial Formulators of Canada. The alumina was dehydrated by applying strong heat to the powdered alumina before mixing it into the resin. A fairly coarse grade of alumina was used to make the mixing easy.

The socket seating for the detector was fabricated at the

same time, with sixteen parallel conductors from the detector seat to the rear of the plug also cemented in the plug. The video line was shielded by using a thin coaxial cable and extra Teflon insulation. The amplifier and integrator were built into a compartment at the back of the cold-box, in the space normally occupied by the dynode resistor chain of a photo-electric photometer. The sample and hold, the 12-bit analog-to-digital converter (ADC) and some driving circuits were mounted in a container bolted to the side of the cold-box. Figure 3 shows the internal layout of the camera housing.

Before use, the camera must be flushed with dry nitrogen to prevent moisture condensation after dry ice is added to the methanol in the coolant compartment. Rubber ring seals were installed at the front and back of the camera. A plastic tube carries the incoming dry nitrogen to the front of the camera; the nitrogen then flows back through other tubes and holes to an exit pressure relief valve at the rear. Flushing for a half hour before cooling down has always proved adequate, and no frosting problems have been known to occur.

A double-pane quartz window is mounted in front of the RETICON , with a standard 3 watt heating coil on the front to prevent condensation. A simple filter slide arrangement bolts to the front of the cold-box, and the whole camera is bolted or screwed onto an adapter or offset guider, depending on the telescope on which it is being used. The UBC offset guider is

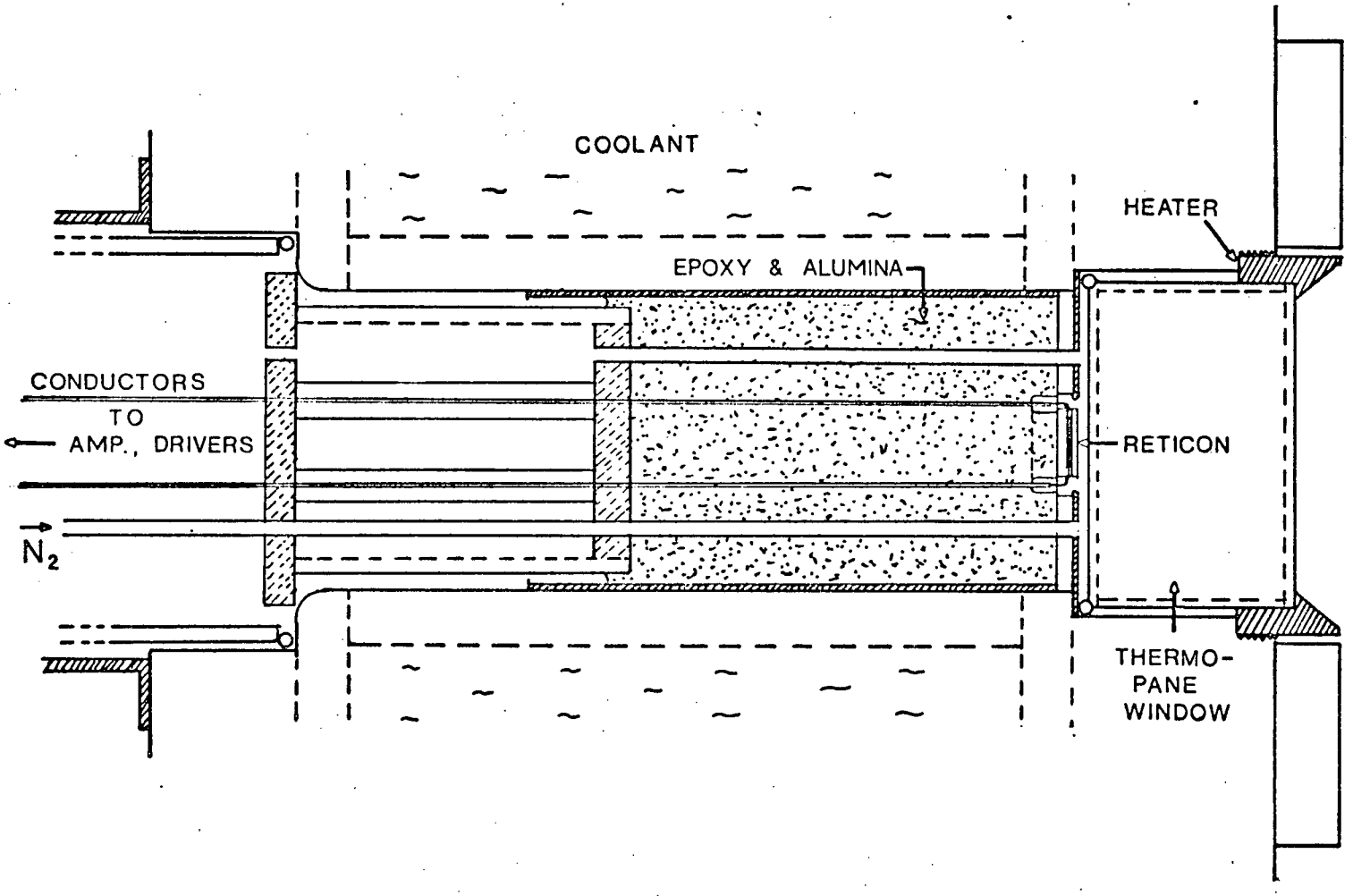

FIGURE 3. Internal Layout of Camera Housing (to scale).

used for setting the camera onto objects as well as for guiding.

Camera Control.

The UBC RETICON RA50x50 camera is controlled by a hard--wired unit which generates the clock and driving pulses and the exposure time (Walker et al. 1974). The scanning rate is 2KHz, so that an interval of 1.25 seconds is needed to read out the array. The control unit also has power supplies for the various voltages needed by the detector and associated circuitry. The reverse bias voltage for resetting the photodiodes is supplied by four rechargeable nickel-cadmium cells mounted at the side of the cold-box itself.

Data Acquisition.

The control unit also formats the serial output from the 12-bit ADC into 16-bit parallel form. Words of 16 bits per detector element are read into the core memory of an INTERDATA minicomputer via a direct memory access interface. The minicomputer has a passive role, accepting data under the control of the control unit. Once the full 2500 elements of an image have been read into core, the minicomputer records the data on 9-track magnetic tape and performs elementary on-line processing and display functions. The image is displayed in a dot-density format on an oscilloscope. Before a meaningful image can be displayed, the fixed pattern must be subtracted.

The fixed pattern is the fixed set of baseline signals which are caused by couplings between conductors in the camera and in the detector itself.

2.3 Operating Software.

Data acquisition is performed by an INTERDATA Model 4 or an INTERDATA 7/16 minicomputer. Since either of the minicomputers was sometimes unavailable, programmes were written and developed for both. The 7/16 has 16K bytes of core memory, allowing two images of 5000 bytes each to be stored in the core memory simultaneously. One of the images is a fixed pattern or dark measurement, which is subtracted from subsequent images in the other area of core. The result is displayed on an oscilloscope. Programmes written by the author were cross-assembled using a FORTRAN code produced by R.D.Russell for the IBM 360 or 370 operating under the Michigan Terminal System (MTS). The assembled machine-language programmes were loaded into the INTERDATA minicomputers via the same magnetic tape unit as used for recording the data.

The Model 4 has only 8K bytes of core, allowing only one image to be stored in core at a time. Starting with an idea found in the tape handler for BOSS, an INTERDATA operating system, I developed a technique whereby the fixed pattern or dark subtraction can be performed by reading data from the tape in single bytes. As the tape moves ahead at normal

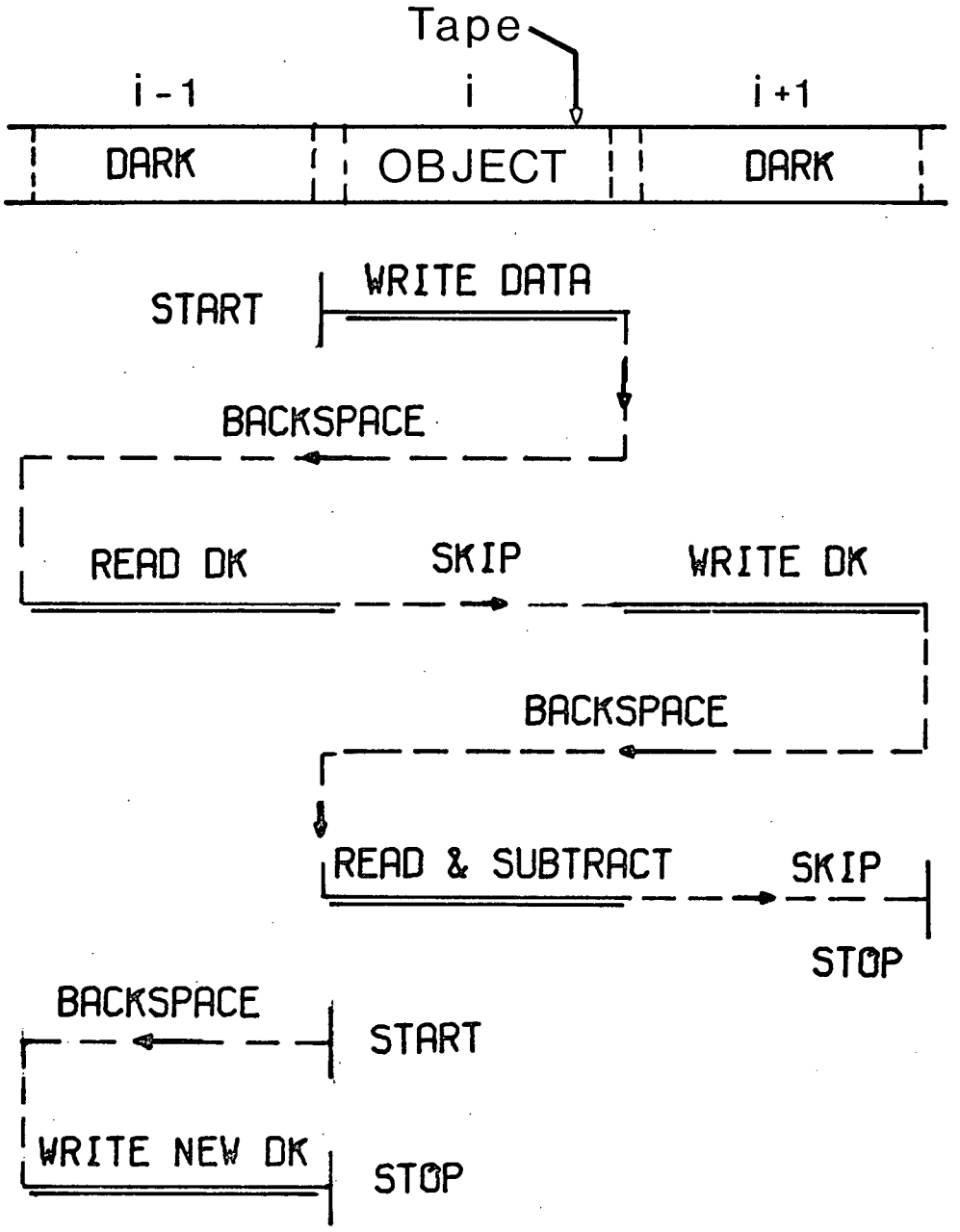

FIGURE 4. Recording of Data on Tape Using the INTERDATA Model 4. Small sequence at lower left is for recording a new dark or fixed pattern.

reading speed, intervals of time between the reading of bytes from the tape are occupied by calculations and manipulations, allowing the subtraction of the fixed pattern. Figure 4 shows the sequence of tape operations needed to write an image as one record on the tape. Table II shows an INTERDATA Assembler listing of the dynamic dark subtraction section of the Model 4 programme. It should be noted that the "dynamic subtraction" technique requires all interrupts to be disabled while the tape drive is moving. A similar technique has been used on the 7/16 for byte by byte verification of data after writing onto tape.

The 7/16 programme is based on the Model 4 code, but is simpler because it does not require an elaborate technique for subtracting the fixed pattern. Completion of a visual display unit and keyboard has permitted subsequent workers to add many useful interactive features to the observing programme.

2.4 System Performance.

The performance of the RETICON area photometer was evaluated from data taken during observing runs, and more detailed analyses are given in Chapters 4 and 5. Some characteristics are summarized in Table III . These and other characteristics are discussed below:

(i) Sensitivity: Using the "circular aperture" results from Chapters 4 and 5, sensitivities through the V passband were

TABLE II . Dark subtraction code for INTERDATA Model 4.

```
*  INTERDATA MODEL 4 CODE : RETICON AREA PHOTOMETER. *********
*
*  SECTION OF OBSERVING PROGRAMME : SUBTRACTION OF DARK. *****
*
*  SET UP REGISTERS FOR DYNAMIC SUBTRACTION OF DARK. *********
        LHI   R6,MTR       ADRS.OF 1ST BYTE LOOP.
        LHI   R12,BYTE2    ADRS.OF 2ND BYTE LOOP.
        LHI   R13,ARRAY    ADRS. OF ARRAY, AND COUNTER.
        LHI   R13,X'0002'  HALFWORD ADDRESS INCREMENT = 2.
        SHR   R13,R14      ALLOW FOR EXTRA HALFWORD.
*  SET UP REGISTERS BEFORE SKIPPING THE 40-BYTE LABEL. *******
        LHI   R8,MTDAT     LOAD  ADDRESS OF LABEL IN CORE.
        LHI   R9,X'0001'   LOAD BYTE ADDRESS INCREMENT.
        LHR   R10,R13      LOAD END HW. ADDRESS OF LABEL.
        AHR   R10,R9       INCREMENT TO GIVE END BYTE ADDRS.
*  READ & IGNORE THE 40 LABEL BYTES. **************************
        BAL   R15,WAIT     CALL "WAIT" TO STOP TAPE DRIVE.
        LHI   R15,ENDHW    LOAD END ADDRESS OF ARRAY.
        OC    MT,READ      START TAPE READING MOTION.
        SSR   MT,STAT      STILL BUSY OR READING A BYTE ?
        BTC   8,*-2        BRANCH BACK IF YES.
        RDR   MT,R7        READ  A  BYTE.
        BXLE  R8,*-8       LOOP BACK IF STILL IN LABEL.
        XHR   R8,R8        ZERO REGISTER(8).
*  DYNAMIC READING AND SUBTRACTION OF DARK CURRENT. **********
MTR     SSR   MT,STAT      STILL BUSY READING ?
        BTCR  8,R6         LOOP BACK IF STILL BUSY.
        RDR   MT,R7        READ FIRST BYTE OF A HALFWORD.
        STH   R8,0(R13)    STORE PREVIOUSLY COMBINED HALFWORD.
        SLHL  R7,8         SHIFT FIRST BYTE LEFT BY 8 BITS.
        AHR   R13,R14      INCREMENT ADDRESS COUNTER BY 2.
        LH    R10,0(R13)   LOAD DARK CURRENT VALUE INTO REG 13
BYTE2   SSR   MT,STAT      STILL BUSY READING ?
        BTCR  8,R12        LOOP BACK IF YES.
        RDR   MT,R8        READ THE SECOND BYTE OF HALFWORD.
        OHR   R8,R7        COMBINE FIST AND SECOND BYTES.
        SHR   R8,R10       SUBTRACT DARK CURRENT VALUE.
        CLHR  R13,R15      COMPARE COUNTER WITH FINAL ADDRESS
        BTCR  8,R6         BRANCH TO "MTR" IF COUNTER LOW.
*  EXIT FROM LOOP *****************************************
        STH   R8,0(R13)    STORE FINAL HALFWORD IN ARRAY.
*  TAPE DRIVE WILL STOP BY ITSELF NOW. ********************
*  CARRY ON WITH OTHER PROCESSING. ************************
```

TABLE III . Performance characteristics of RETICON area photometer.

Characteristic	Site	Numerical Value
Total Sensitivity in V Passband for V=0 object.	MKO	8×10^7 units/min.
	DAO	2×10^7 units/min.
Random Noise	MKO	±1.8units (s.d.)
	DAO	±1.8units (s.d.)
Baseline fluctuation	MKO	±3units (p.p.)
	DAO	±1unit (p.p.)
Average Dark Signal	DAO	0.3 units/min.
Maximum Dark Signal	DAO	5.2 units/min.
Fraction of Diodes with Dark > 2 x average.	DAO	3 %
Saturation Signal(approx.)		1000 units
Saturation Charge per Diode[1]		5×10^6 electrons

1. Manufacturer's specifications.

MKO: 2.2 Metre Cassegrain.

DAO: 1.8 Metre Broken Cassegrain.

obtained by comparison with published observations. Allowing for the different telescope sizes, the camera was about 2.5 times more sensitive on the 2.2 metre telescope at Mauna Kea than on the 1.8 metre telescope at Victoria. This difference was due partly to the arrangement and poor coating of the tertiary mirror in the 1.8 metre telescope, and partly to the difference in atmospheric extinction. Otherwise, the sensitivity difference is hard to explain.

(ii) Noise: The random diode to diode noise was 1.8 ADC units, or approximately 8000 electrons. A major contributor was digitization bit noise, since the analogue signal was observed to have a lower noise. An attempt to increase the gain without increasing the noise was unsuccessful at the time of the observations undertaken for this work. The problem was corrected later. The random noise is defined as the root mean square (r.m.s.) of the difference between two dark integrations of equal duration with average (baseline) drift being firstly removed. The noise for a single frame would therefore be $1/\sqrt{2}$ of this, but would not be very meaningful because the fixed pattern always must be subtracted.

The maximum possible signal to noise ratio at half saturation is therefore about 250, where only the random noise remaining after subtraction of a fixed pattern integration is considered.

The formal detective quantum efficiency, DQE, of the detector can be written as,

$$DQE = \left(S/n\right)^2_{out} \Big/ \left(S/n\right)^2_{in} \quad , \tag{5}$$

$$= \left\{ \frac{(\epsilon q P)^2}{\epsilon q P + \frac{N^2}{\langle MTF \rangle^2}} \right\} \Big/ \left\{ \frac{P^2}{P} \right\} \quad , \tag{6}$$

where:

ϵ = {sensitive area} / {total area} = 0.5,

q = quantum efficiency = 0.8(max.),

$\langle MTF \rangle$ = an average value of the MTF, such that $\langle MTF \rangle^{-2}$ is the effective number of diodes in a seeing image,

P = incident photon flux,

N = noise introduced by charge extraction and amplification.

For a star image with a diameter of 2 diode units, I assume $\langle MTF \rangle$=0.5. With N=8000 electrons, DQE = 0.06%, 0.6%, 1.5%, and 2.9% for P = 10^6, 10^7, 2.5×10^7 and 5×10^7 photons respectively. With ϵq =0.4 and $\langle MTF \rangle$=0.5, half saturation corresponds to 2.5×10^7 photons from a seeing-broadened point source incident upon the surface of the detector. For a continuous distribution rather than a star image, we have effectively $\langle MTF \rangle$=1.0 and at half saturation DQE=5.4%. The DQE at half saturation could be as high as 30% if the noise N were reduced to about 2000 electrons.

The present DQE is rather low because of the high

read-out and digitization noise. By comparison, the UBC Isocon system has a detective quantum efficiency of about 5% at 4100A°, and a silicon diode vidicon has been operated at a DQE of 1 to 2% (Buchholz et al. 1973). However, the RETICON has much higher dynamic range and red response than the Isocon, and it is geometrically and photometrically more stable than the Vidicon. These and other characteristics are not fully included in the DQE figure of merit discussed here.

(iii) Stability of the Baseline: The average fixed pattern fluctuated while the random diode to diode noise distribution remained constant. The baseline uncertainty between successive exposures was ±3 ADC units at Mauna Kea, ±1 unit at Victoria. Over periods of hours the baseline drifted by a few units in a non-uniform manner. The difference between two fixed-pattern exposures taken far apart sometimes looks like a grid of vertical bars. It is important to take fixed-pattern exposures frequently, or immediately after long exposures. Because the baseline fluctuation is of the same order of magnitude as the random noise, not much is to be gained from averaging a number of fixed-pattern integrations.

It was found that for integrations of less than one minute, the fixed pattern differed from longer fixed pattern integrations, indicating a settling time of about one minute. Thus observations of more than one minute exposure time required a one minute fixed pattern integration, while short observations of less than one minute required corresponding

fixed-pattern integrations <u>of the same duration.</u>

(iv) <u>Dark current:</u> A discussion of the measurements will be given in Chapter 5. At an indicated detector temperature of -76°C, the average dark current was 0.3 ADC units per minute, or about 25 charge carriers per second. About 3% of the diodes were "hot", having a dark signal rate of between 0.6 and 5.2 instrumental (ADC) units per minute.

For integrations of a half hour or less, the dark current rate was found to be constant within the limits of single measurements. This linearity is not expected for longer integrations or larger dark current rates (Weckler 1967, Dravins 1975).

(v) <u>Linearity:</u> Silicon diodes are known to have a very linear dependance of signal charge with respect to light intensity over a wide range when used in the integrating mode (Weckler 1967). One-dimensional RETICON arrays have generally been found to have a linearity of better than 1% up to the saturation level (Horlick and Codding 1973, Hog and Wiskott 1974, Buchholz 1974, Dravins 1975), and even to within 0.25% (Campbell 1977). The system developed for this work uses signal amplification and digitization circuitry very similar to that used by Buchholz (1974), while the manufacturer specifies the same linearity characteristics for the RA50x50 as for the linear arrays. I therefore assume that the device is linear within the errors of measurement. The "circular-aperture" results of Chapter 4, in particular, support this conclusion.

(vi) Flat field response: The large scale (edge to centre, or edge to edge) variation within the flat field calibration exposures was up to ±10% of the average signal. This depended on the telescope, the vignetting (if any), etc. The small scale (diode to diode) variation of about ±3%, which was greater than the random noise. This meant that the flat field calibration had to be applied diode by diode without smoothing or running averages. The dusk or dawn sky was generally used as the flat field. The short time during which the sky was of suitable brightness limited the number of exposures which could be summed to obtain an averaged flat field calibration through each filter.

(vii) Spatial frequency response: The spatial frequency characteristics of the detector will be given a full theoretical discussion in Chapter 3. The exact diode sensitivity profile is not very important for the fairly poor seeing of the observations reported in this work. A detailed laboratory study using a laser or other narrow beam of light has been carried out by Geary (1976) for a linear RETICON , but has not been attempted here. Star images are used to obtain the total transfer function or seeing profile, which includes instrumental effects. Observations at coarser plate scales show that charge spread or "blooming" is found only when charge saturation of diodes occurs. "Lag" or charge persistence after readout is also found only when saturation occurs.

Geary (1976) reported that at wavelengths beyond 9000A an

increase of the point spread function was to be found in RETICON detectors. This is not important here since only the B, V and R passbands have been used. The diode sensitivity profile becomes wider because at very low temperatures silicon becomes more transparent, excessively so at long wavelengths.

2.5 Optical Filters.

Broad-band absorption filters were chosen to reproduce as closely as possible the Johnson UBVRI passbands (Johnson 1965). The BVR combinations are listed in table IV . The manufacturers' curves were combined and compared with the curves published by Johnson, and the glasses were selected accordingly. The filter passband curves, including the RETICON response, are shown in Figure 5, together with the curves of Johnson (1965). The results of this work are insufficient to show whether the filter combination used here is superior to that chosen by de Lara et al. (1977) for a silicon diode photometer. More calibrated work with silicon diode photometers is needed to decide on the best choice of filters to approximate the Johnson system. An important problem is the presence of small red-leaks in the B and V passbands with the filters used here. The leaks are difficult to eliminate using standard absorption glasses without introducing a large amount of absorption within the desired passband. The wide spectral response of silicon diodes makes this a worse problem than in conventional photometry.

TABLE IV . Broad-band optical filters.

Pass-Band	CS or KG	Glass No.	Thickness m.m.	eff (1)	A (1)
B	CS-5-61	5562	5	4400	1100
V	CS-3-70 CS-4-97	3384 9788	4 5	5550	1050
R	CS-2-73 KG-3	2434	3 2	6600	1400

1. Filter transmission and detector response. (Based on manufacturers' data). Effective wavelength is middle of half-maxima points. Pass-band is wavelength interval between half-maxima points.

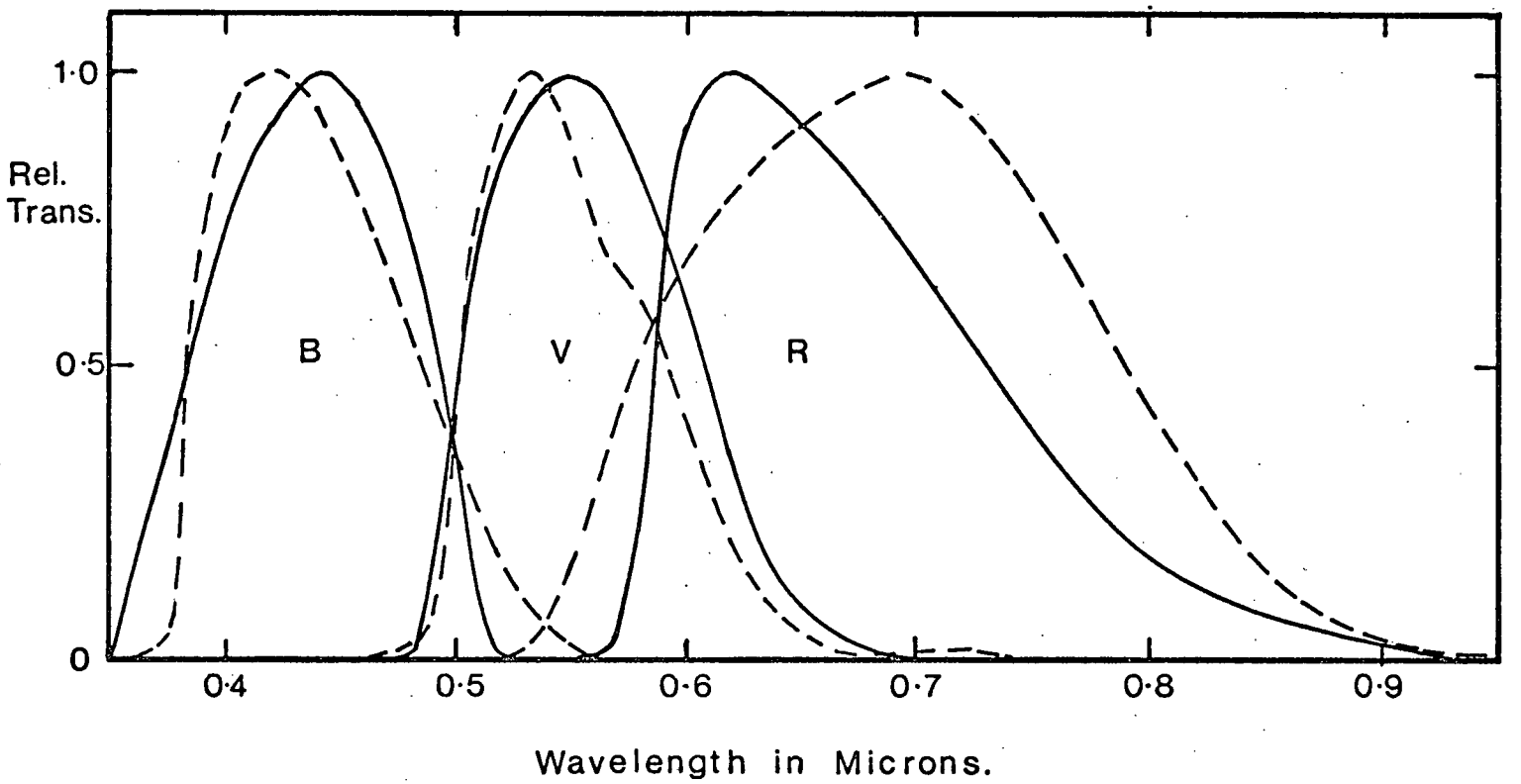

FIGURE 5. Optical filter passbands, combining manufacturers' data for filter transmission and RETICON response. Relative transmission plotted (solid line). Broken line represents standard curves of Johnson (1965).

CHAPTER 3

DATA ANALYSIS THEORY AND METHODS

3.1 General Concepts For Diode Arrays.

In addition to having greater geometrical stability than electron-beam readout detectors, the solid-state diode arrays such as the RETICON RA50x50 have much more discrete and better defined sampling elements. The spreading of the electron beam and other effects in conventional television cameras listed in Chapter 2 lead to an overlapping of sampling intervals resulting in "oversampling" (Fischel 1976). In devices such as the RETICON series of self-scanned arrays, there is much less spreading, and the overlap of sampling elements is complementary, i.e. the total charge extracted is proportional to the total incident light (Geary 1975).

The two-dimensional arrangement of the RA50x50 requires opaque metal conductors to lie alongside the silicon diodes, thus obscuring portions of the silicon substrate. This feature is also shared by the front-illuminated charge-coupled devices such as the Fairchild CCD211 (Fairchild Corp. 1976), but can be eliminated using the back-illuminated arrangement which, however, involves difficult fabrication methods (Antcliffe 1975).

While detailed laboratory measurements and calibration of the device would be most desirable, such a study is beyond the

scope of this work. Geary (1975), Buchholz *et al.* (1974) and Campbell (1976), among others, have found RETICON devices to be linear to better than 1% over their working range. Geary (1976) has measured the spatial sensitivity profile (or data window) of individual diodes in linear arrays, finding agreement with the manufacturer's 's specifications except at low temperatures (near liquid nitrogen) and at wavelengths greater than 9000 Angstroms. A theoretical study is outlined in the next section, suggesting ways of reducing errors in the taking of observations.

3.2 Theoretical Analysis Of Array Spatial Frequency Response.

The individual diodes of the RETICON RA50x50 are arranged in a square matrix, with separations of 4 mils (101.6 microns) between diodes in the X and Y dimensions. Approximately 50% of the total area is obscured by metal conductors. We shall assume for our theoretical model a centre-to-centre separation distance D, with each diode having a rectangular sensitive area a by b, with

$$0 < a \leq D, \quad 0 < b \leq D. \tag{7}$$

Without loss of generality, the sensitivity is assumed to be 100% in the live area and 0 over the dead area.

In two dimensions, the individual diode aperture can be represented by

$$d(x,y) = {}^{2}\Pi\left(\frac{x}{a}, \frac{y}{b}\right) = \Pi\left(\frac{x}{a}\right)\Pi\left(\frac{y}{b}\right), \qquad (8)$$

where Π is the box-car function (Bracewell 1959, p.243). The individual diode aperture function is the <u>data window</u> in this sampling problem.

If the individual diode "aperture function" cannot be represented by a simple box-car, but rather has a truncated pyramid shape, the higher frequency response will be more attenuated since extra "sinc" terms will be involved in the product in equation 20. Thus the rectangular "box-car" is probably a worst-case representation of the data window.

Most technical papers on television-type detectors employ the concepts of the square-wave amplitude response (SWAR), sinc-wave response, or point-spread function (PSF) to describe the spatial modulation transfer function (MTF). However, in astronomy resolution is normally limited by seeing or an optical instrumental function. We shall use a Gaussian representation for the seeing or optical profile, and observations described in Chapters 4 and 5 confirm the first-order accuracy of this approximation. The desirability of using a Gaussian instrumental function for this type of analysis has been pointed out by Anger <u>et al.</u> (1973), who treated a very similar problem involving a scanning auroral photometer. We define A as the <u>diameter</u> of the isophote for an intensity which is 1/e times the central intensity of the seeing profile

(or star image), which is represented by

$$i(x,y) = i(c,d)\exp\left[-\frac{4}{A^2}\left\{(x-c)^2+(y-d)^2\right\}\right], \quad (9)$$

where (c,d) is the position of the centre of the star image, as indicated in Figure 6. All features in an image prior to detection are convolved with the circularly symmetric normalized seeing function,

$$\Lambda(x,y) = \frac{4}{\pi A^2}\exp\left[-\frac{4}{A^2}\left(x^2+y^2\right)\right]. \quad (10)$$

The signal f(x,y) obtained from each diode can be thought of as the cross-correlation of the star image and the individual diode function d(x,y), the cross-correlation being sampled at discrete equi-spaced points which can be represented by an infinite two-dimensional Dirac comb, which is the product of two orthogonal one-dimensional Dirac combs,

$$^2\text{Ш}\left(\frac{x}{D},\frac{y}{D}\right) = \text{Ш}\left(\frac{x}{D}\right)\text{Ш}\left(\frac{y}{D}\right). \quad (11)$$

The effects of having a finite array will be discussed later. The signal (x,y) obtained by observing a Gaussian star image as given by equation (10) can therefore be written as :

$$f(x,y) = \int_{-\infty}^{+\infty}\int_{-\infty}^{+\infty} d(p-x,q-y)\,i(p,q)\,dq\,dp\;{}^2\text{Ш}\left(\frac{x}{D},\frac{y}{D}\right). \quad (12)$$

Now since the functions d(x,y) and i(x,y) are symmetric in x and y about their centres, we can replace the cross-correlation integral by the convolution integral:

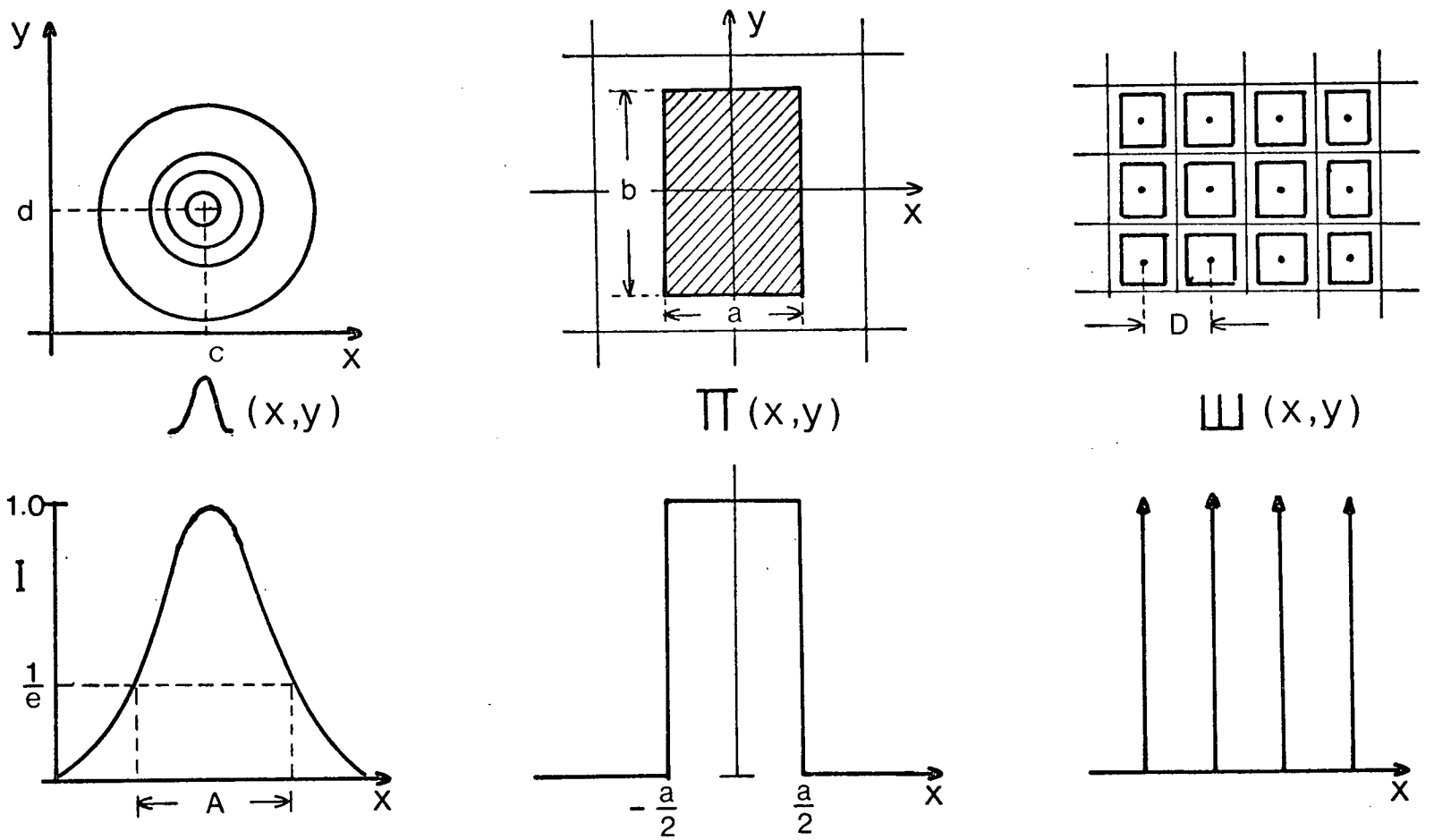

FIGURE 6. Detector sampling configuration, showing Gaussian star image, diode sampling window and diode array arrangement.

$$f(x,y) = \int_{-\infty}^{+\infty}\int_{-\infty}^{+\infty} d(x-p, y-q) . i(p,q)\, dq\, dp \;\; {}^{2}\text{Ш}\left(\frac{x}{D}, \frac{y}{D}\right), \tag{13}$$

$$= \left(d(x,y) * i(x,y) \right) . {}^{2}\text{Ш}\left(\frac{x}{D}, \frac{y}{D}\right). \tag{14}$$

which now has the same form as the expression used by Fischel (1976).

We need to obtain the spatial frequency response function as a function of seeing disk size A and diode spacing D, given the diode aperture dimensions (a,b) and "star" position (c,d). Applying the standard theorems (Bracewell, 1959, p.244), equation 14 is Fourier transformed to

$$F(u,v) = \left\{ D(u,v) . I(u,v) \right\} * {}^{2}\text{Ш}\left(Du, Dv\right), \tag{15}$$

where D (u,v) is the transform of the diode aperture function, and I(u,v) is the transform of the seeing profile or stellar image. We write,

$$R(u,v) = D(u,v) . I(u,v), \tag{16}$$

so that

$$F(u,v) = R(u,v) * {}^{2}\text{Ш}\left(Du, Dv\right). \tag{17}$$

The convolution with the shah symbol ${}^{2}\text{Ш}(Du, Dv)$ in the (u,v), or frequency, plane is a replication and local summation which is the mathematical form of <u>aliasing</u>. Equation (15) can be

written as

$$F(u,v) = \sum_{k=-\infty}^{+\infty} \sum_{m=-\infty}^{+\infty} R\left(u - \frac{k}{D}, v - \frac{m}{D}\right) . \qquad (18)$$

Without loss of generality, let us assume the value of the seeing profile is unity, i.e.

$$i(c,d) \int_0^\infty 2\pi r \exp\left(-\frac{4r^2}{A^2}\right) = \frac{\pi A^2}{4} i(c,d) = 1 . \qquad (19)$$

Then R(u,v) can be expanded as

$$R(u,v) = ab \exp\left\{-\frac{\pi A^2}{4}(u^2+v^2)\right\} .$$

$$. \exp\{-2\pi i(cu+dv)\} \operatorname{sinc}(au) \operatorname{sinc}(bv), \qquad (20)$$

where $\operatorname{sinc}(x) = \sin(\pi x)/(\pi x)$.

The finite size L by L of the detector can be expressed as a large box-car function in two dimensions multiplying the sample, so that the sample can be written as

$$f_L(x,y) = \left(d(x,y) * i(x,y)\right) . {}^2\text{Ш}\left(\frac{x}{D}, \frac{y}{D}\right) . {}^2\Pi\left(\frac{x}{L}, \frac{y}{L}\right) . \qquad (21)$$

The finite length sample $f_L(x,y)$ transforms to,

$$F_L(u,v) = \{D(u,v) \cdot I(u,v)\} * {}^2\text{Ш}(Du, Dv) *$$

$$\{L^2 \cdot \text{sinc}(Lu)\,\text{sinc}(Lv)\} . \tag{22}$$

Since L >> D, the sinc functions are very sharp and the convolution in frequency space will not appreciably broaden the Fourier transform. The finite size effect will be neglected from now on.

In general, F(u,v) as defined in equation (18) is a complex function. The <u>total</u> modulation transfer function (MTF) of the system, including both the seeing or optical profile and the detector geometry, can be called the Gaussian response function (GRF) and can be written as,

$$GRF(u,v) = \frac{|F(u,v)|}{R(0,0)} . \tag{23}$$

This includes the aliasing contribution. Indeed, the aliasing contribution $\delta F(u,v)$ at a point (u,v) in the frequency plane can be computed from,

$$\delta F(u,v) = F(u,v) - R(u,v) , \tag{24}$$

and so,

$$\delta GRF(u,v) = \frac{|\delta F(u,v)|}{R(0,0)} . \tag{25}$$

How can we determine when it is possible to do accurate photometry of a star observed with a diode array detector? Now,

$$F(0,0) = \int_{-\infty}^{+\infty}\int_{-\infty}^{+\infty} f(x,y)\,dx\,dy \quad , \tag{26}$$

i.e. the zero-frequency value of the transform of the sample is equal to the total integral of the sample. However, aliasing introduces errors into f(x,y), so a simple summation of the sample value $f(x_i , y_j)$ may not give a true measure of the total intensity in a stellar image. The value of $\delta GRF(0,0)$ provides a measure of the accuracy with which the flux from a star may be determined, so that $\delta GRF(0,0)$ can be called the <u>photometric error.</u> At higher frequencies, $\delta GRF(u,v)$ gives the aliasing error at (u,v). This will usually be worst at the Nyquist frequencies 1/(2D) .

A number of examples have been computed. Figure 7 shows the behaviour of GRF(u,o) for a=0.9, b=0.6, D=1.0 and several values of seeing diameter A.

Table V lists a corresponding set of values at the zero and Nyquist frequencies, with a comparison of the modulus of the unaliased Fourier transform R(u,v) with the aliased value |F(u,v)|.

How does the GRF depend on the position of the star image? Figure 8 shows a set of curves of GRF (u,v) for various displacements of the star image with respect to the

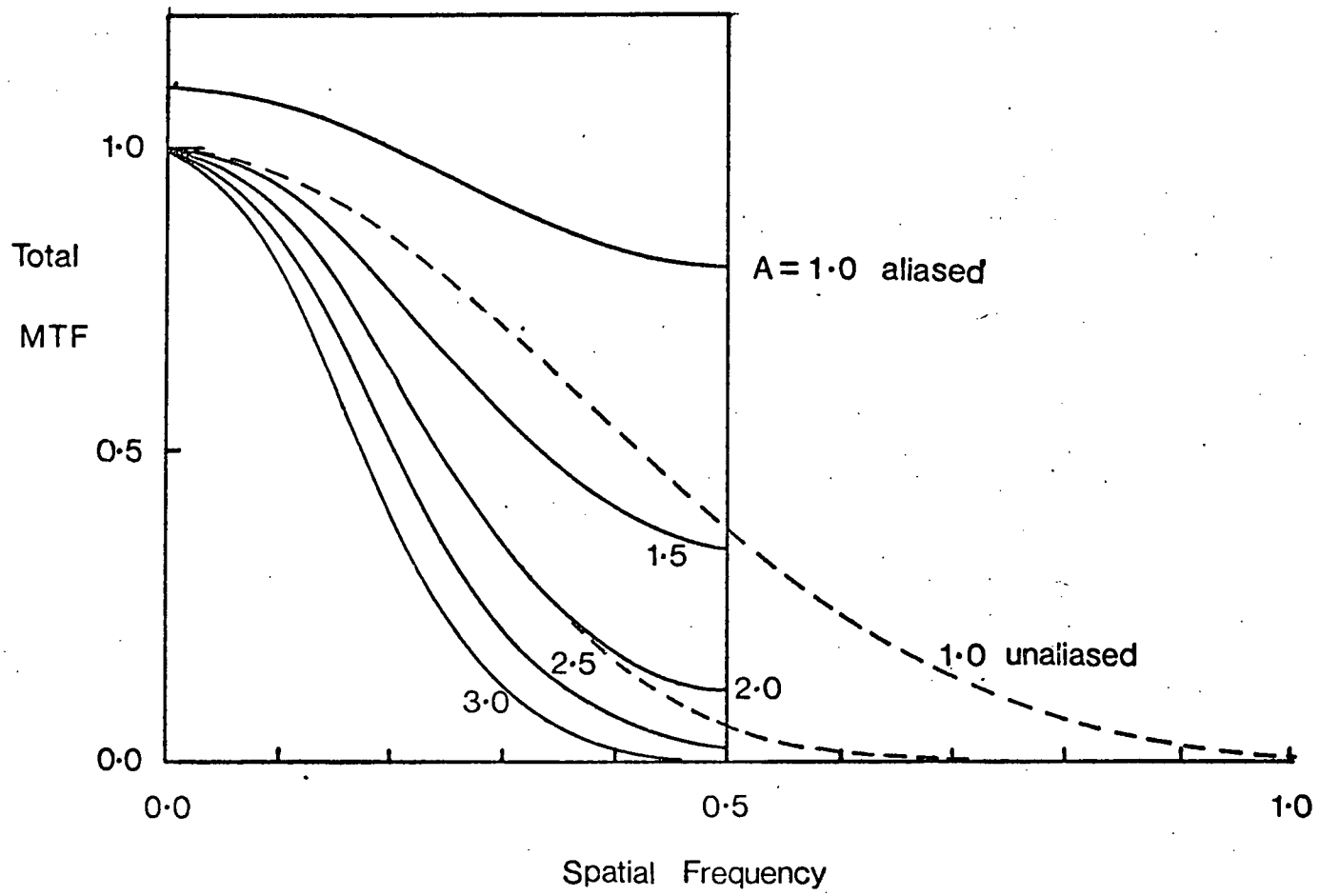

FIGURE 7. Effect of different seeing diameters on Gaussian response function (total MTF).

TABLE V . Aliased and unaliased Gaussian response functions (total MTF), with a=0.9, b=0.6, c=d=0., D=1.0. Upper numbers in each line pair are R(u,v) (unaliased). Lower numbers are F(u,v), including aliasing for k,m=-1,0,1. Total signal loss due to 54% live area ratio included.

Seeing	Spatial Frequency (u,v)			
A/D	(0.,0.)	(0.5,0.0)	(0.,0.5)	(0.5,0.5)
0.5	0.5400	0.3234	0.3973	0.2379
	0.9324	0.9551	0.9048	0.9268
1.0	0.5400	0.2036	0.2501	0.0943
	0.5971	0.4415	0.5098	0.3770
1.5	0.0942	0.1157	0.0202	
	0.5426	0.1891	0.2316	0.0807
2.0	0.5400	0.0320	0.0393	0.0023
	0.5400	0.0640	0.0786	0.0093
2.5	0.5400	0.0080	0.0098	0.0001
	0.5400	0.0160	0.0196	0.0006
3.0	0.5400	0.0015	0.0018	0.0000
	0.5400	0.0029	0.0036	0.0000
4.0	0.5400	0.0000	0.	0.
	0.5400	0.0000	0.	0.

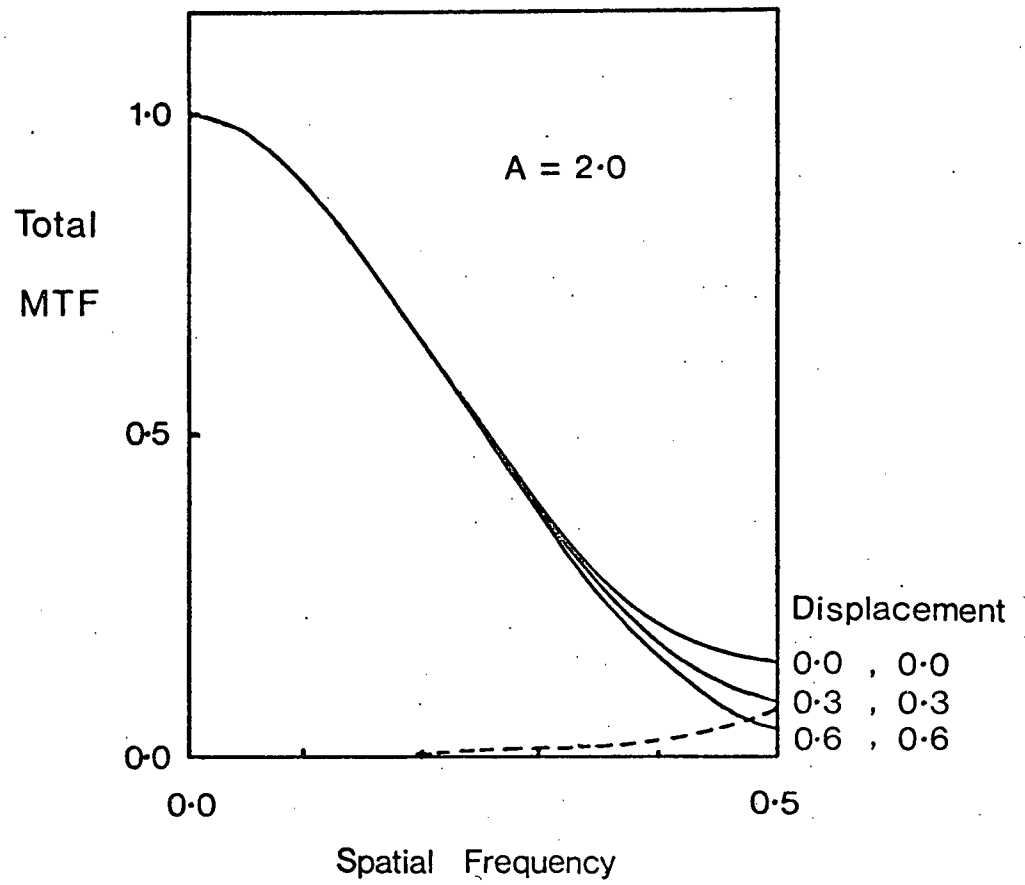

FIGURE 8. Effect of star image displacement on Gaussian response function (total MTF). Dashed line represents aliasing contribution to zero-displacement case.

centre of a diode. We see that for A=1.0 the GRF varies only at the high frequency end. For A/D $\geqslant$ 2.5, the effects are almost insignificant.

It is also very interesting that for A>2.0, the diode spacing rather than the dead area is the dominant parameter in determining the GRF. Figure 9 shows that at very low frequencies there is little difference between the Fourier transforms R(u,v) for live areas covering 1% and 100% respectively of the detector's surface. This result follows anaytically and was also tested using the simulated star image computed by invoking the instruction STAR in the FIRM code. Different displacements (c,d) of the star image gave similar results.

3.3 Techniques For Avoiding Aliasing.

As demonstrated in section 3.2, "photometry" of 1% or better accuracy is possible if the ratio of seeing disk diameter to diode centre-to-centre spacing is greater than or equal to 2.0 . Geometrical distortions at all frequencies below the Nyquist are essentially absent for A/D > 2.5. These criteria are almost independent of the ratio of "live" detector area to "dead" area. Thus, if one can match the diode spacing, the telescope plate scale and the local seeing properly so that the above criteria are met, there is no need to be concerned by aliasing. For example, the 1.8 metre

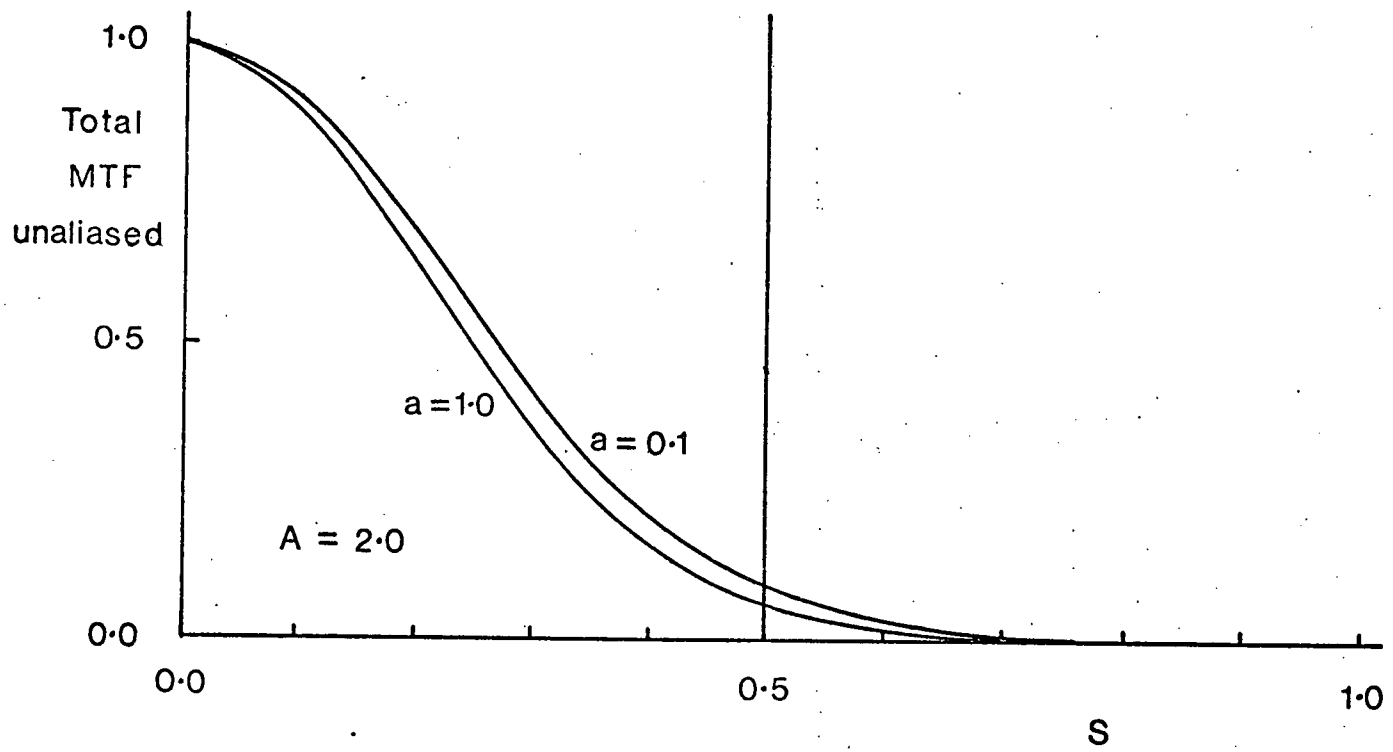

FIGURE 9. Effect of Dead Space on Gaussian response function (total MTF). Curves correspond to 100% and 1% fractional sensitive area, for a=1.0 and a=0.1 respectively.

reflector at the D.A.O., Victoria has a Cassegrain plate scale of 6 arc seconds per millimetre, corresponding to approximately 0.6 arc seconds per RETICON diode. The "limiting" seeing is therefore 1.2 arc seconds, a sharpness rarely achieved at this site.

If the seeing is better than the limiting seeing, problems will follow if one attempts to observe an object which intrinsically has high spatial frequency features. If A/D < 2.0 and star-like features are observed, meaningful area photometry can only be obtained by "pre-filtering" the image before it impinges upon the detector. In optics this is called <u>apodization</u> and can be achieved by suitable design of aspheric lenses, mirrors, or slits (Blackman and Tukey, 1959; p. 100). It is obvious that a Gaussian or similar apodizing function can simulate seeing and satisfy the aliasing criterion. However, this is likely to be an expensive method, so therefore other techniques should be examined.

An obvious candidate is de-focussiing of the image. A crude representation of de-focussing is the circular box-car function $\Pi_0(r)$, which has a simple Hankel transform:

$$\Pi_0\left(\frac{r}{2a}\right) \Longleftrightarrow \frac{a J_1(2\pi a q)}{q} \tag{27}$$

where $r = \sqrt{x^2+y^2}$ is the radial coordinate, a is the radius of the circular box-car function and $q = \sqrt{u^2+v^2}$ is the radial frequency. The function $J_1(x)$ is the Bessel function of order 1. The unaliased transfer function becomes:

$$R_{df}(u,v) = R(u,v) \cdot \frac{2J_1(\pi P q)}{\pi P q} , \qquad (28)$$

where P = 2a is the diameter of the defocussing function, and the volume of the function is unity .

Calculations of the total MTF (or GRF) involving circular defocussing showed that even for P/D = 5 the best possible photometric accuracy was no better than 1%. The conclusion is that defocussing is an inadequate prefiltering method especially if a central obscuration is present. However, it does sharply reduce aliasing if A/D << 1.0, and may in some cases be necessary. Some of the problems can be overcome using square apertures or baffles in the collimated beam. For example, a square aperture can be placed over the front of the telescope , with a square baffle over the rear of the secondary, such that the defocussed image will be a square with a square hole at the centre. To fully eliminate aliasing at zero frequency, the size of the defocussed image of a point source must be an integral multiple of the diode spacing, as must be the size of the square hole at its centre. This is not an efficient technique, as well as being somewhat unpractical for large telescopes. The desirability of a square convolving function suggests the following method.

A very promising technique is scanning the image across the detector in some carefully controlled manner. An example of this is the electron beam scanning method used by Beaver <u>et</u>

al. (1972). In the optical case, the image can be scanned in two dimensions using refracting plates as in the scheme illustrated in Figure 10. Such a system has not been constructed, but its principles need to be discussed.

The aim of scanning is to simulate a box-car convolving filter by having each point of the image spend an equal time on the sensitive fraction of the detector. This is accomplished by moving the image in a raster pattern as shown in Figure 10. Filters other than the box-car are possible but are much more difficult to realise.

The same effect can be produced by scanning the telescope itself in a raster pattern. Care must be taken that the scan is uniform and that the telescope does not dwell at the turning points. The inertia of a large telescoe makes such a uniform raster difficult to achieve. The size of the raster should be an exact multiple of the diode spacing D, so that the equal-time condition holds. This condition can be understood in the spatial frequency domain as the requirement that the zeroes of the convolving function be made to fall at all integral frequencies.

An attempt was made to perform computer-controlled 10 arc second square raster scans with the 2.2 metre telescope of the Mauna Kea Observatory, but equipment problems prevented the use of the method during observations. This technique is worth further tests with more reliable equipment. Alternative

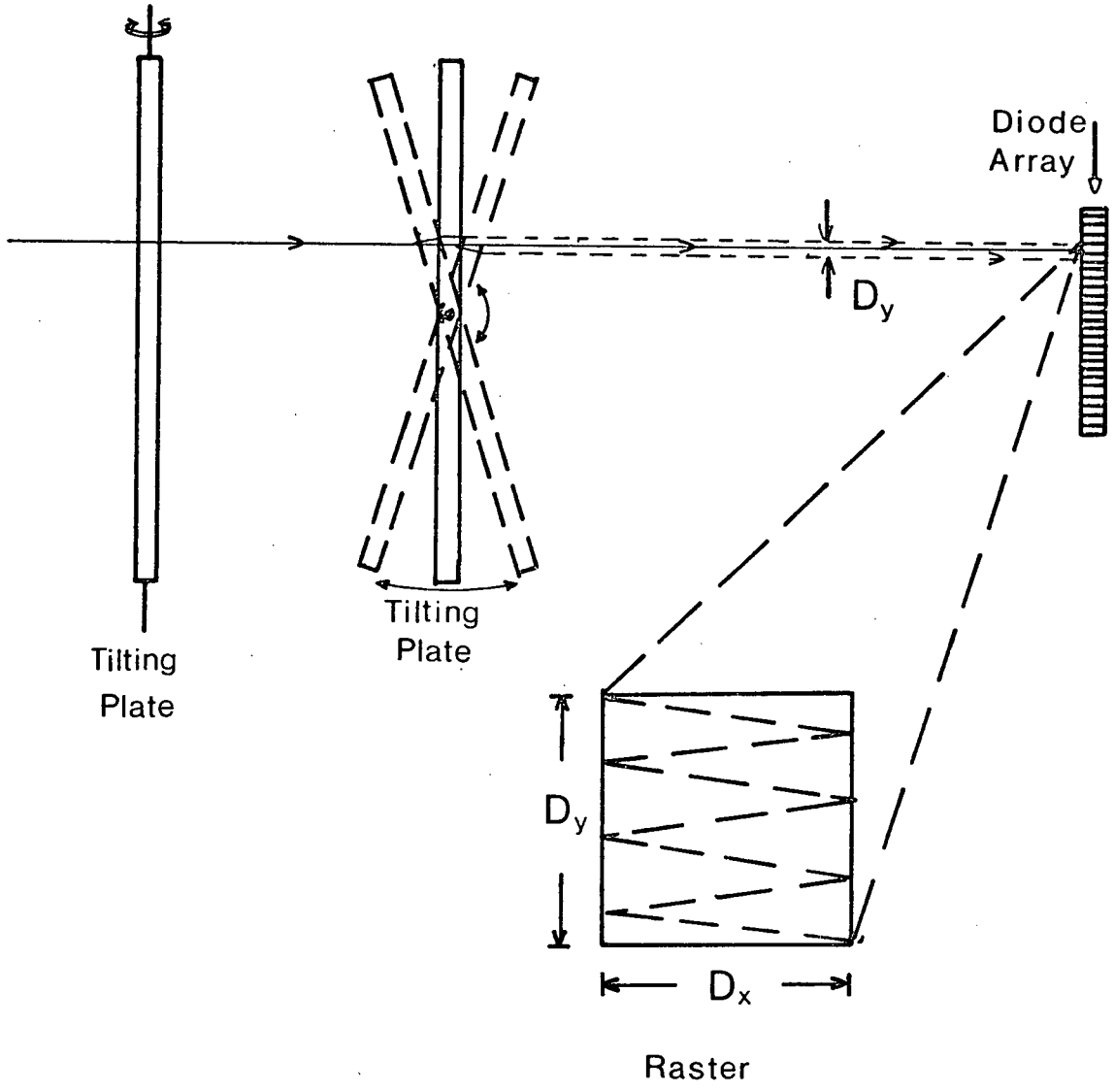

FIGURE 10. Raster Scanning to reduce aliasing. Proposed system would use two tilting refracting plates to make every point of image execute a raster over the detector.

techniques would involve moving the detector but not the telescope, or moving the secondary mirror. Both these techniques would introduce particular problems, and would require new and very precise hardware.

The scanning procedure can be mathematically represented by

$$f_{scan}(x,y) = f(x,y) * \left\{ \frac{1}{n^2 D^2} \Pi\left(\frac{x}{nD}\right) \Pi\left(\frac{y}{nD}\right) \right\} , \qquad (29)$$

where n is an integer. This transforms to,

$$F_{scan}(u,v) = \sum_k \sum_m R\left(u - \frac{k}{D}, v - \frac{m}{D}\right) \cdot$$

$$\cdot \operatorname{sinc}\left\{ nD\left(u - \frac{k}{D}\right)\right\} \operatorname{sinc}\left\{ nD\left(v - \frac{m}{D}\right)\right\} . \qquad (30)$$

The net effect of apodization by scanning is to make a rectangular "boxcar" diode function more triangular in the MTF or GRF, or "pyramidal", thus reducing the side lobes of its transform and therefore reducing the aliasing. At integral spatial frequencies zeroes are introduced, thus eliminating aliasing at zero frequency. Small-scale sensitivity irregularities, within each diode are also smoothed out, even if there is no dead space between diodes. The gain of reduced alassing must be balanced against the slight loss of resolution caused by pre-filtering or apodization.

In the future, aliasing may not be a serious problem.

Back-illuminated CCD's, for example, have little dead space between detector elements. Apodization techniques may nevertheless be desirable for reducing inherent aliasing by controlling the instrumental profile. (Inherent aliasing is defined as the aliasing at higher spatial frequencies due to the shape of the diode response function, even without "dead spaces"). One obvious application is the determination of star positions with high accuracy, as in astrometry. The results of Chapters 4 and 5 show that star positions could be determined to within 0.01D, unless limited by geometrical irregularities in the diode array.

3.4 Principles Of Data Reduction.

Signals are recorded on magnetic tape as outlined in Chapter 2 . A "frame" can be an object observation, a sky measurement, a dark current, a flat field or a short dark current measurement used as a "fixed pattern". The raw observations need to have the fixed pattern, dark and sky contributions subracted. The remainder is then divided by the similarly reduced observation of a flat field. These are standard procedures of area photometry and have been described by Crane (1975). In mathematical form, for the ij-th diode,

$$r'_{ij} = \frac{r_{ij} - s_{ij} - d_{ij} - p_{ij}}{f_{ij}} \qquad (31)$$

where r_{ij} is the raw measurement, s_{ij} is the sky contribution, d_{ij} is the dark current contribution for the same integration

interval, p_{ij} is the fixed pattern and f_{ij} is the "flat field" intensity. The quantities s_{ij}, d_{ij}, and f_{ij} do not contain a fixed-pattern contribution. For short exposure times, it is possible to combine the dark, sky and fixed pattern into a single integration q_{ij} such that,

$$r'_{ij} = \frac{r_{ij} - q_{ij}}{f_{ij}} \tag{32}$$

When the exposure time for the measurement r is long, it is inefficient to take as long to measure the sky background, since an average over all the diodes can be computed:

$$\langle s \rangle = \frac{1}{N} \sum \left(\frac{s_{ij}}{f_{ij}} \right) , \tag{33}$$

whence

$$r'_{ij} = \frac{r_{ij} - d_{ij} - p_{ij}}{f_{ij}} - \langle s \rangle . \tag{34}$$

This cannot be applied to the subtraction of the dark current, which varies non-uniformly from diode to diode. The "field-flattening" values f_{ij} are suitably normalised,

$$f_{ij} = \frac{f'_{ij}}{\langle f' \rangle} , \tag{35}$$

where f are the intensities derived by observing a flat field such as the dusk or dawn sky, with the corresponding fixed pattern and dark contribution subtracted.

The frame reduced via equations 31, 32 or 34 contains the

intensity distribution of an image with some noise added.

The noise performance of the RETICON area photometer has been described in Chapter 2, and shows an approximately Gaussian distribution of deviations from the mean under normal conditions. Standard signal processing techniques in two dimensions can be applied to reduce the noise. While optimal Wiener filtering is desirable (e.g. Arp and Lorre 1976), a simple circular Gaussian filter is used in this work. In some cases no filtering is needed because the signal to noise ratio is sufficient. The filtering procedure involves transforming the picture using a Fast Fourier Transform (FFT) routine, multiplying the transform by the transform of the filter and performing the inverse transform. A simple conical convolution filter applied in the real domain gives similar results in an equal or longer computation time. The FFT technique is preferable because the image can also be moved simultaneously using the shift theorem (Bracewell, 1959, p.244). Colour index or ratio maps are computed by registering two images and dividing.

Model intensity distributions can be computed and subtracted to map the residuals. Simple operations and manipulations of picture data can be combined for sophisticated analysis of the data, for which a general and powerful computer code is needed.

3.5 FIRM : An Image Processing Code.

A number of astronomical picture-processing codes have been developed, such as the MIT code "IIPS" (McCord et al. , 1975), the Cal Tech-JPL code "VICAR" (see Arp and Lorre, 1976), the Kitt Peak system (Wells 1975),and others (see: Klinglesmith 1975; Nieuwenhuijzen 1975). All such codes depend on the hardware and software available at the institutions where they were developed, so it was decided to develop a sequential modular processing language for the facilities at the University of British Columbia . This code is called FIRM (for Fortran Interactive Record Manipulation), and is set up for the IBM 370/168 running under the Michigan Terminal System (MTS) with virtual memory. It can be used either in batch or interactive mode, but the economics and turnaround speed at U.B.C. make the batch mode more attractive. Table VI lists the operations performed by FIRM. A full description of the code and its usage is given in Appendix I.

The most important operations in the final processing of reduced data are PLOT, FT, SECTION, ELLIPSE and STAR. The other operations such as ADD, DIV, etc. are elementary.

The PLOT command causes a contour map to be generated using a modified version of UBC CNTOUR. The area and centroid of every closed contour are computed, and printed if the effective radius is above some pre-defined lower limit (usually 0.5 diode spacing units). The effective radius r of

TABLE VI . Operations performed using FIRM , a FORTRAN Interactive Record Manipulation Language.

Operation		Function
APERTURE		Integrate over a square aperture in the field of view.
ADD		Add two images.
AI		Add constant to each element of an image.
AVERAGE		Read from tape and average two or more raw images.
COLUMN		Specify which columns "dead" or "live".
DIVIDE		Divide an image by another.
ELLIPSE		Generate a model ellipsoidal distribution or generate a circular aperture.
END		End processing and exit to MTS.
EXAMINE	AVERAGE	Print averages and extreme values,
	LABELS	print labels,
	HIST	plot a histogram, or
	CATLG	print the output file catalogue.
FT		Smoothing and/or shifting via the FFT.
GRAPH		Graph the value at each element of one picture versus the value of each corresponding element of a second picture.
INT		Convert magnitudes to intensity.
LABEL		Label a picture already in core memory.
LOAD		Read a raw data record from magnetic tape and load into core.
MAG		Convert intensity into magnitudes.
MI		Multiply each element of picture by constant.

MOVE	Move an image into a different array in core. Six arrays are available. Optionally, registration of images is performed using bi-linear interpolation.
MULT	Multiply two images.
PLOT	Plot a CALCOMP or printer contour map of an image. Print closed contour centroids and areas.
PRINT	Print the contents of an image array using the line printer.
RETRIEVE	Read back a reduced image from the output tape.
ROW	Define dead or live rows.
SECTION	Plot a graph of the cross-section of an image along a straight line or along an elliptical locus.
SHIFT	(Synonym for MOVE)
SMOOTH	Convolve a picture with a conical filtering profile.
STAR	Compute a Gaussian "star image" intensity distribution.
SUB	Subtract an image from another image.
VIEW	Print a 10x10 matrix of numbers corresponding to a 50x50 image averaged in 5x5 blocks.
WRITE	Write an image as a record on the output tape. Enter label into catalogue.
YY	An operation to be defined by the user.

each contour is defined as,

$$r^* = \sqrt{\frac{A}{\pi}} \tag{36}$$

as done by de Vaucouleurs and Freeman (1972), where A is the area of the contour. The centroids of the contours of sharp features in an image are used to find the movement necessary to register the image with another image so that ratio or difference maps can be computed. This detailed technique is used here rather than the global cross-correlation technique more commonly used by other workers (e.g Fischel 1976).

The bi-linear interpolation optionally used for image registration with the MOVE or SHIFT instructions is probably inferior to the Fourier shift theorem used when FT is invoked, unless very sharp spikes are present in the data. The Fourier method involves multiplying every element of the discrete Fourier transform (DFT) by a phase factor,

$$\exp\left\{-2\pi i\left(u_m \Delta x + v_n \Delta y\right)\right\}, \tag{37}$$

where $(\Delta x, \Delta y)$ is the desired image movement in the (x,y) plane and (u_m, v_n) are the spatial frequencies (m/N, n/N) of the elements of the discrete Fourier transform.

Filtering is equivalent to convolving with a Gaussian of effective diameter A in real space specified by the user in the FT instruction. This involves multiplying each element of the DFT by

$$\exp\left\{-\frac{\pi^2 A^2}{4}\left(u_m^2 + v_n^2\right)\right\} \quad . \tag{38}$$

The alternative smoothing instruction is SMOOTH, which uses a two-dimensional convolving filter corresponding to a cone with fixed base diameter 4.0 in the real domain,

$$0.2397 \begin{bmatrix} 0.2929 & 0.5 & 0.2929 \\ 0.5 & 1.0 & 0.5 \\ 0.2929 & 0.5 & 0.2929 \end{bmatrix} \tag{39}$$

This can be compared with the square convolving function used by Davis (1975).

In both FT and SMOOTH it is assumed that the outer boundaries of the image are the outermost "live" rows or columns and that the intensity distribution beyond a boundary is a <u>reflection</u> of the distribution inside the boundary. When smoothing is used, some bias occurs near the edges, but at least no information external to the observations is introduced.

The command SECTION uses simple bi-linear interpolation to plot the intensities along a straight line or elliptical locus in the image plane, while the instructions ELLIPSE and STAR produce various model distributions which can be compared with or subtracted from reduced images. An elliptical

distribution can be computed with a simple King, "generalized" Hubble, de Vaucouleurs or exponential radial dependence. A circular uniform distribution can also be computed for use as a multiplicative "integrated photometry " aperture. Stellar images are assumed to be Gaussian, although a more precise extended profile such as that measured by Kormendy (1973) will be needed for work with detectors more sensitive than the RETICON RA50x50 .

Stellar or extended intensity distributions are integrated using the instructions APERTURE or EXAMINE AVERAGE . The command APERTURE uses a square aperture of specified size, with the centre being automatically placed at the centroid of the observed image. The aperture produced by ELLIPSE must be located by the user, multiplied by the observed image and integrated via the EXAMINE AVERAGE instruction.

CHAPTER 4

THE SPIRAL GALAXY NGC 4736(=M94)

4.1 Background.

The galaxy NGC 4736 is classified as Sb in the Hubble scheme (Humason, Mayall and Sandage, 1956), and (R)SA(r)ab in the de Vaucouleurs scheme (de Vaucouleurs 1963). Other classifications are listed by de Vaucouleurs and de Vaucouleurs (1964). The principal data for this galaxy are listed in Table VII .

Photographs of this galaxy reveal a structure which is regular but very complex. The descriptions given by Sandage (1961), Chincarini and Walker (1967), Lynds (1974), van der Kruit (1974,1976) and Bosma, van der Hulst and Sullivan (1977) indicate the following optical structure:

(a) A prominent nucleus of 3 to 4 arc seconds diameter,

(b) A very bright central region of about 16 arc seconds radius , with spiral structure extending from about 7 arc seconds to one minute of arc. This inner spiral structure is defined by dust lanes.

(c) At a radius of 30 to 60 arc seconds, a ring of bright H11 regions embedded within fainter diffuse emissions.

(d) Between 60 and 180 arc seconds radius, the main disk of the galaxy, filled with a tight and broken spiral structure.

TABLE VII . Elements and properties of NGC 4736

α(1950)	12h 48.6m	(1)
δ(1950)	41° 23'	(1)
Galactic longitude	123.3°	(1)
Galactic latitude	76.0°	(1)
Hubble type	Sb	(1)
De Vaucouleurs type	(R)SA(r)ab	(1)
DDO type	Sb-pec.II:	(1)
Morgan type	D-S g	(1)
Photographic magnitude m_{pg}	8.91	(2)
Colour B-V	0.76	(2)
Face-on diameter D(0)	6.76'	(1)
System velocity V(sys)	314±1 km s^{-1}	(3)
Distance	6±2 Mpc	(4)
Inclination	35±10°	(4)
Position angle of line of nodes	122±3°	(4)

Source References

1. de Vaucouleurs and de Vaucouleurs (1964).
2. de Vaucouleurs, Corwin and Bollinger (1977).
3. van der Kruit (1976).
4. Schommer and Sullivan (1976).

(e) A zone of very low surface brightness between 200 and 260 arc seconds radius.

(f) A faint external ring, starting at 260 arc seconds from the centre.

Recent work shows that this galaxy is a most interesting "laboratory" for galaxy dynamics. There exists a triple radio source centred at the nucleus, with the two outer lobes coinciding with the emission ring (van der Kruit 1971). These sources have a non-thermal spectrum (de Bruyn 1977). Photometry by Simkin (1967) shows distinctly bluer colours in the emission ring, indicating a young stellar population there. Pritchet (1975, 1977) obtained polarization Fourier spectrometer scans using a 20 arc second aperture over the nuclear region, and he also found there a significant young star contribution after applying population synthesis techniques.

A good optical rotation curve has been obtained by Chincarini and Walker (1967), who found that both the absorption and emission lines were sharp and that there was no difference between the velocities of the absorption and the emission lines, unlike the centre of M31 (Pellet 1976). Van der Kruit (1974, 1976) has obtained numerous spectrograms at different position angles and has measured the extent and the radial velocities of the emission lines associated with the inner ring. The outer structure of this galaxy and its HI rotation curve strongly suggest that the inner emission ring should be

near the inner Lindblad resonance, while the gap between the main disk and the outer ring probably corresponds to the corotation radius (Schommer and Sullivan 1976). Van der Kruit's results for the inner ring, however, are not completely consistent with conventional models of a dispersion ring at the inner Lindblad resonance (van der Kruit 1974,1976). It is most likely, from van der Kruit's exhaustive studies, that an excessive outward expansion exists in the inner ring, the excess being most pronounced at the east and west extremities of the ring. The extent of the ring is also quite interesting, with an apparent inner boundary at about 30 arc seconds radius and a sharp outer boundary at about 60 arc seconds radius. The Hα emission appears to be diffuse, with HII regions embedded in it. It should be noted that Chincarini and Walker (1967) found emission lines right into the nucleus, a possibility not discounted by van der Kruit (1976).

One possible model for the discrepant velocities in the emission ring is that the ring is the result of an explosion in the nucleus (van der Kruit 1974). A theoretical model has been computed by Sanders and Bania (1976), and it appears to be quite successful in explaining the ongoing star formation, the non-circular motions, and the non-thermal radio emission. The most important observational test for the Sanders-Bania model is a pair of dips in the rotation curve, but such dips are not confirmed by the most recent observations of van der

Kruit (1976).

An even more curious phenomenon perhaps is the existence of spiral structure within the inner emission ring. This structure appears to be defined by dust lanes, and conventional photographs reveal spiral structure extending to within 7 arc seconds of the centre (Chincarini and Walker 1967). Since in addition this galaxy has an unusually high surface brightness in the bulge region (Simkin 1967; Pritchet, personal communication), it was chosen for observation at Mauna Kea Observatory in March and April, 1976, using the RETICON area photometer.

4.2 NGC 4736: The Observations.

The RETICON area photometer was mounted at the Cassegrain focus of the 2.2 metre telescope of the Mauna Kea Observatory. Three exposures, each of 5 minutes, were taken , one each through blue, visual and red filters. A corresponding three exposures were taken of the sky background and a further three exposures of five minutes each were taken through a polarizing element devised by R. Wolstencroft. A visual double star, HR4708, was used to calibrate the plate scale on the detector and the orientation of the instrument. An exposure of the evening sky was used as the flat field calibration. The relevant observations, together with their record numbers on my permanent file tapes, are listed in Table VIII . The data

TABLE VIII . Log of observations for NGC 4736.

Permanent Rec. No.	Object	Filter	Exp. Time	Time at end (U.T.)
File 13				1976 March 30
6	Dusk Sky	None	5m	5h 13m
7	Dark	-	"	5h 24m
35	Sky	B	"	11h 38m
36	NGC4736	B	"	11h 48m
37	"	V	"	11h 52m
38	Sky	V	"	12h 00m
39	"	R	"	12h 05m
40	NGC4736	R	"	12h 16m
41	"	Pol 1	"	12h 37m
42	"	Pol 2	"	12h 44m
43	"	Pol 3	"	12h 52m
44	Sky	Pol 3	"	12h 58m
45	Sky	Pol 1	"	13h 06m
46	"	Pol 2	"	13h 12m
62	Faint Star	B	1m	14h 12m
63	" "	V	"	14h 13m
64	" "	R	"	14h 15m
65	" "	-	"	
File 38				March 31
162-166	HR4708A+B	B	10s	12h 25m
167-172	"	V	"	12h 27m
173-178	"	R	"	12h 28m
179-181	Dark	-	"	12h 29m

are encoded on duplicate labelled library tapes stored in the permanent magnetic tape rack of the Computer Centre at U.B.C. The file and record numbers given in Table VIII will allow the listed data to be located on these tapes as required. Appendix II lists the contents of the library tapes.

Owing to difficulties with the equipment, only a single unsaturated filter-less exposure, of the sky at dusk, is available as a flat-field calibration image.

The orientation and angular scale of the detector and telescope combination was simply calibrated by using a suitable well-observed visual double star. I assume that both the scale and orientation are constant over the detector meaning that the plate transformation is assumed to be linear, and that the diodes are regularly spaced and aligned as specified by the RETICON Corporation.

The double system HR4708 was used to calibrate the scale and orientation of the observations of NGC 4736. Landolt (1969) has published photometry for this system. Due to an excessively pessimistic estimate of the response of the system before the first observing run on the 2.2 metre telescope, HR 4708A saturated the diodes near the centre of its seeing disk even with the shortest possible exposure time, thus precluding its use for magnitude or colour calibration. Varying degrees of saturation between the blue, visual and red exposures do not lead to significantly different scales or orientations of

the images.

Since a series of exposures on stars in Praesepe were similarly saturated, it has not been possible to tie the instrumental measurements into the standard Johnson UBVRI system. Observations with the RETICON area photometer at Victoria and Vancouver reported in Chapter 5, however, indicate that the following differentials probably apply:

$$\left.\begin{aligned} \delta V &\simeq 1.0 \quad \delta v \\ \delta(B-V) &\simeq 1.1 \quad \delta(b-v) \\ \delta(V-R) &\simeq 1.2 \quad \delta(v-r) \end{aligned}\right\} , \qquad (40)$$

where b, v, and r are the magnitudes in the instrumental blue, visual and red passbands.

The positions of HR 4708 A and B in each exposure have been determined by averaging the centroids of contours for each star image. Only contours with radii between 1.0 and 2.0 diode units were used for the averaging. The scales for each of the three filters did not differ by more than 0.6% from each other, and did not lead to serious registration errors over the area of the detector when images were registered using a star-like feature near the centre of the detector. The average spacing between HR 4708 A and B was 22.49±0.05 (std. devn.) diode units, with position angle of 67.9±0.1 degrees in the instrumental system. The weighted average of the

measurements listed by Aitken (1932) for ADS 8531 gives a separation of 20".04±0.36 (std. devn.), at a position angle of 336.7±0.1 degrees in the celestial coordinate system. This puts North in the direction of increasing X, East in the direction of Y. Figure 11 shows the relationship between the instrumental orientation and the celestial coordinate system. The "plate" scale is 0".89±0.02 (std. devn.) per diode (diodes are spaced at 4 mils or 101.6 microns).

The absolute intensity calibration in the v passband is obtained by comparison with the aperture photometry of Chincarini and Walker (1967). Using the plate scale of 0.89 arc sec./diode, synthetic circular apertures were computed corresponding to the three smallest centred apertures used by Chincarini and Walker. A numerical integration of the signal within each aperture was performed, and the totals converted to magnitude measure. Table IX summarises the data necessary to calibrate the reduced form of record F13R37 from instrumental v magnitudes to Johnson V magnitudes.

The consistency of the differences v-V in Table IX is very encouraging, considering the errors which can be introduced by uncertainity in the plate scale and by assuming V= v. Table XIII for the visual filter data contains a column giving isophotal surface brightnesses in V magnitudes per square arc second.

The seeing has been estimated from observations of a

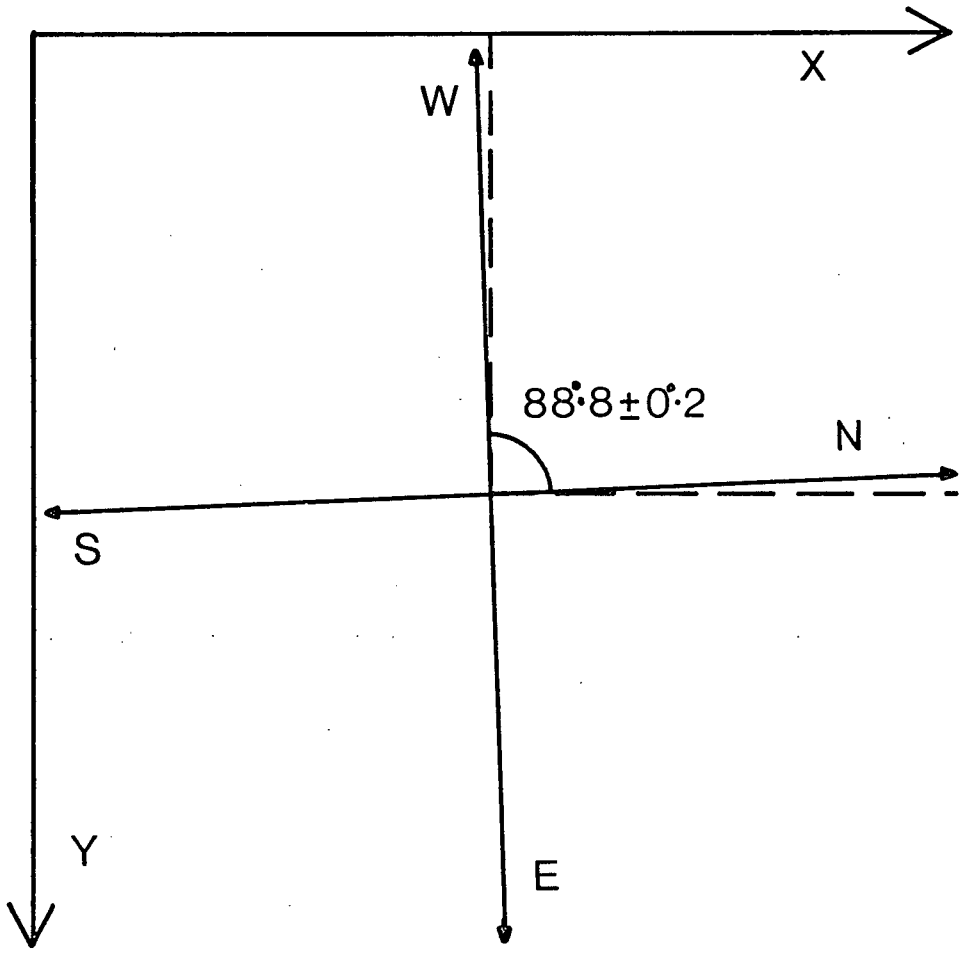

FIGURE 11. Relationship of orientations between camera and sky. Coordinates X, Y are aligned with diode array.

TABLE IX . Comparison of integrated circular aperture visual magnitudes in the instrumental system with photometry by Chincarini and Walker (1967) =C+W. The calibration applies to exposure F13R37 of NGC 4736. Corrected for sky background and flat field.

Aperture Diameter	C+W V	This Work v	Difference v-V
11"	10.85	-10.60	-21.45
17"	10.28	-11.18	-21.46
28"	9.70	-11.72	-21.42

Average Difference <v-V> = -21.44±0.02(s.d.)

<u>Add</u> 21.44 to convert from instrumental magnitudes to V magnitudes.

<u>Subtract</u> further 0.25 magnitudes to convert from V magnitudes per diode to V magnitudes per square arc second(").

faint star on the same night, although at a higher airmass and with a shorter exposure (1 minute) than for NGC 4736. Figure 12 shows the natural log of the contour intensities versus the square of the corresponding effective radii. The residual "semi-stellar nucleus" is also plotted (to be discussed later). Effective seeing diameters (to 1/e of central intensity) arc 3".7 (blue) 2".9 (visual), 3".2 (red), and 3".6 (polaroid). Longer exposures can be expected to give worse seeing figures. The effective seeing diameters include the effect of imperfect focussing and telescope guiding errors. Both the focussing and guiding controls were troublesome during this observing run on the 2.2 metre telescope.

The noise in the observations was evaluated by subtracting the visual sky exposure from the red exposure. The histogram of the difference is plotted in Figure 13. After subtraction of the mean, the difference pattern was squared and averaged to find the r.m.s. deviation, which was 1.75 instrumental units. This corresponds to the r.m.s. diode-to-diode noise within each exposure after subtraction of the sky (including the fixed pattern and dark current). A histogram of the flat field calibrating image minus a strongly smoothed version of the same flat field exposure yielded a wider and different distribution, with r.m.s. deviation of 2.75 instrumental units. I conclude that the flat field calibrating pattern has significant diode-to-diode variations greater than the random noise of

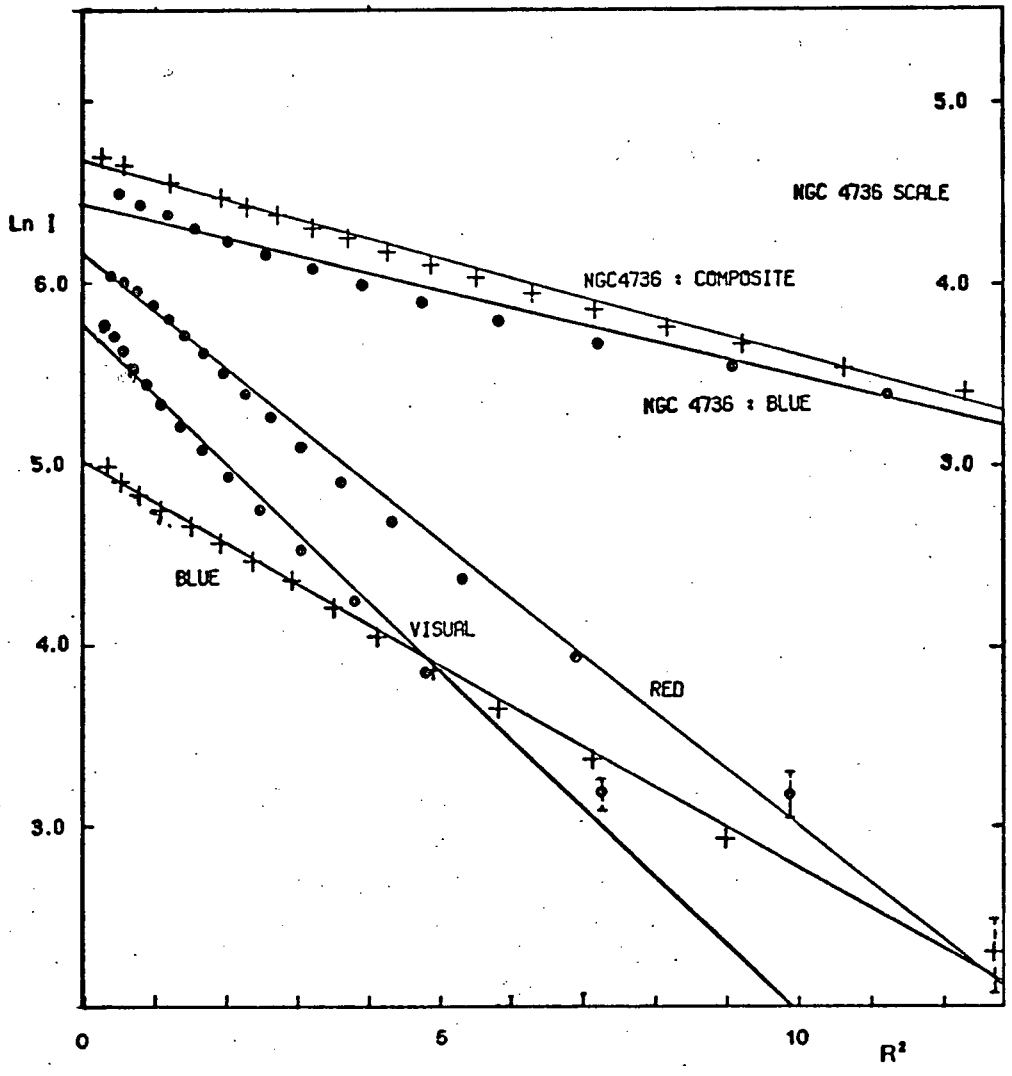

FIGURE 12. Star images in B, V and R filters plotted on Gaussian scale. "Residual nucleus" of NGC 4736 included for comparison.

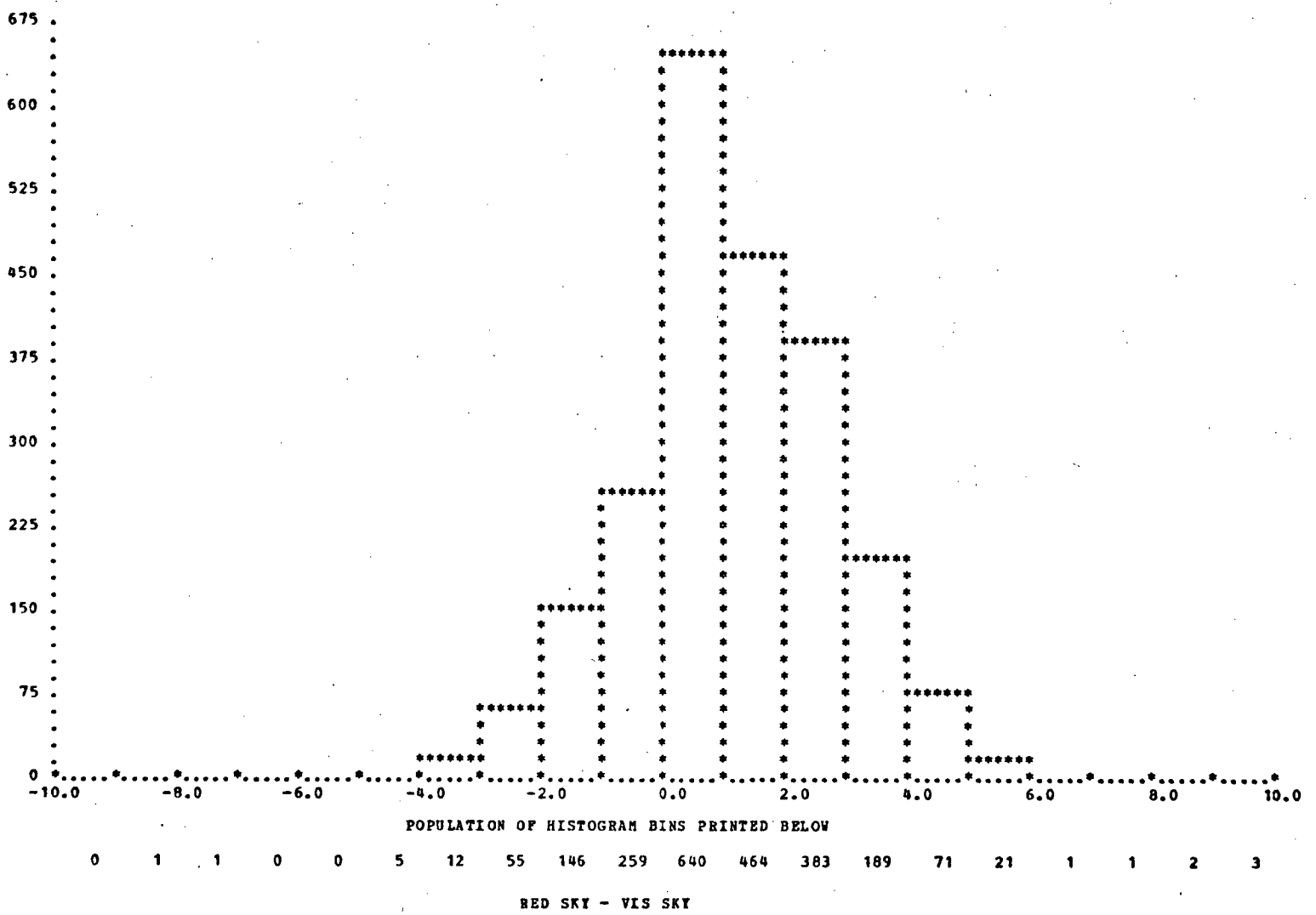

FIGURE 13. Typical Noise Histogram. Plot of differences between elements. Mean has been subtracted.

the observations. It is, therefore, invalid to smooth the flat field image before dividing the observed images by the flat field calibrating image.

Noise measurements using the same method for different times of the night of 1976 March 29/30 all had an r.m.s. deviation about the mean of the difference between two dark exposures of between 1.75 and 2.0 instrumental units. However the mean of the difference between two successive dark exposures of the same duration showed a fluctuation of up to ±3 instrumental units. Thus there was a general baseline drift from exposure to exposure, in addition to the diode-to-diode scatter within each exposure. Image regions of lower signal have correspondingly lower signal to noise ratio, limited by the diode-to -diode scatter and the baseline drift.

The brightest regions will be limited to the signal to noise ratio of the flat field calibrating image. Neglecting the baseline drift in this case, the signal to r.m.s. noise ratio of the single flat field calibrating image was 60 (using 1.8 instrumental units as the r.m.s. diode-to-diode scatter). This is the highest signal to noise ratio possible for a single picture element of the observations of NGC 4736.

The surface brightness maps reduced for sky, dark current and flat field correction in the instrumental filter system are presented as isophotal contours in Figures 14, 15 and 16. Figure 17 is a composite formed by registering the blue and

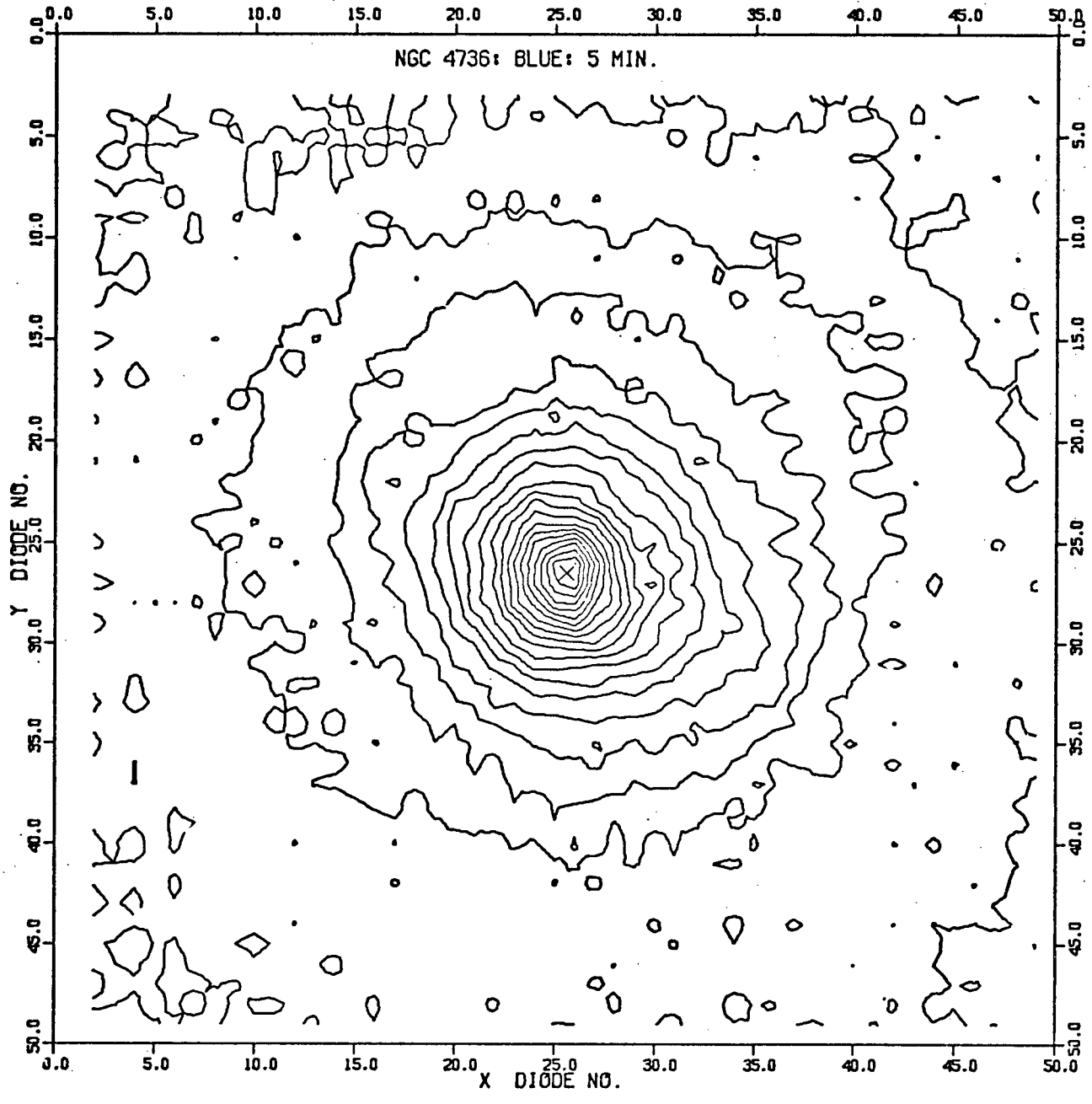

FIGURE 14. NGC 4736: Blue isophotal contours. Peak marked by 'X'. Closed contours listed in Table X. North is to the right (X), East is down (Y). (See Fig. 11).

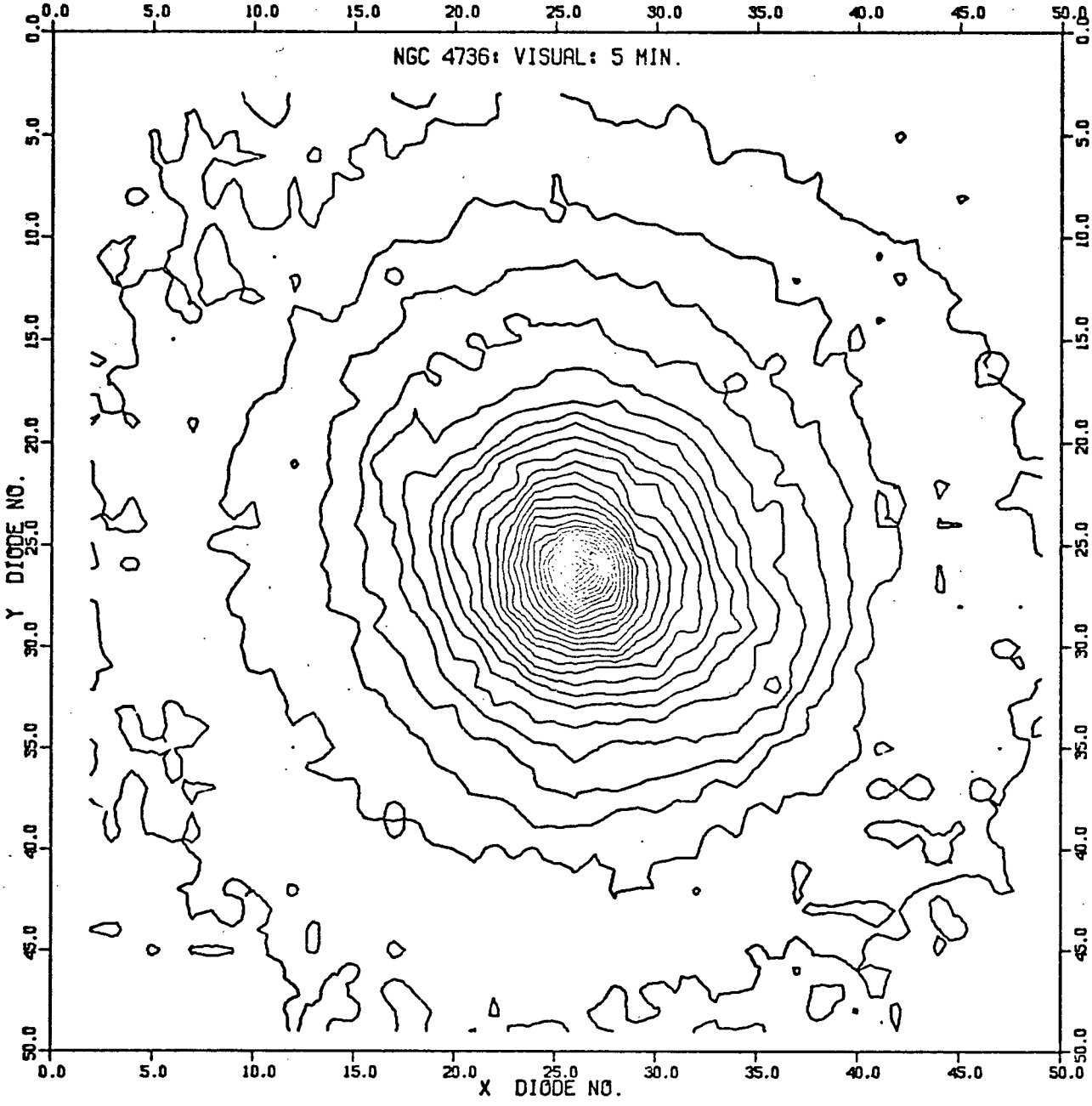

FIGURE 15. NGC 4736: Visual isophotal contours. Closed contours listed in Table XI. North is to the right (X), East is down (Y). (See Fig. 11).

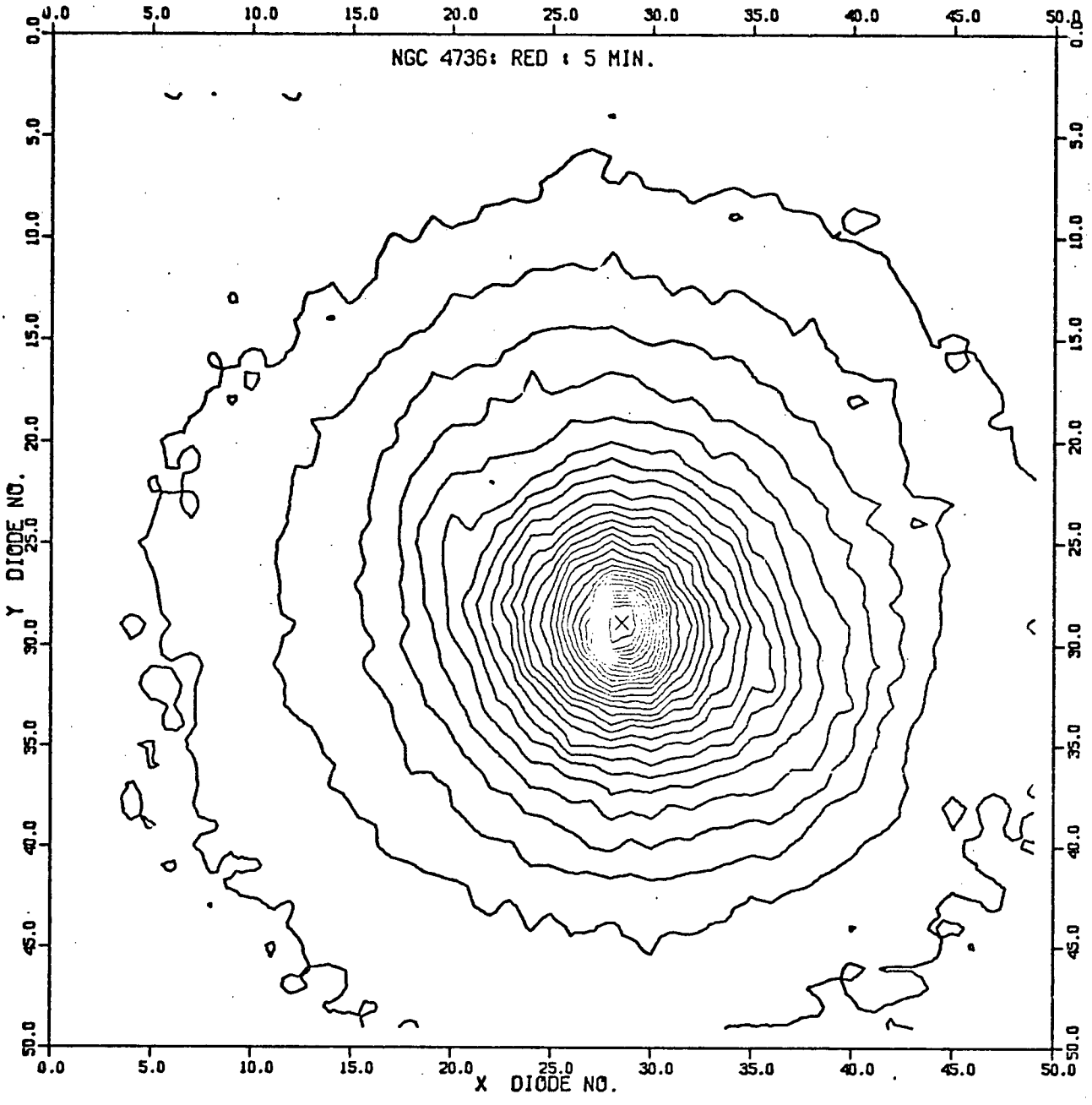

FIGURE 16. NGC 4736: Red isophotal contours. Closed contours centred on nucleus listed in Table XII. North is to the right (X), East is down (Y). (See Fig. 11).

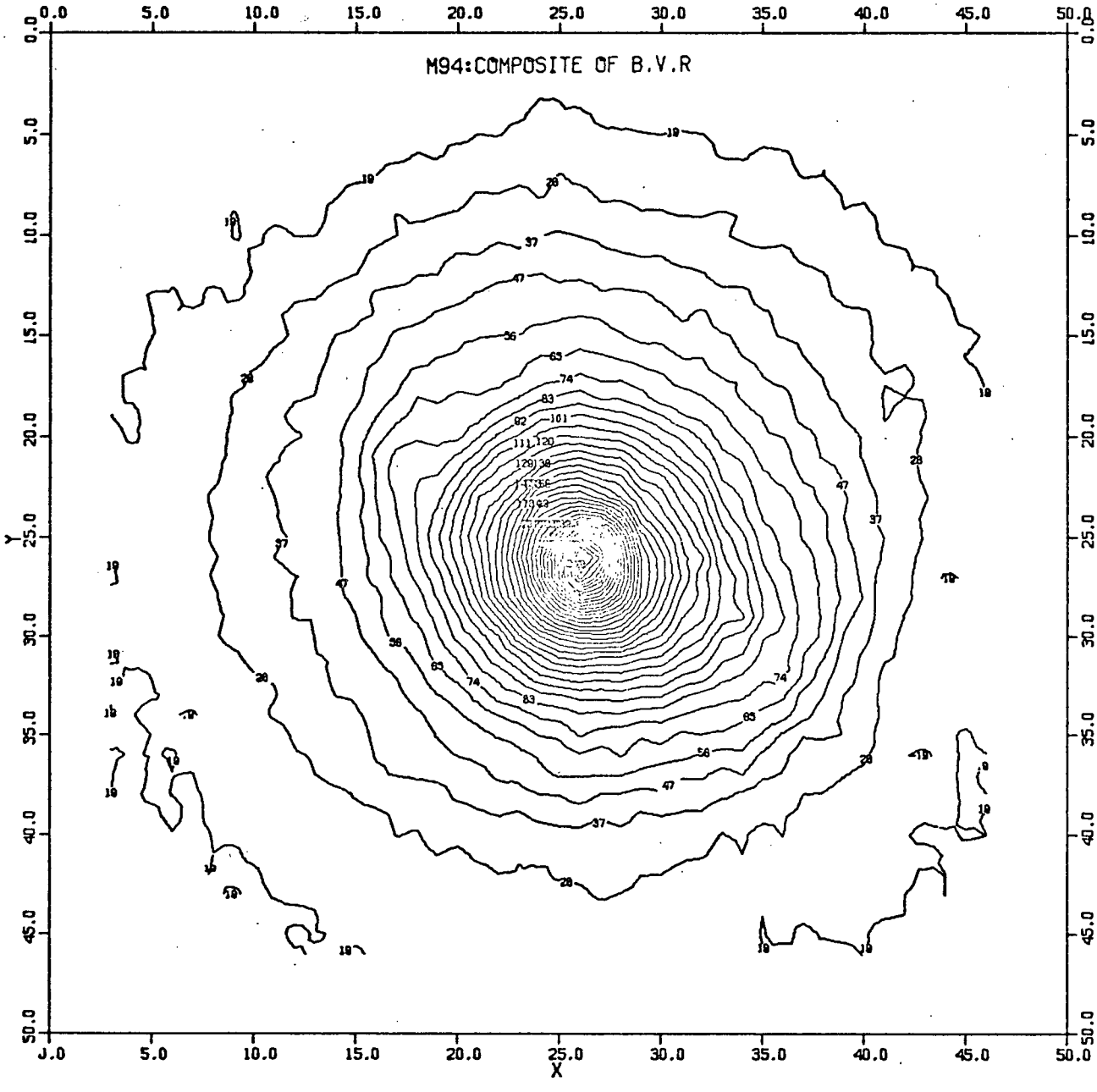

FIGURE 17. NGC 4736: Composite of B, V, R, isophotal contours. North is to the right (X), East is down (Y). (See Fig. 11).

red images to the position of the visual image, and performing a direct summation. Figure 18 shows the outer contours of the composite image smoothed to show the shapes of the contours.

4.3 NGC 4736: Analysis of Observations.

The first information needed to probe the inner structure of NGC 4736 is a "law" to represent the radial variation of surface brightness. A model-independent approach is one used by de Vaucouleurs and Freeman (1972) and by Ables and Ables (1972), whereby the area A of each contour is computed and a corresponding equivalent radius r derived, so that:

$$r_I^* = \sqrt{\frac{A_I}{\pi}} \qquad (41)$$

The plot of intensity I versus radius r_I^* then gives an intensity "law" independent of ellipticity and other distortions, but not independent of internal absorption. Figure 19 shows the variation of $\log_{10} I$ versus r_I^*, in the instrumental system red filter. Tables X, XI, and XII give values of I and r_I^* in each filter. The contours are the same as in Figures 14, 15 and 16. Table XIII gives V surface brightnesses calibrated using the calibration in Table IX.

Further insight may be gained by plotting I versus r using specialized scales. For example, Kormendy (1976) has used de Vaucouleurs' model very effectively by plotting log I versus $r^{0.25}$. The plot should be linear if de Vaucouleurs'

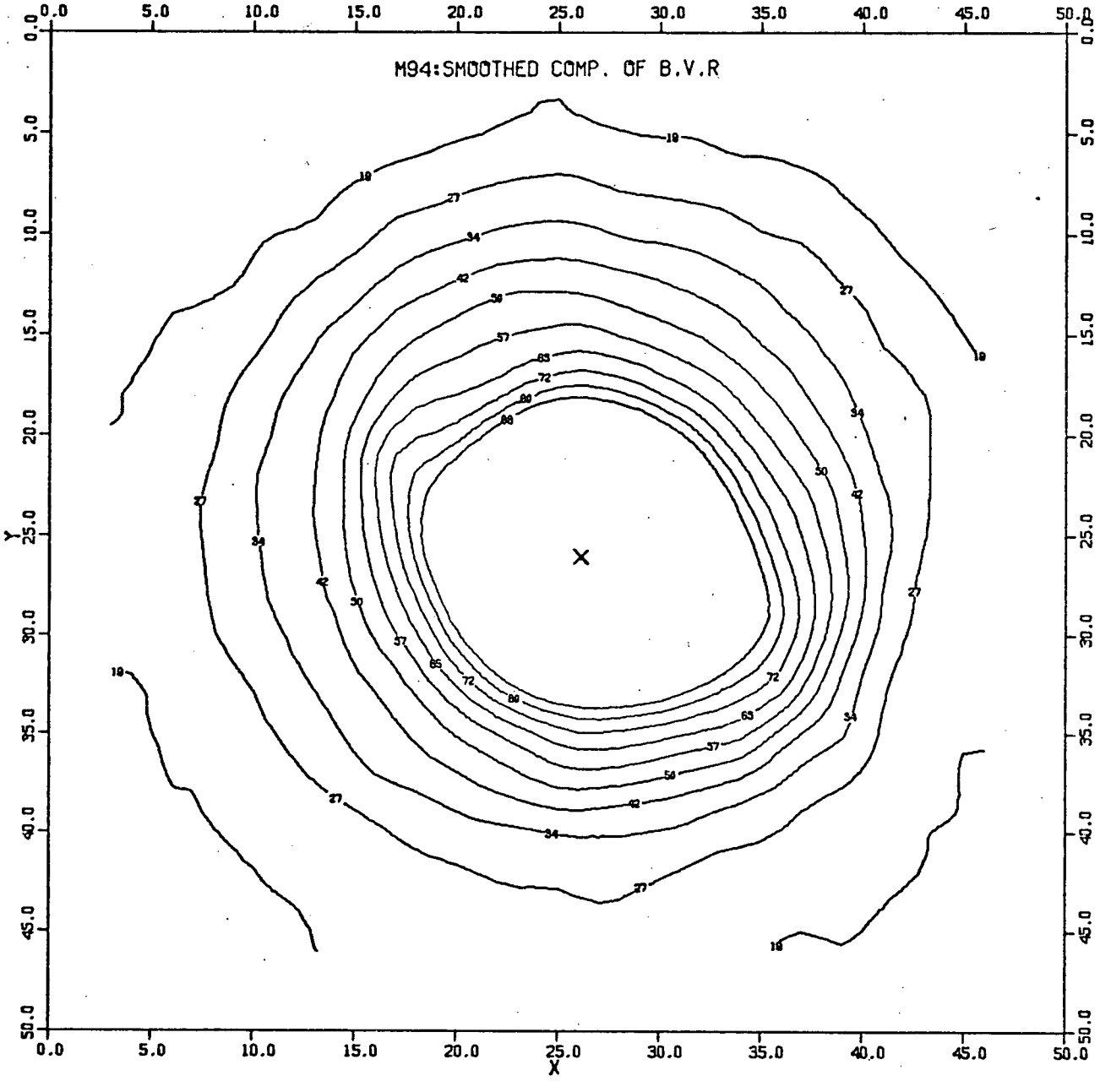

FIGURE 18. Outer contours of smoothed composite of B, V, R. North is to the right (X), East is down (Y). (See Fig. 11).

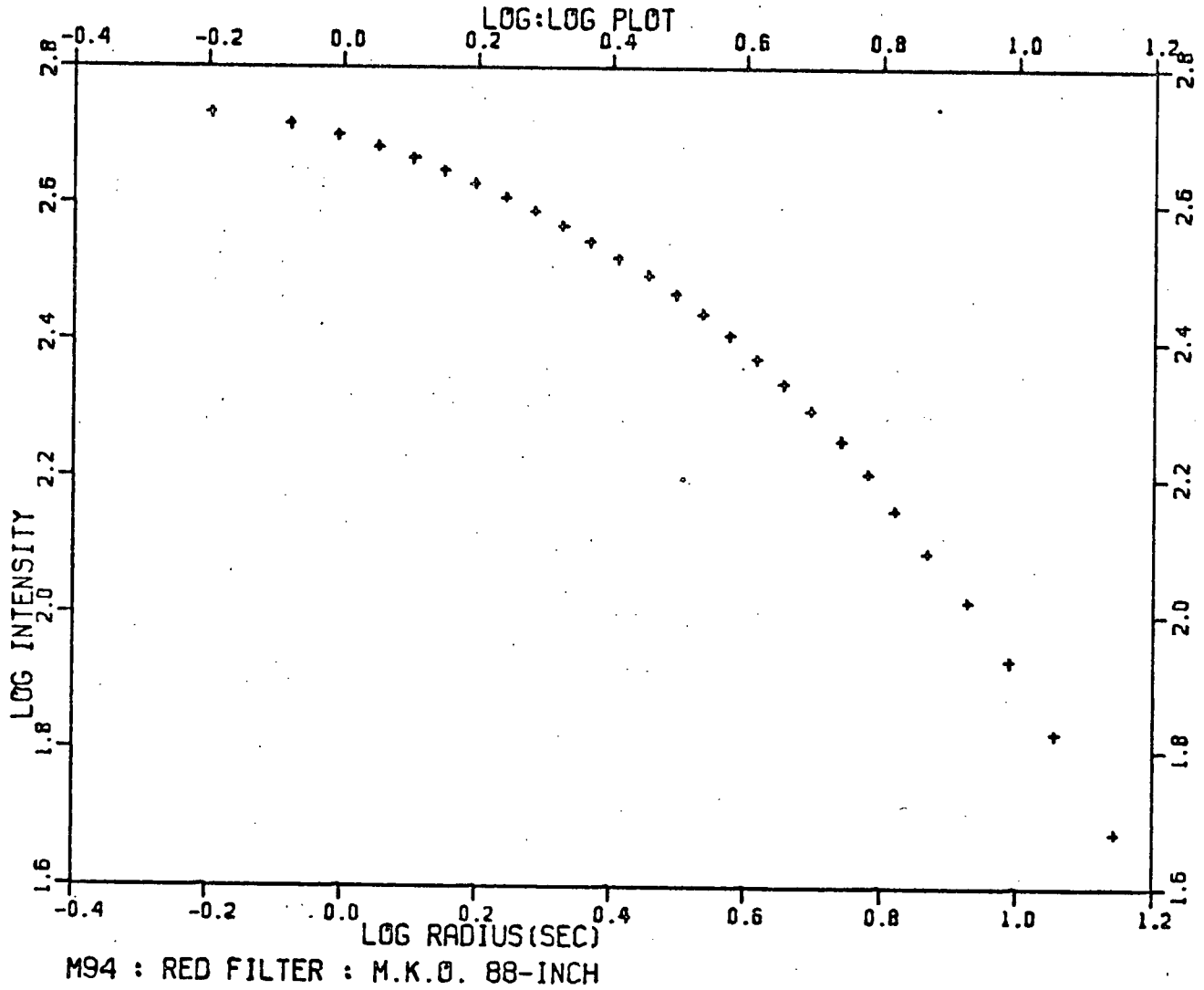

FIGURE 19. NGC 4736: Log(intensity) versus log(radius), red filter.

TABLE X . Blue surface brightness contours for NGC 4736. All units are in the instrumental system.

Surface Brightness	Effective Radius	Centroid x	Centroid y
187.5	0.708	25.62	26.42
177.6	1.025	25.56	26.46
167.8	1.324	25.50	26.52
157.9	1.613	25.45	26.54
148.1	1.907	25.40	26.54
138.2	2.209	25.39	26.56
128.3	2.553	25.40	26.61
118.5	2.941	25.41	26.60
108.6	3.359	25.43	26.57
98.8	3.789	25.45	26.56
88.9	4.392	25.53	26.56
79.0	5.131	25.69	26.42
69.2	6.013	25.95	26.32
59.3	6.853	26.09	26.29
49.5	8.100	26.34	26.35
39.6	9.860	26.56	26.29
29.7	12.391	26.20	25.20
19.9	16.281	25.34	24.48

TABLE XI . Visual surface brightness contours for NGC 4736. All units are in the instrumental system.

Surface Brightness	Effective Radius	Centroid x	Centroid y
290.4	0.573	26.20	26.18
279.8	0.763	26.23	26.14
269.2	0.940	26.25	26.17
258.6	1.108	26.27	26.19
248.0	1.274	26.27	26.20
237.4	1.446	26.27	26.22
226.9	1.636	26.26	26.25
216.3	1.841	26.25	26.29
205.7	2.077	26.23	26.33
195.1	2.323	26.19	26.36
184.5	2.596	26.13	26.36
173.9	2.878	26.08	26.33
163.3	3.176	26.04	26.33
152.7	3.532	26.08	26.33
142.1	3.918	26.14	26.28
131.5	4.345	26.25	26.22
120.9	4.835	26.34	26.14
110.3	5.461	26.52	26.04
99.7	6.135	26.49	25.97
89.2	6.741	26.59	25.99
78.6	7.413	26.71	26.01
68.0	8.341	26.69	26.09
57.4	9.649	26.82	26.07
36.2	13.324	26.40	25.01
25.6	16.383	25.45	24.79

TABLE XII . Red surface brightness contours for NGC 4736. All units are in the instrumental system.

Surface Brightness	Effective Radius	Centroid x	Centroid y
541.1	0.757	28.50	28.84
522.2	0.994	28.51	28.94
503.2	1.170	28.53	28.96
484.2	1.344	28.56	28.98
465.3	1.515	28.58	29.00
446.3	1.685	28.61	29.02
427.3	1.869	28.65	29.04
408.4	2.075	28.65	29.06
389.4	2.292	28.63	29.06
370.4	2.524	28.58	29.06
351.4	2.772	28.51	29.05
332.5	3.058	28.49	29.04
313.5	3.389	28.52	29.03
294.5	3.725	28.56	29.01
275.6	4.089	28.57	28.99
256.6	4.485	28.56	28.96
237.6	4.918	28.61	28.93
218.7	5.390	28.71	28.93
199.7	5.906	28.79	28.92
180.7	6.547	28.93	28.93
161.8	7.187	29.00	28.93
142.8	7.865	29.07	28.95
123.8	8.779	29.03	28.91
104.8	10.089	29.06	28.75
85.9	11.628	28.98	28.48
66.9	13.564	28.74	28.12
47.9	16.582	28.06	27.96

TABLE XIII . Calibrated V surface brightness, versus effective radius for NGC 4736. Errors are calculated from flat field and baseline uncertainties.

Radius (arcsec)	V (mag arcsec^{-2})
0.51	15.03±0.03
0.68	15.07
0.84	15.12
0.99	15.16
1.13	15.20
1.28	15.25
1.46	15.30
1.64	15.35
1.85	15.41
2.07	15.46
2.31	15.53
2.56	15.59
2.83	15.66
3.14	15.73
3.49	15.81
3.87	15.89
4.30	15.98
4.86	16.08
5.46	16.19±0.04
6.00	16.31
6.60	16.45
7.42	16.61±0.05
8.59	16.79
10.08	17.01±0.06
11.86	17.29±0.09
14.58	17.67±0.12

law holds. Figure 20 shows that in the innermost region the plot is not linear, and that the observations do not extend out far enough for a straight line to be drawn through a significant range of values. Some of the curvature is due to seeing, and it cannot be said whether de Vaucouleurs' empirical law holds for NGC 4736 or not. It should be recalled that this law does appear to hold over the entire bulge of M31 (de Vaucouleurs 1975), a galaxy with many similarities to NGC 4736.

It is obvious that the contour area technique gives very smooth surface brightness curves. Experiments show that if the pictures are smoothed using a convolution filter prior to computation of the contours, the same surface brightness curves are obtained, except in the innermost two or three seconds of arc where smoothing degrades the resolution of the "semi-stellar" nucleus.

It can be seen from the maps that the contours are somewhat non-circular and are not aligned with the major axis or line of nodes of the galaxy as a whole. The major axis of the system is taken to be at position angle 122±3 degrees (Schommer and Sullivan 1976). Bosma, van der Hulst and Sullivan (1977) discuss the apparent change with radius of the position angle of the line of nodes of NGC 4736. In addition, a difference of about 15° was observed by them between the apparent minor axis of the optical body and the kinematical minor axis derived from HI observations.

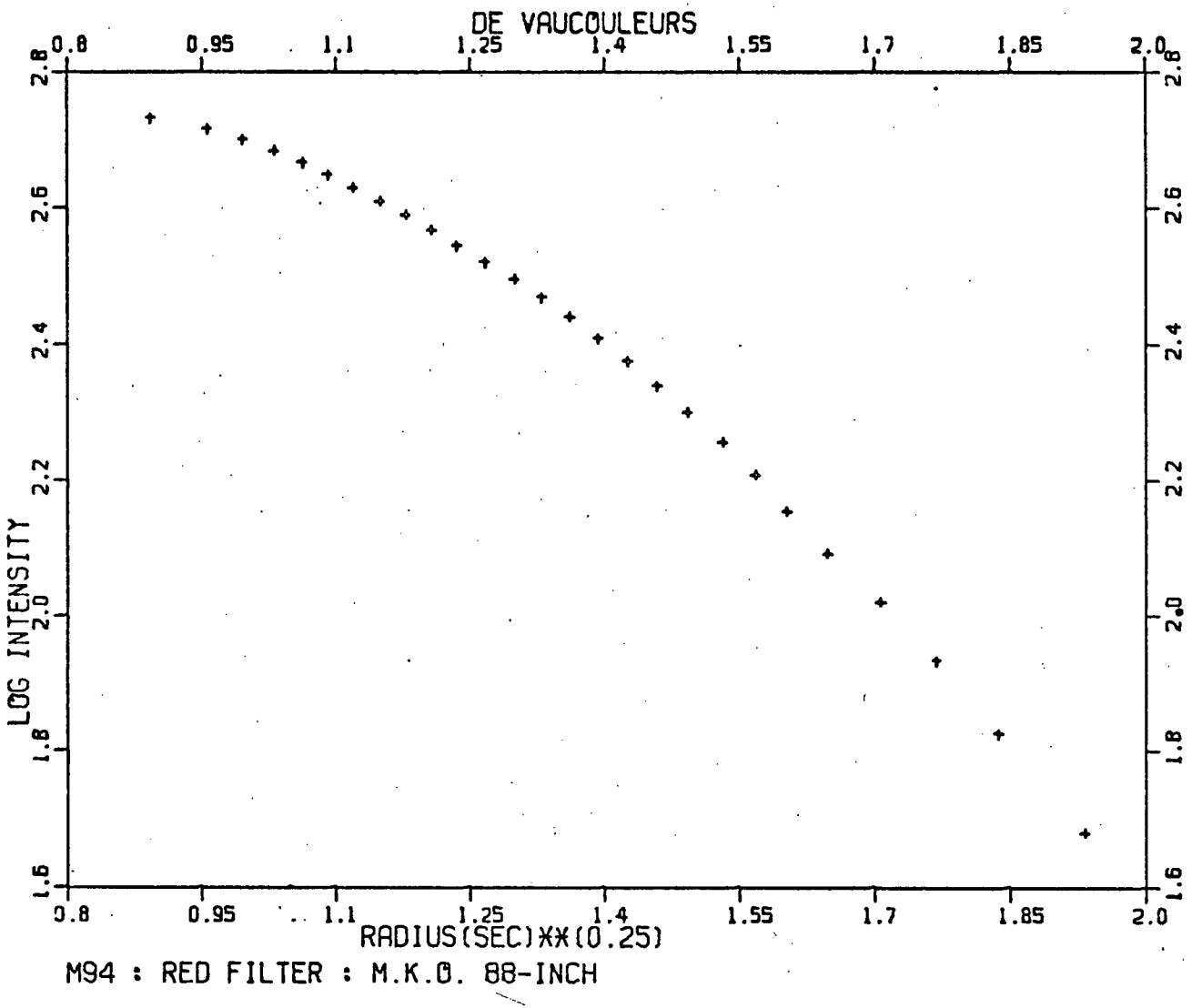

FIGURE 20. NGC 4736: Log(intensity) versus (radius)$^{0.25}$, red filter. De Vaucouleurs' law is linear in this diagram.

Figure 18 shows that the major axes of some contours may be roughly perpendicular to the major axis of the system. While it is possible to fit ellipses to the contours to derive the ellipticity and position angle of each contour such an approach has not been carried out here because there are more physically meaningful ways of treating the data. Ellipse fitting has been done for M31 (Peterson, Ford and Rubin 1977), and the SB0 galaxy NGC 2950 (Crane 1975). The rather face-on aspect of NGC 4736 and the known presence of dust in its central regions suggest that fitting ellipses to contours may yield confusing results.

<u>The King Model:</u> I have chosen a simple model which can be used to discuss both the photometry and the dynamics of this galaxy. For the central bulge, a simple empirical model is,

$$I(r) = \frac{I(0)}{1 + \left(\frac{r}{r_c}\right)^2} , \qquad (42)$$

as developed by King (1962) for globular clusters, where I(0) is the central surface brightness and r_c is the core radius, at which $I(r_c) = I(0)/2$. A spherical system which has a surface brightness described by equation 42 has a density law corresponding to,

$$\rho(r) = \frac{\rho(0)}{\left\{1 + \left(\frac{r}{r_c}\right)^2\right\}^{3/2}} , \qquad (43)$$

assuming that the mass-to luminosity ratio M/L is constant, an assumption to which I shall return later. The central surface

brightness and the central density are then related by

$$I(0) = 2\rho(0)\, r_c \left(\mathcal{M}/\mathcal{L}\right)^{-1} . \tag{44}$$

As a starting point, this model has many useful features. In the limit for large r, it tends to Hubble's inverse square surface brightness law for elliptical galaxies (Hubble 1930). For small radii, it closely follows the isothermal model. Equation (43) gives a good fit out to 10 isothermal scale lengths, where the scale length α is given by,

$$\alpha = \left[\frac{v^2}{4\pi G \rho(0)} \right]^{1/2} , \tag{45}$$

where v^2 is the mean square velocity dispersion in the line of sight. Since King (1966b) has shown that

$$r_c = 3.0\, \alpha , \tag{46}$$

this means that the run of density in the isothermal model and equation (43) agree very closely for $r \leqslant 3r_c$.

The agreement of equation (42) with King's isothermal cut-off models and with de Vaucouleurs's empirical model extends to greater radii (King 1966b). Empirically, there is fairly good evidence to assume $\rho(r) \propto r^{-3}$ for the bulges of spiral galaxies. Oort and Plaut (1975) have shown such a relationship to hold for RR Lyrae variables in the Galaxy, with an axial ratio of the spheroidal system between 0.8 and 1 (i.e. nearly spherical). This can be taken to be similar to

the run of the total bulge and halo density (Schmidt 1976).

Since NGC 4736 is probably similar to the Galaxy, and recalling that the ellipticity of the inner surface brightness contours is small and that the major axes are not along the line of nodes, I assume a circularly symmetrical surface brightness law as given by equation (42). All the light at the centre is assumed to come from the bulge system. After fitting to the observed surface brightness versus effective radius for the inner region, the model is subtracted point by point from the observed image to obtain a map of residuals.

The fitting was done by plotting 1/I versus $(r_I^*)^2$ so that a linear equation obtains,

$$\frac{1}{I(r)} = \frac{1}{I(0)} + \frac{1}{I(0)\, r_c^2} \cdot r^2 \quad . \qquad (47)$$

The intercept is equal to 1/I(0) and the slope equals $1/\{I(0)\, r_c^2\}$. This graphical procedure was demonstrated by King (1962, Fig. 4). Figures 21, 22 and 23 show I^{-1} versus r^2 in the blue, visual and red filters, using the data of Tables X, XI and XII. The dip for small radii below the linear extrapolation of the upper part of the curve is due to the so-called "semi-stellar nucleus", which is not predicted by King's theory. I therefore do not use this portion in determining I(0) and r_c .

The red contours and the contours of a composite image

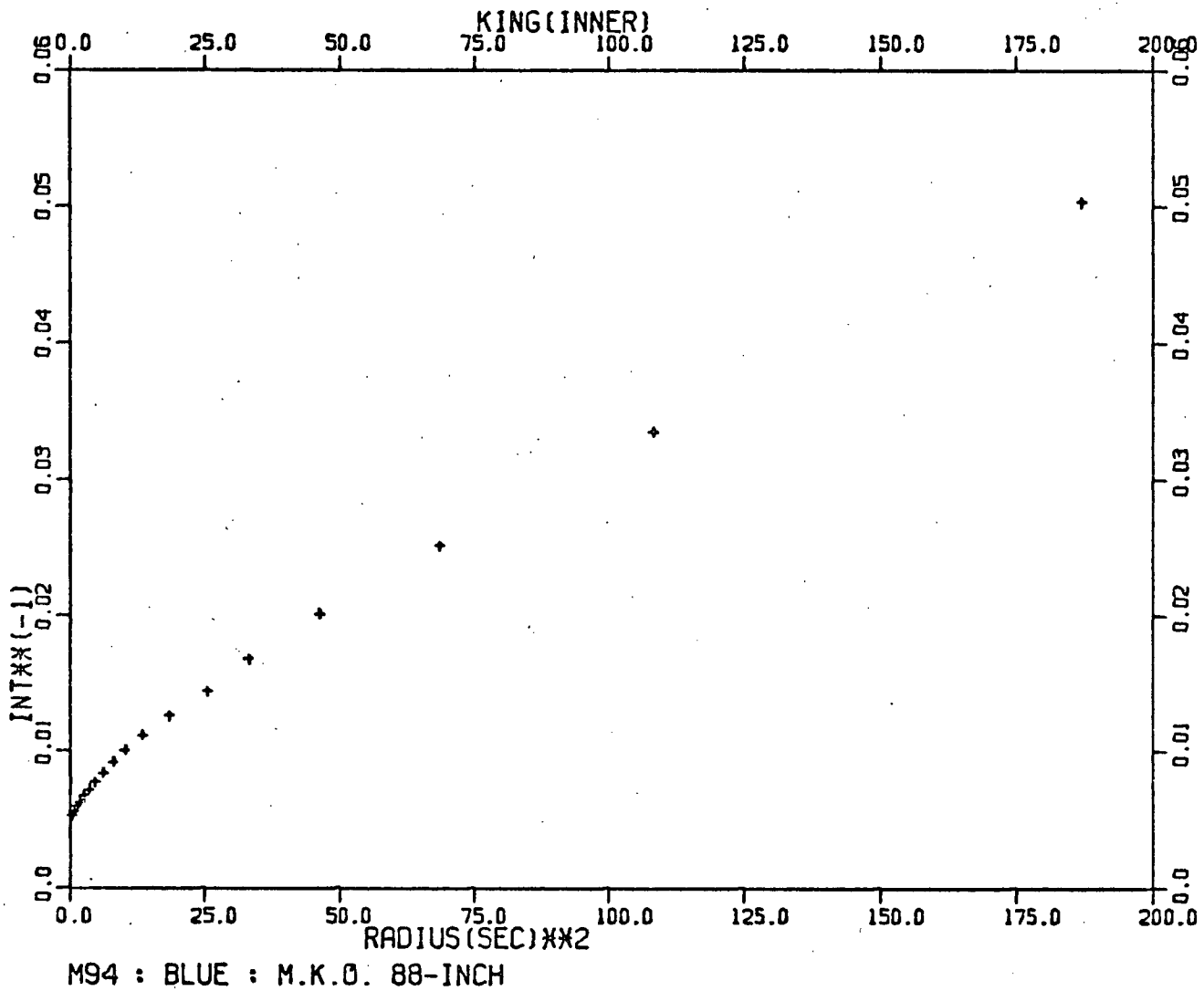

FIGURE 21. NGC 4736: (Intensity)$^{-1}$ versus (radius)^2, blue filter. King's law is linear in this diagram.

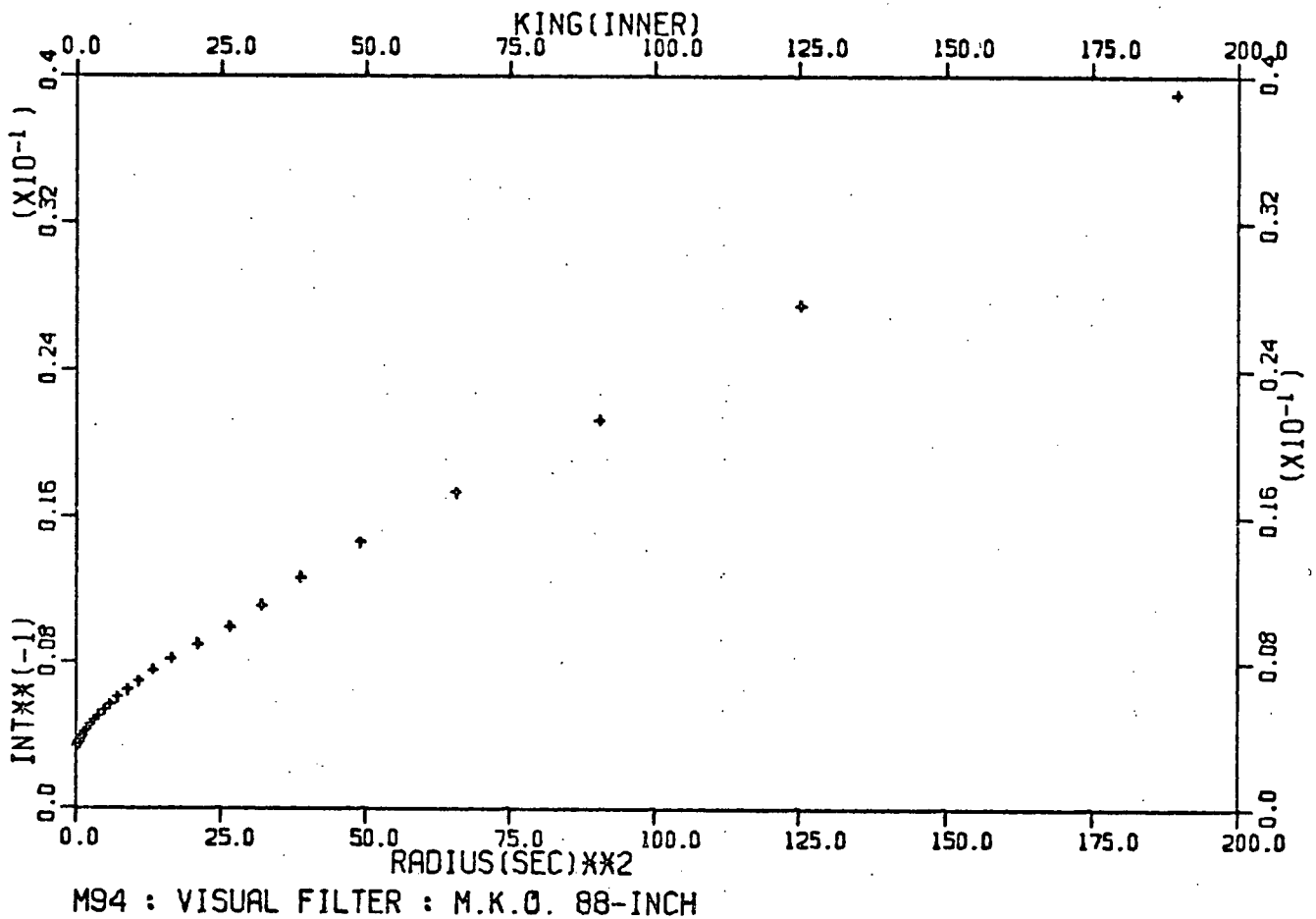

FIGURE 22. NGC 4736: (Intensity)$^{-1}$ versus (radius)^{2}, visual filter.

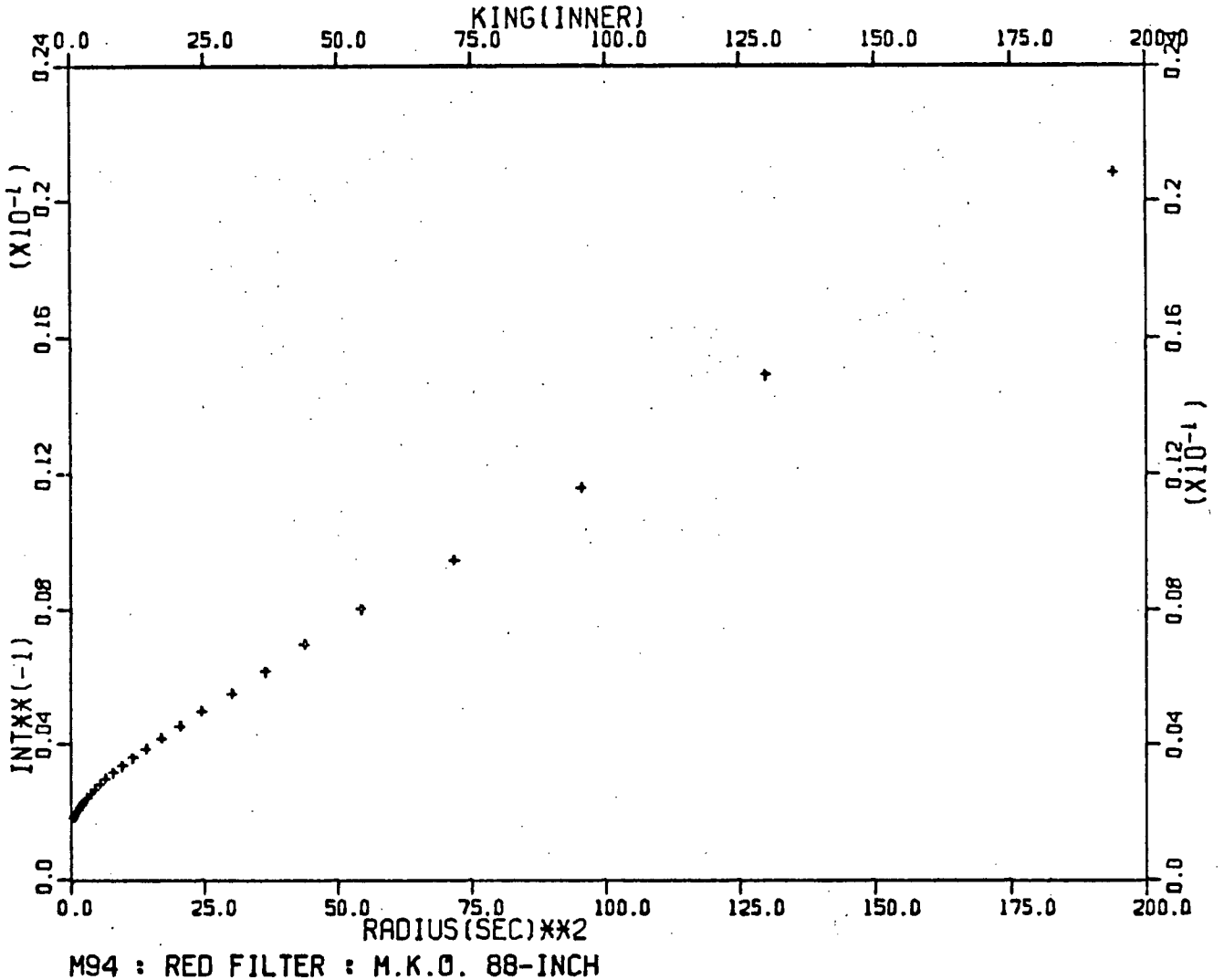

FIGURE 23. NGC 4736: (Intensity)$^{-1}$ versus (radius)^2, red filter.

(made up from summing the registered forms of the blue, visual and red images) give a core radius of 6.7±0.4 (est. error) diode units. At 0.89±0.02 arc seconds per diode, this corresponds to r = 6."0±0."5. The central intensities I(0) were estimated graphically, and the circular simple King distributions were computed and subtracted from each image. The contours of the residuals are depicted in Figures 24 to 28.

A Generalized Hubble Model

Another empirical model for spheroidal systems is due to Hubble (1930),

$$I(r) = \frac{I(0)}{\left(1 + \frac{r}{a}\right)^2}, \tag{48}$$

which can be compared more clearly with the simple King relationship if one writes,

$$I(r) = \frac{I(0)}{1 + 2\left(\frac{r}{a}\right) + \left(\frac{r}{a}\right)^2} \tag{49}$$

$$\approx I(0)\left\{1 - 2\left(\frac{r}{a}\right)\right\}, \quad \text{for } r \ll a. \tag{50}$$

This law more nearly attempts to account for the central cusp or nucleus, while the surface brightness of the outer parts of the system follows an inverse square law $I(r) \propto r^{-2}$, as does the King law. Note that Hubble's parameter "a" is the radius at which the surface brightness I(r) has dropped to one

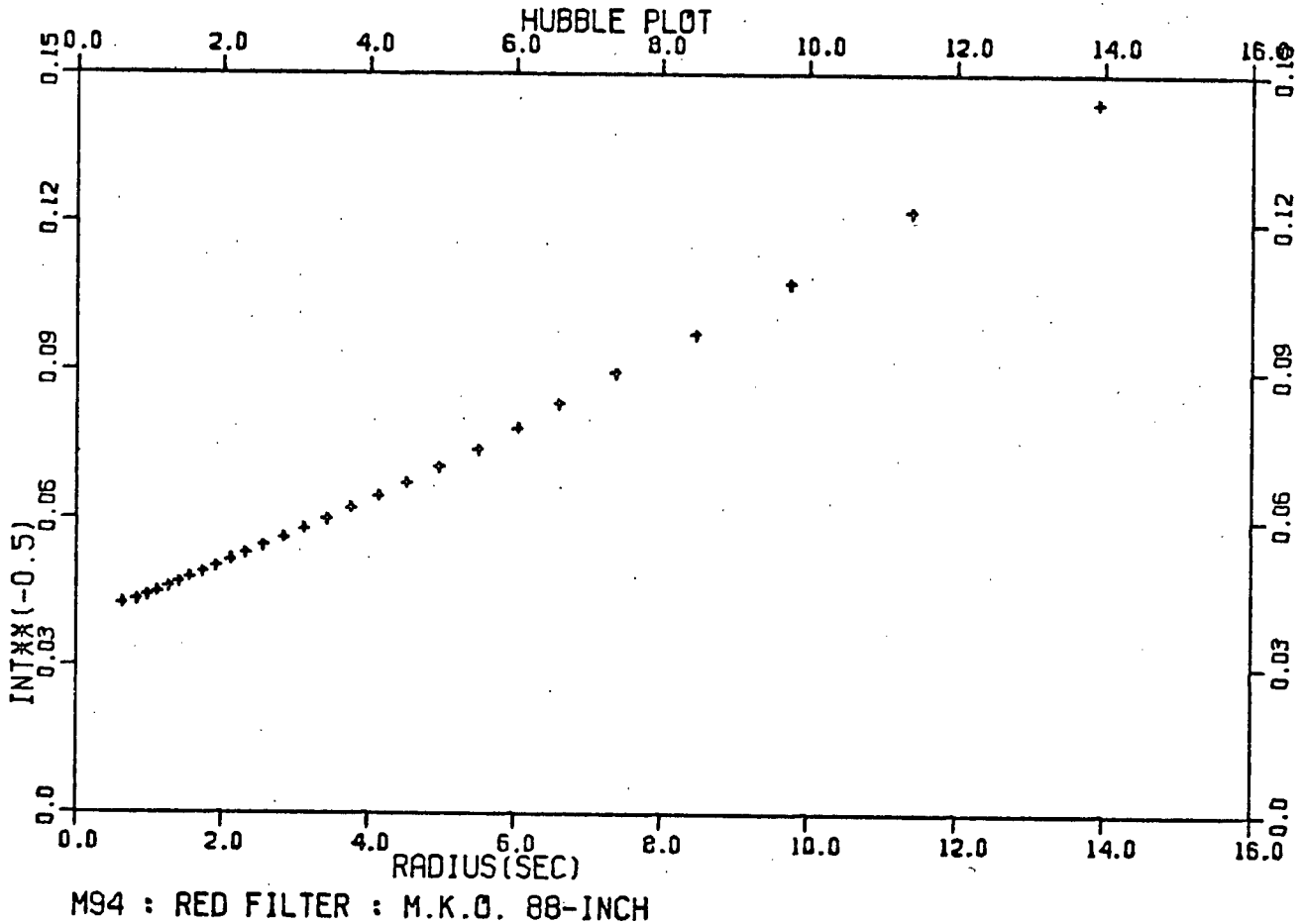

FIGURE 24. NGC 4736 : $(\text{Intensity})^{-0.5}$ versus (radius), red filter. Hubble's surface brightness law for galaxies is linear in this diagram.

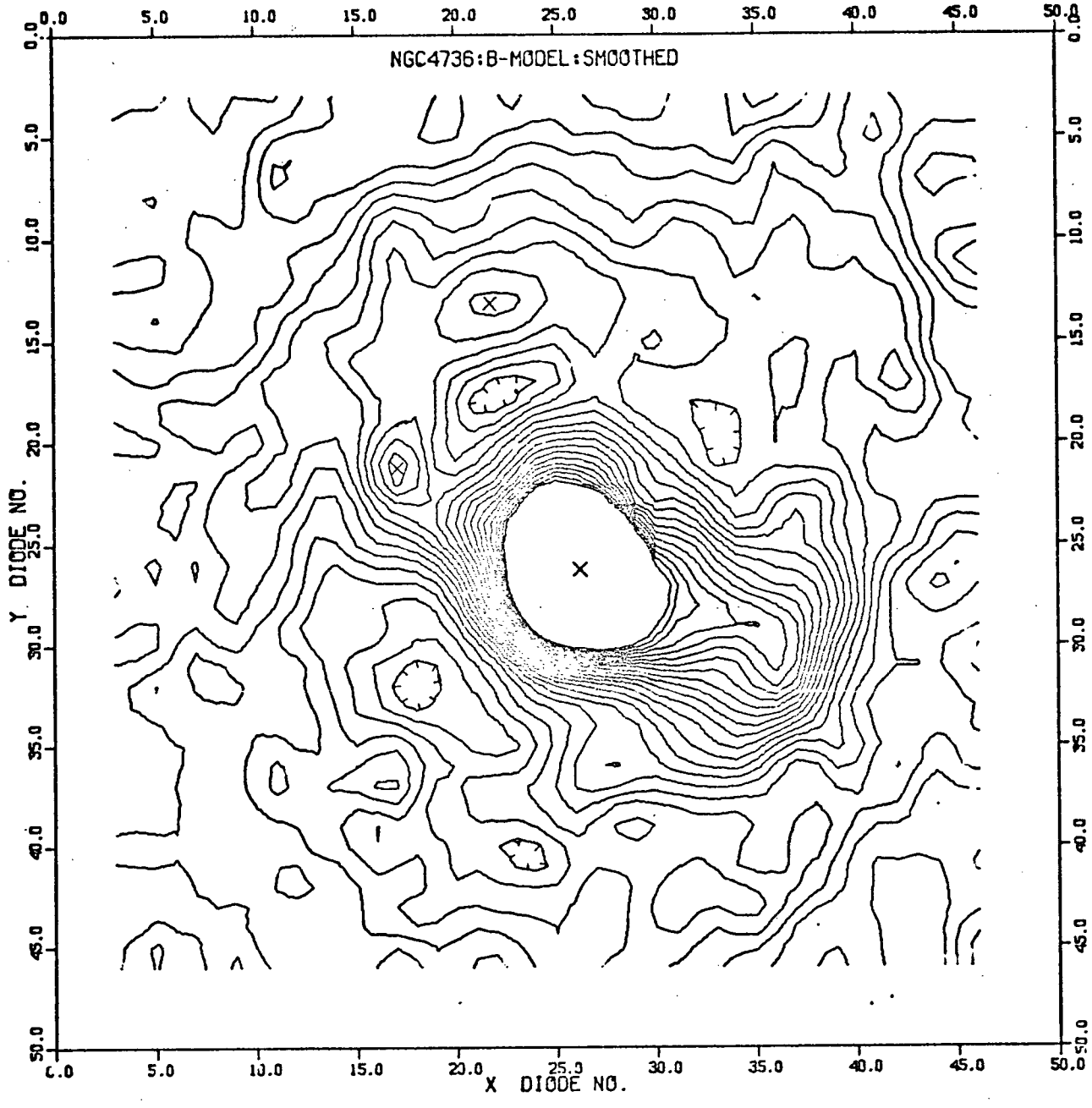

FIGURE 25. Blue minus simple King model. Equal intensity increments between contours. Image shifted into registration with V image. Peaks marked by 'X', minima are inside tick-marked contours. Central contours left unplotted for clarity. North is to the right (X), East is down (Y). (See Fig. 11).

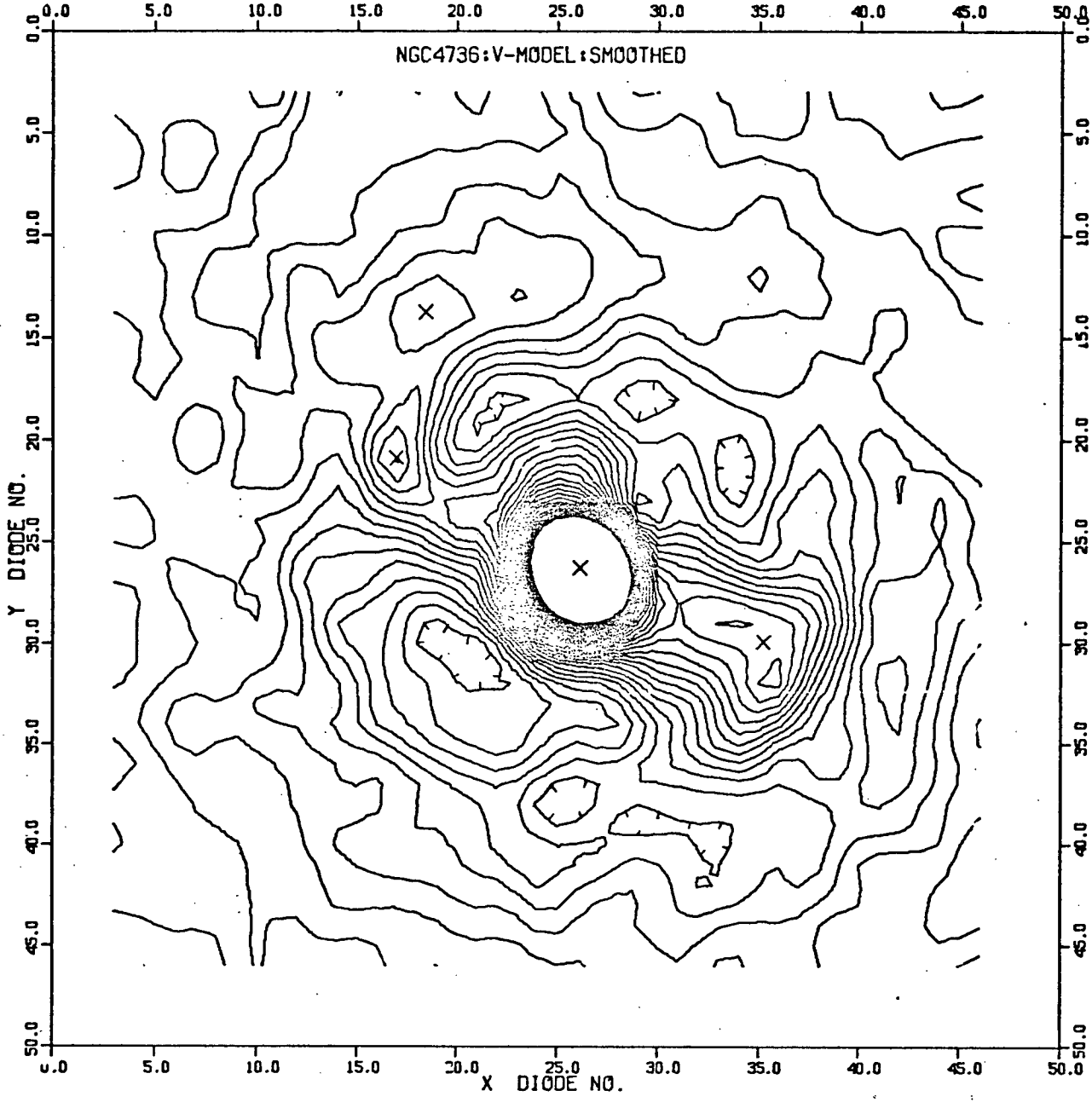

FIGURE 26. Visual minus simple King model. Notation as for Fig. 25.

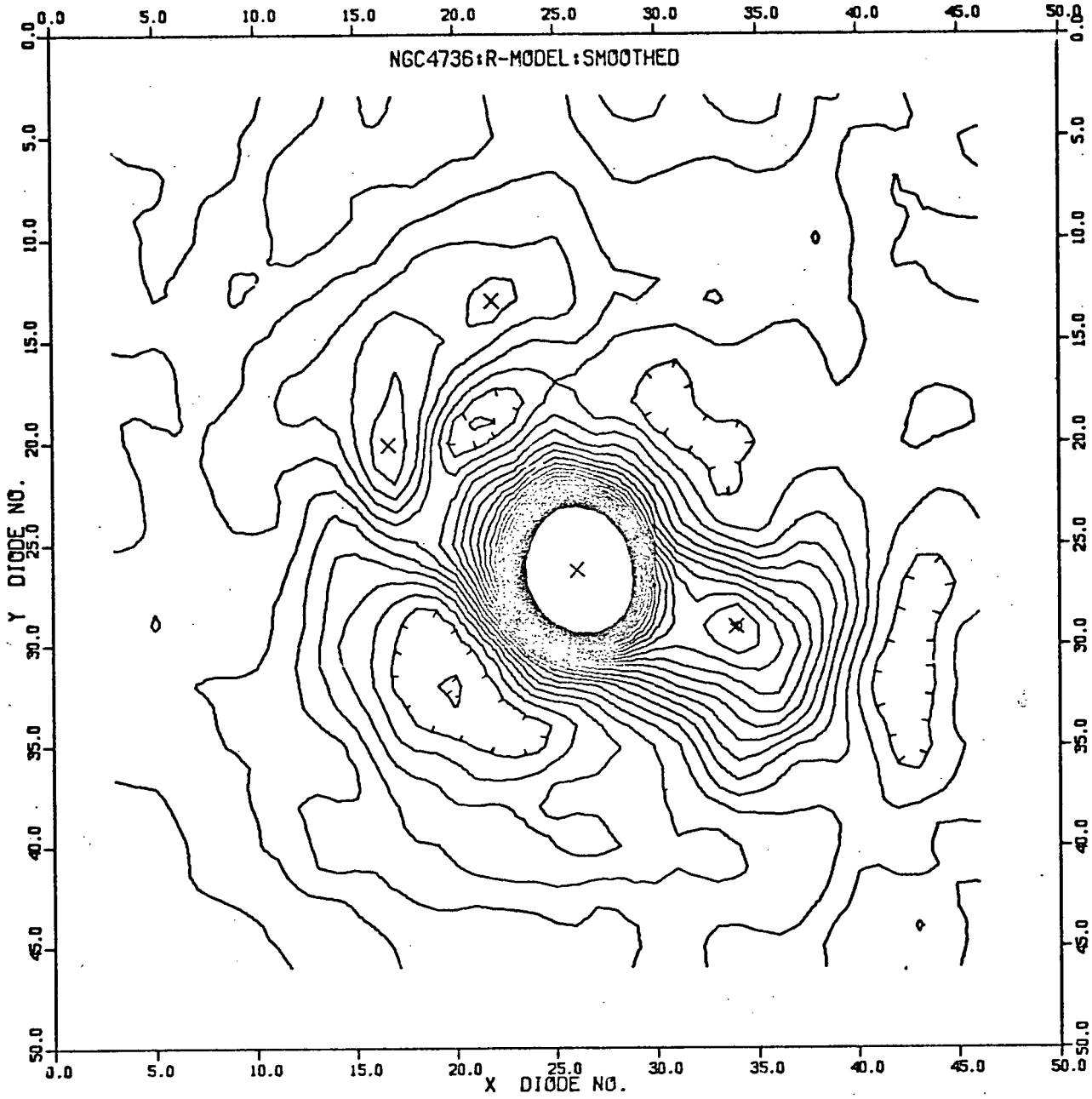

FIGURE 27. Red minus simple King model. Notation as for Fig. 25. Image shifted into registration with V image.

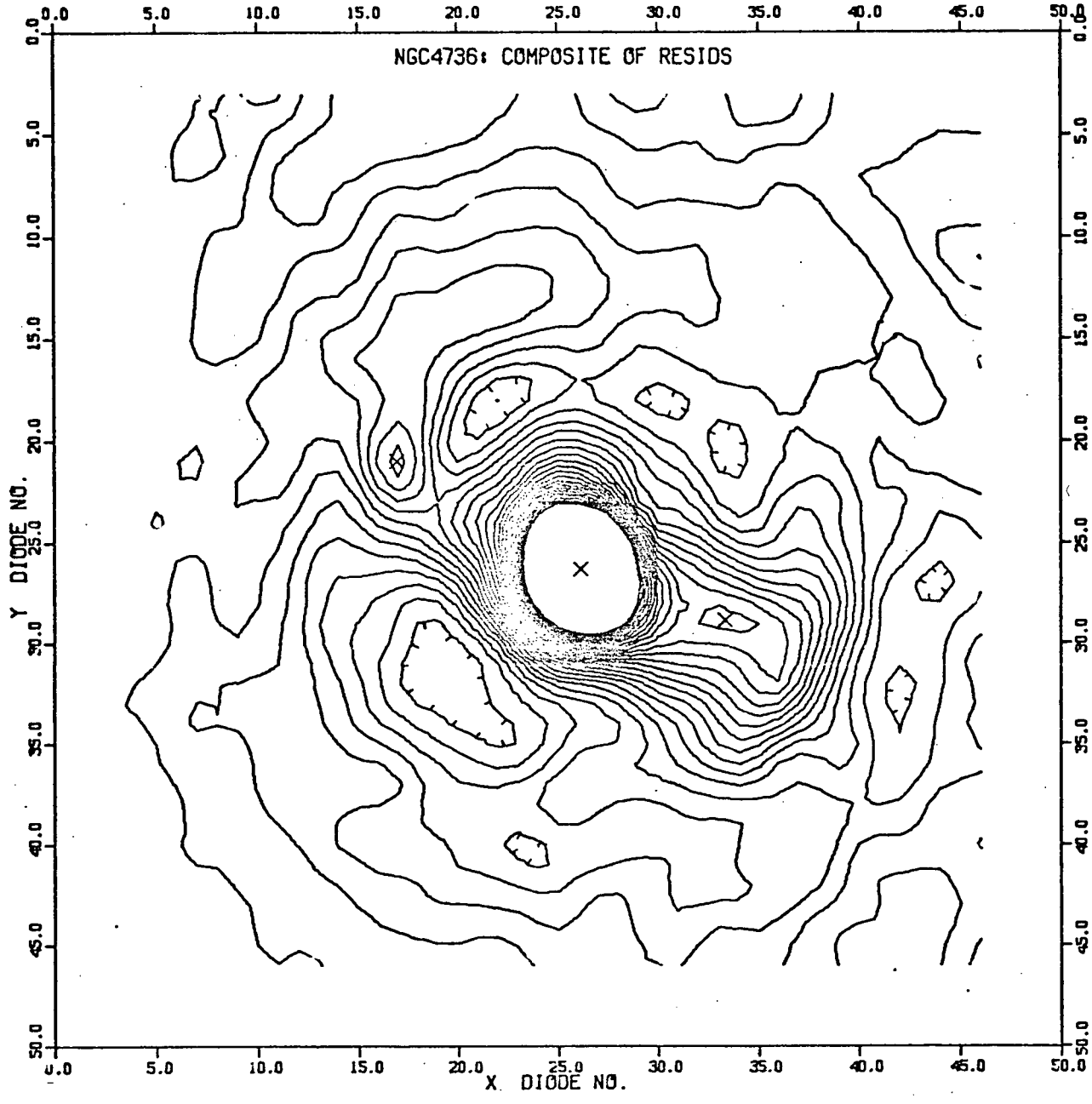

FIGURE 28. Composite of residuals from simple King model. Notation same as for Figures 25-27.

quarter of its central value I(0). Equation (49) can be written in the form,

$$\frac{1}{\sqrt{I(r)}} = \frac{1}{\sqrt{I(0)}} + \frac{1}{a\sqrt{I(0)}}\, r \quad , \qquad (51)$$

so that plotting $1/\sqrt{I(r)}$ versus r should give a straight line of the Hubble law holds. Figure 24 illustrates such a plot for the red contours of NGC 4736. It would appear that the nuclear surface brightness is over-estimated by the Hubble law. A generalized Hubble law can be written as,

$$I(r) = \frac{I(0)}{1 + c_1\left(\frac{r}{a}\right) + \left(\frac{r}{a}\right)^2} \quad , \qquad (52)$$

where c is some constant. Least-squares fits were made to the data in Tables X to XII to evaluate I(0), a and c_1 for each image. Circularly-symmetric models of the surface brightness computed using equation (52) were subtracted from each image. These residual maps are discussed in the next section.

4.4 NGC 4736: Halftone Residual Maps.

The residual maps obtained by subtracting simple circular King and generalized Hubble models from images of NGC 4736 have also been reproduced using the graphics facilities of the Dominion Radio Astrophysical Observatory, Penticton. Figure 29 shows an electrostatic printer dot-density plot of the red image minus a simple King model. The same data is shown in Figure 30, using a Raytheon half-tone plotter, together with

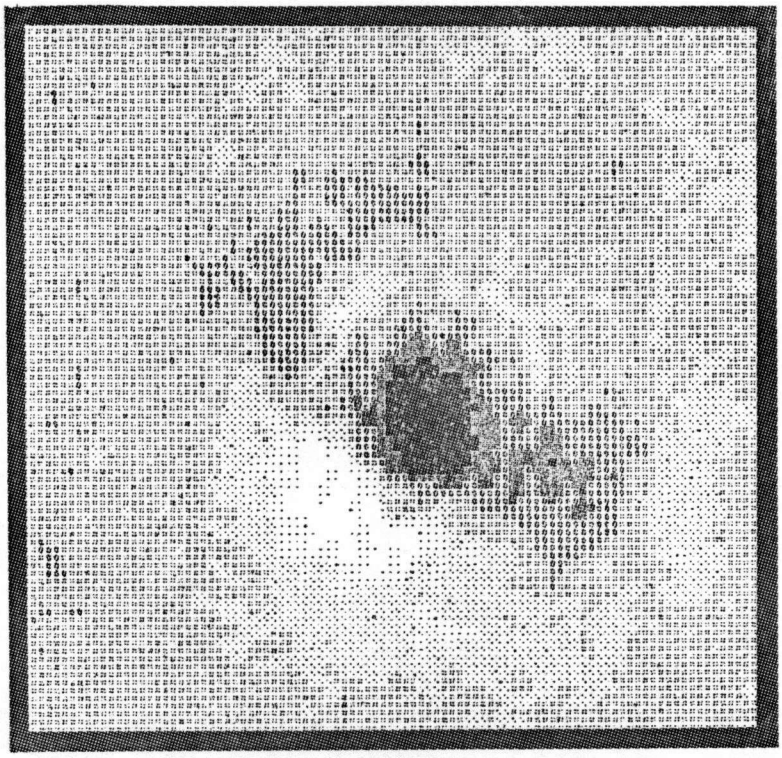

FIGURE 29. Red image minus simple King model: dot-density plot (Versatec electrostatic printer plotter: 8 intensity levels plotted).

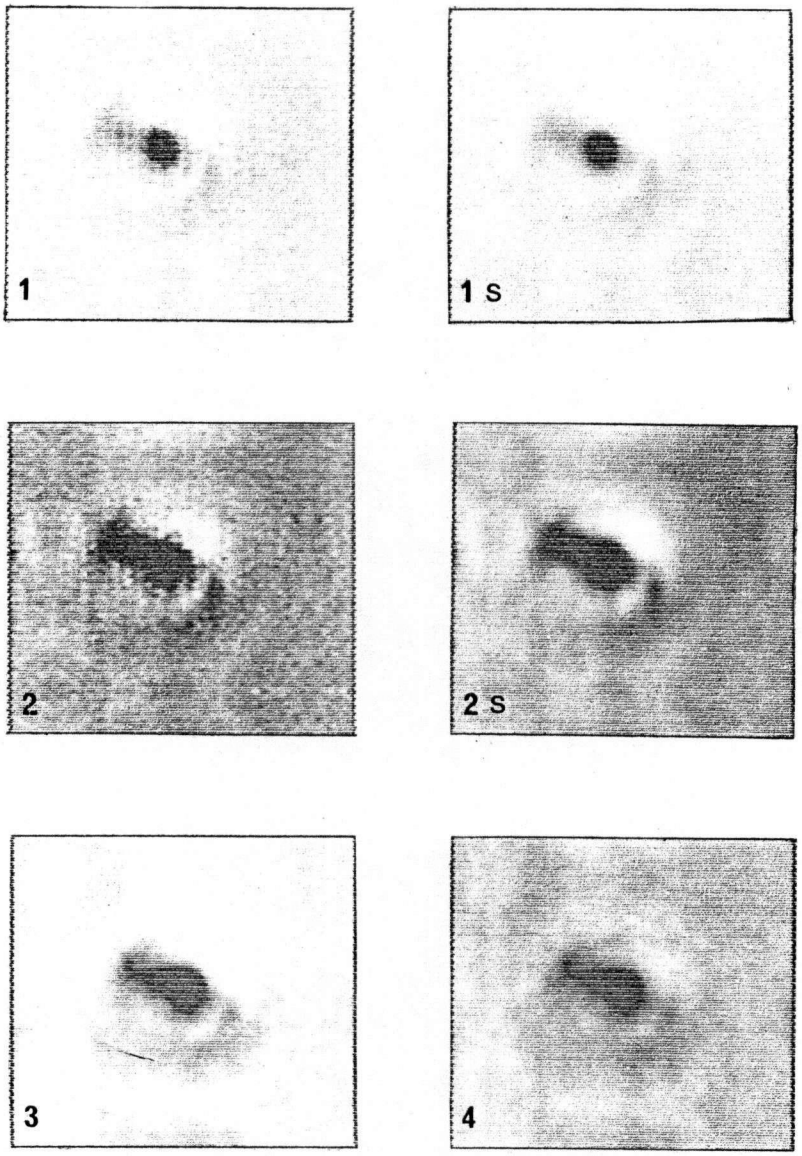

FIGURE 30. NGC 4736 Minus Simple King Model.

1. Red minus model:low contrast.
1s. Image 1 smoothed.
2. Red minus model: high contrast.
2s. Image 2 smoothed.
3. Blue minus model, smoothed.
4. Blue minus model, smoothed, lower cut-off.

Note: Approximately 1/4 inch band around edges is redundant. Orientation rotated by 180° from contour maps.

blue data. Smoothed and unsmoothed versions are shown with the effect of different contrast factors.

A high-resolution Raytheon plot of the red image minus a generalized Hubble model is shown in Figure 31. Lower resolution unsmoothed residual maps are shown in Figure 32, using different contrast factors. The contrast is set to 100 levels of gray with specified minimum white and maximum (black) levels.

In all these residual maps, a bar like structure of about 20 arc seconds length is evident, orientated at a position angle of roughly 30 degrees.

The residual "nucleus" is plotted on a Gaussian scale in Figure 12. The straight line fit gives a Gaussian 1/e diameter of 5.0 arc seconds for the composite map of residuals, corrected for the slight broadening introduced by smoothing. This compares with the 2.9 to 3.7 arc second seeing disk for the shorter one minute star exposures of a star. Since the seeing may have been worse for the longer exposure, and also since the residual nucleus has a rather Gaussian surface brightness distribution, the nucleus cannot be said to be definitely resolved.

The integrated V magnitude of the residual nucleus can be estimated by summing the excess in the central region, and by applying the calibration of Table IX. This gives V(nucleus) = 13.3. For a distance modulus of 28.9 (corres-

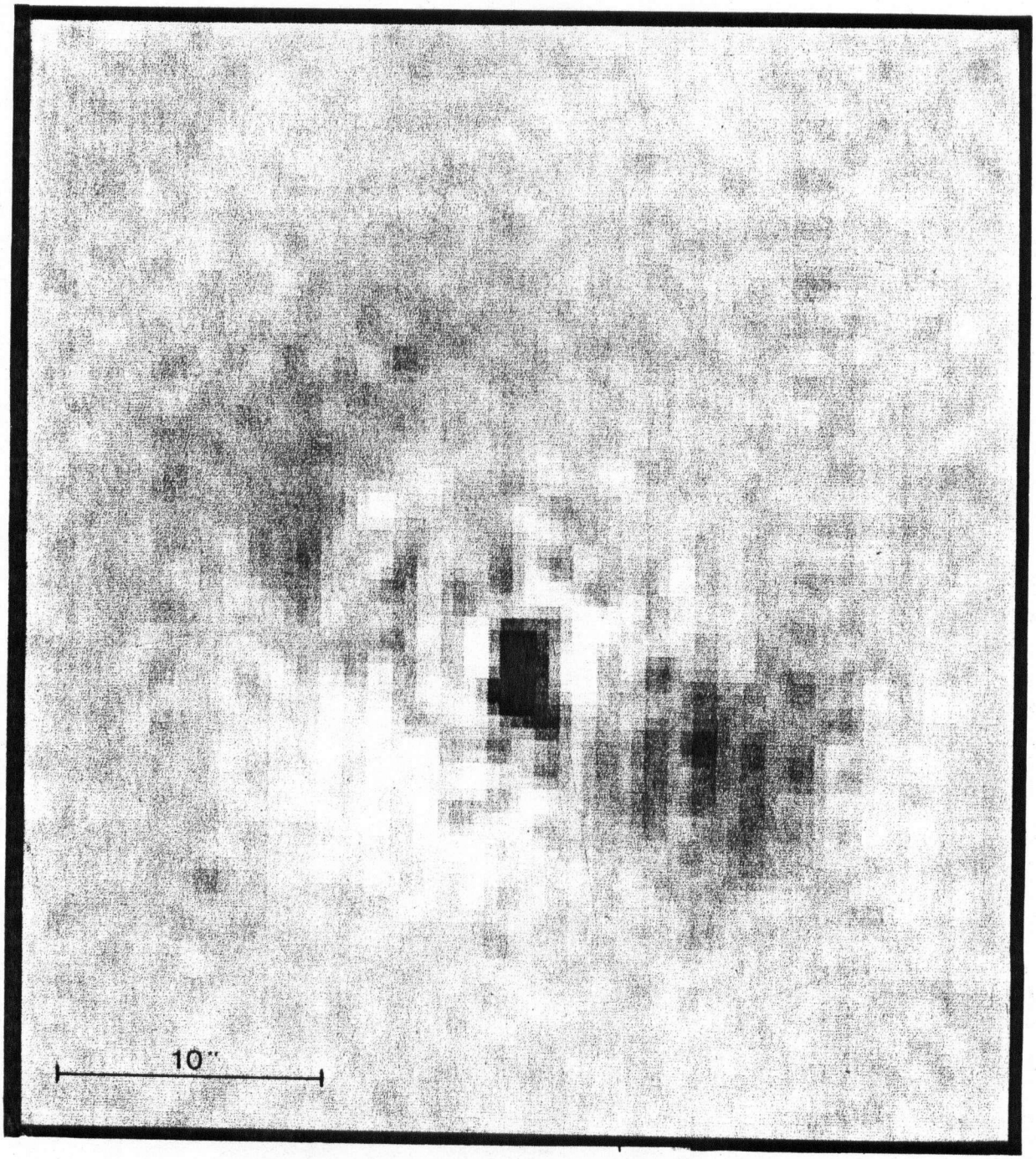

FIGURE 31. Red minus generalized Hubble model. Unsmoothed, high plotter resolution.

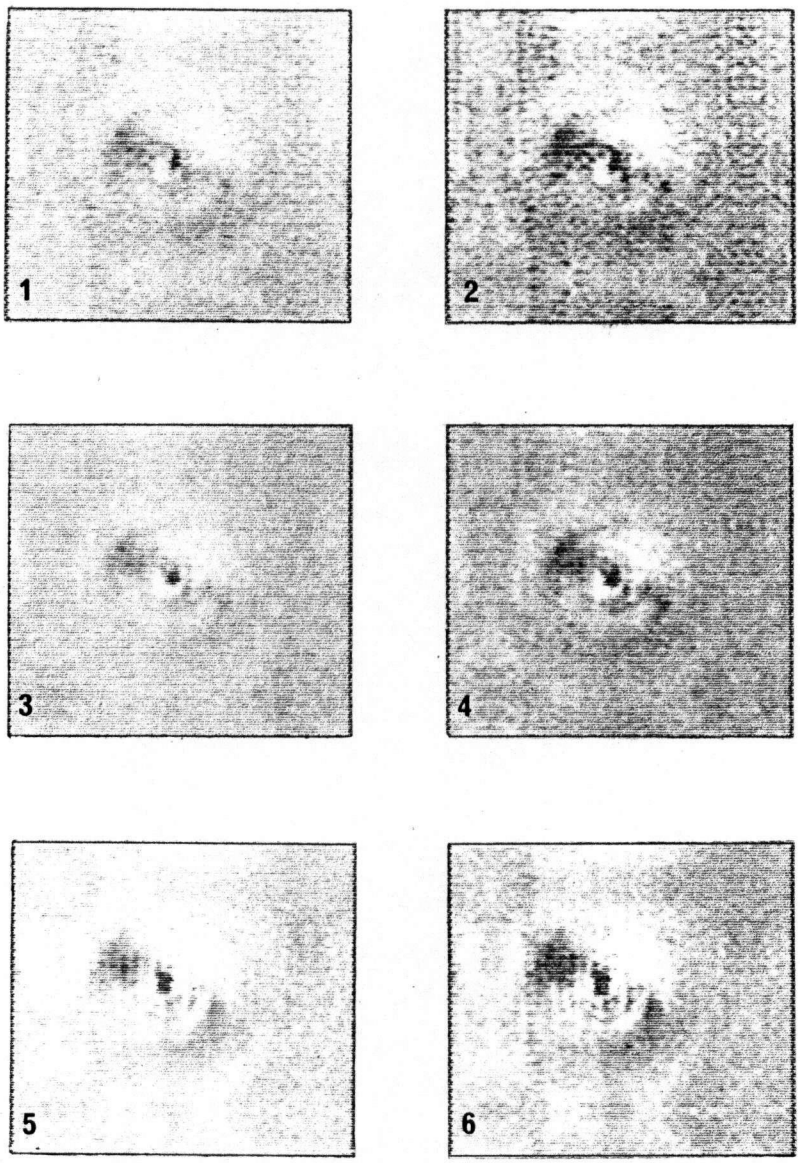

FIGURE 32. NGC 4736 minus generalized Hubble model.

1,2: Blue - model: two contrasts.
3,4: Visual - model: two contrasts.
5,6: Red - model: two contrasts.

Note: Approximately 1/4 inch band around edges is redundant. Orientation rotated by 180° from contour maps.

ponding to a distance of 6 Mpc), the absolute V magnitude is approximately -15.6. In comparison, Light, Danielson and Schwarzschild (1974) obtain $M_V = -12.0$ for the nucleus of M31.

4.5 NGC 4736: Ratio And Colour Maps.

The residual maps presented in Sections 4.4 and 4.5 correspond to linear intensity differences between the observed and computed surface brightness distributions. Since there is a very wide range of surface brightness in each image of the nuclear region of NGC 4736, it is also interesting to see the ratio of the observed and computed distributions. Figures 33, 34 and 35 show the blue, visual and red images divided by the corresponding simple King models. The ends of the bar-like structure are most strongly accentuated, as is the arm-like feature in the North-East quadrant.

The colour maps are shown in Figures 36, 37 and 38. The b, v, and r images were smoothed using a Gaussian of 2.5 diodes diameter. The position of the nucleus listed in Table XIV , was determined from the contour centroids for each image by averaging the positions of contours with radii between 1 and 2 diode units. The blue and red images were brought into registration with the visual image by using the FIRM Fourier transform instruction FT and applying the shift theorem. Small perturbations of less than 0.1 diode spacings to the image registration do not radically change the colour maps.

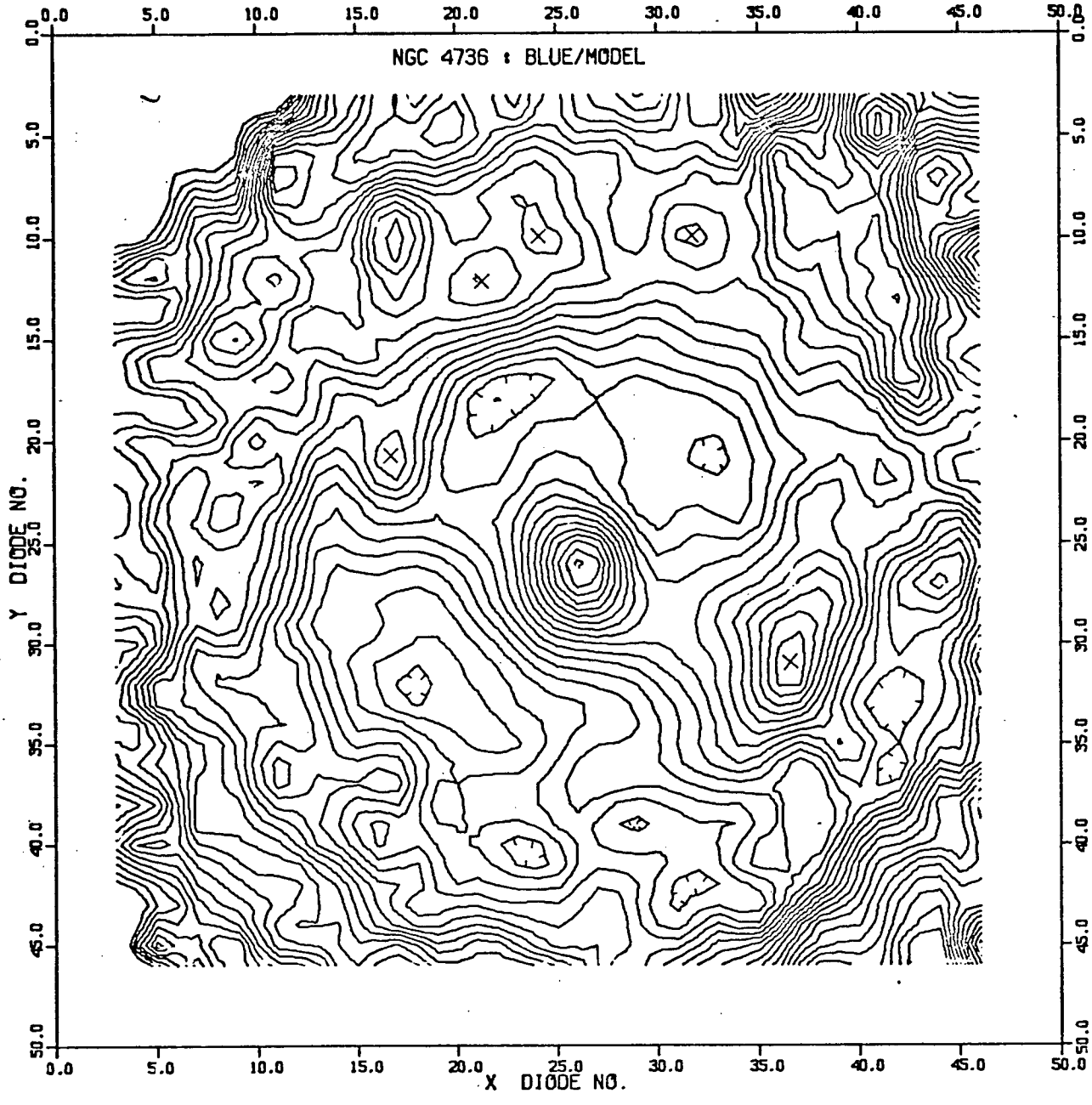

FIGURE 33. NGC 4736: Blue divided by simple King model. Peaks marked by 'X', local minima inside ticked contours. Contours separated by 5%.

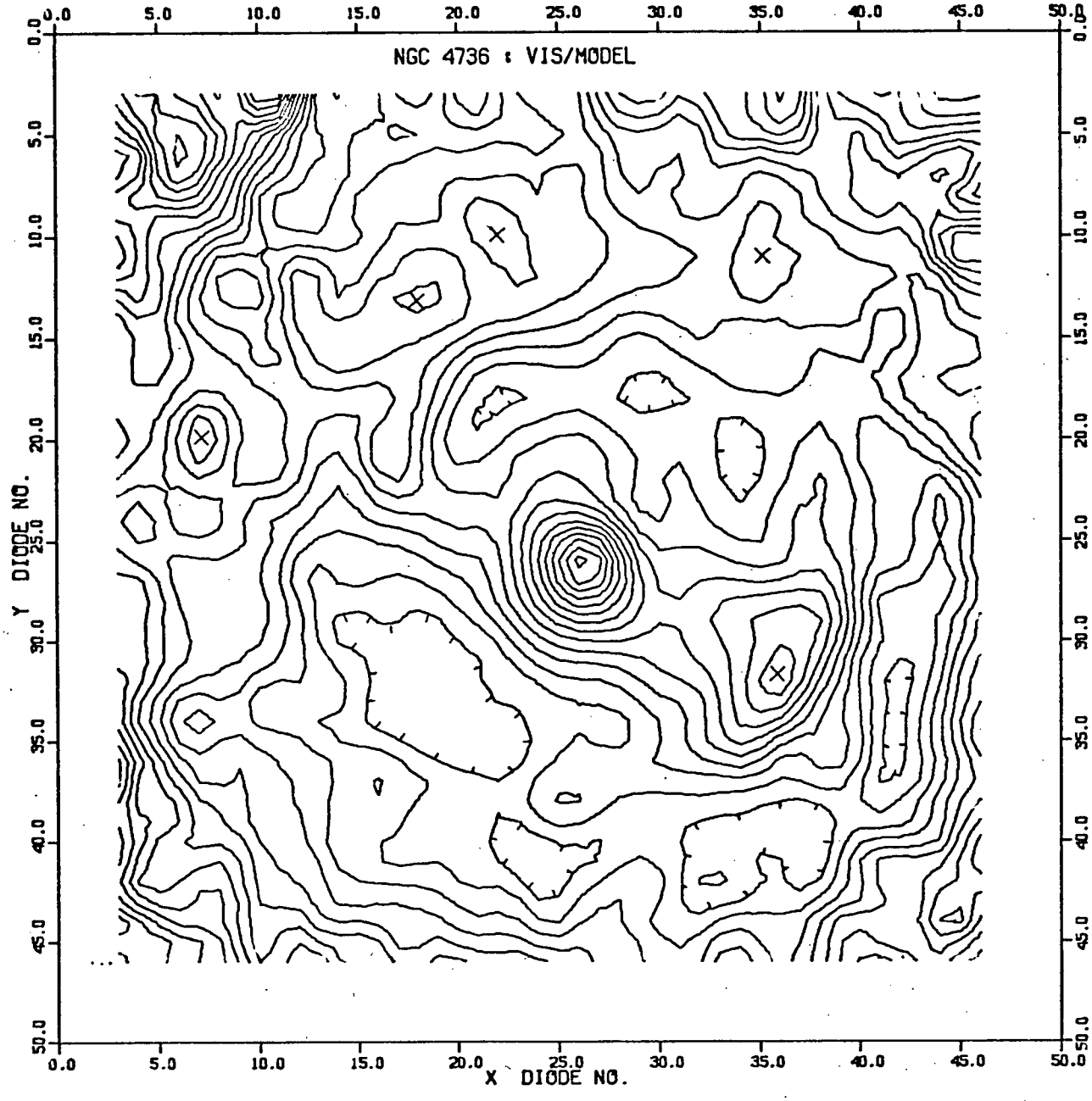

FIGURE 34. NGC 4736: Visual divided by simple King model. Peaks marked by 'X', local minima inside ticked contours. Contours separated by 5%.

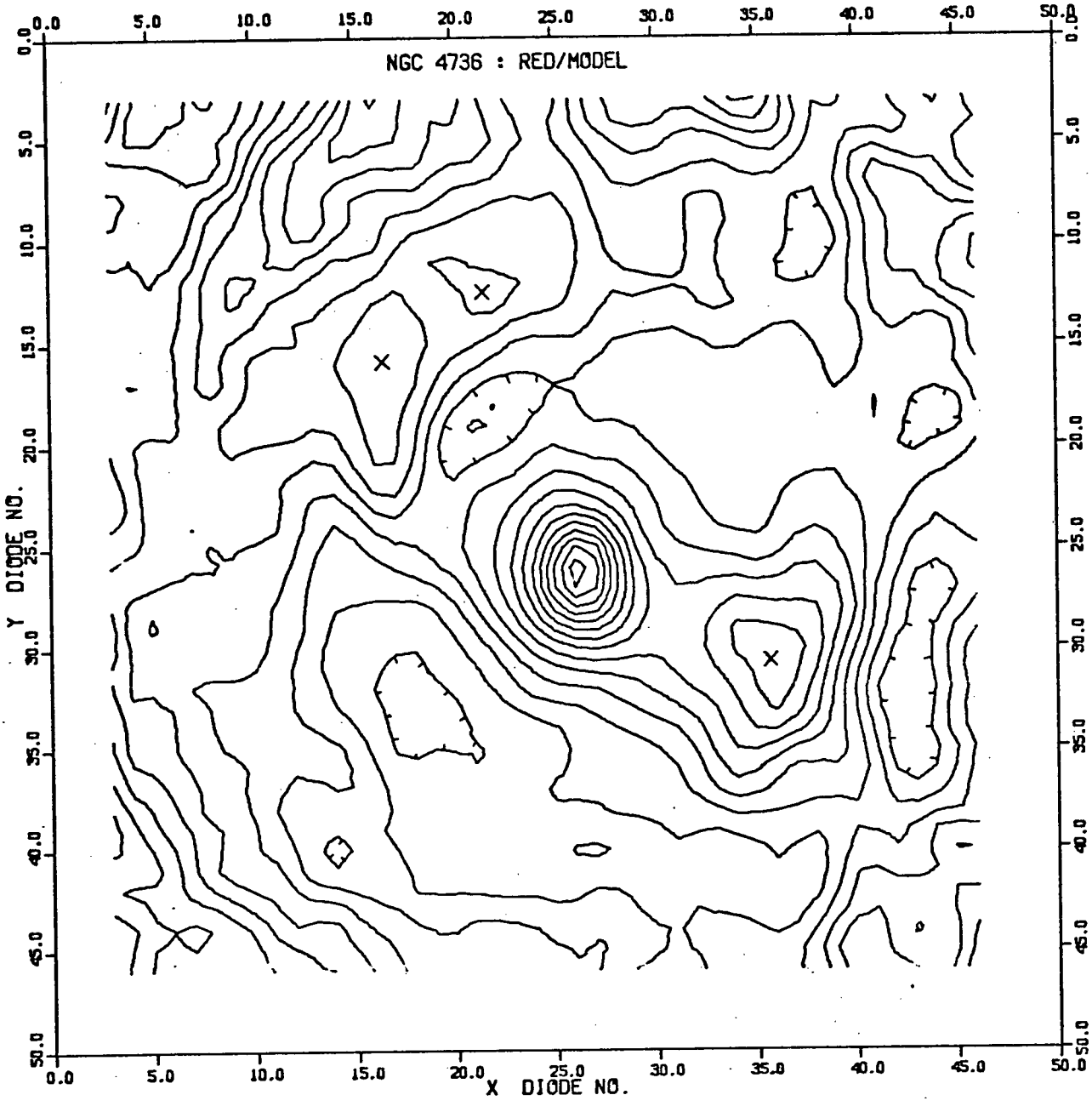

FIGURE 35. NGC 4736: Red divided by simple King model. Peaks marked by 'X', local minima inside ticked contours. Contours separated by 5%.

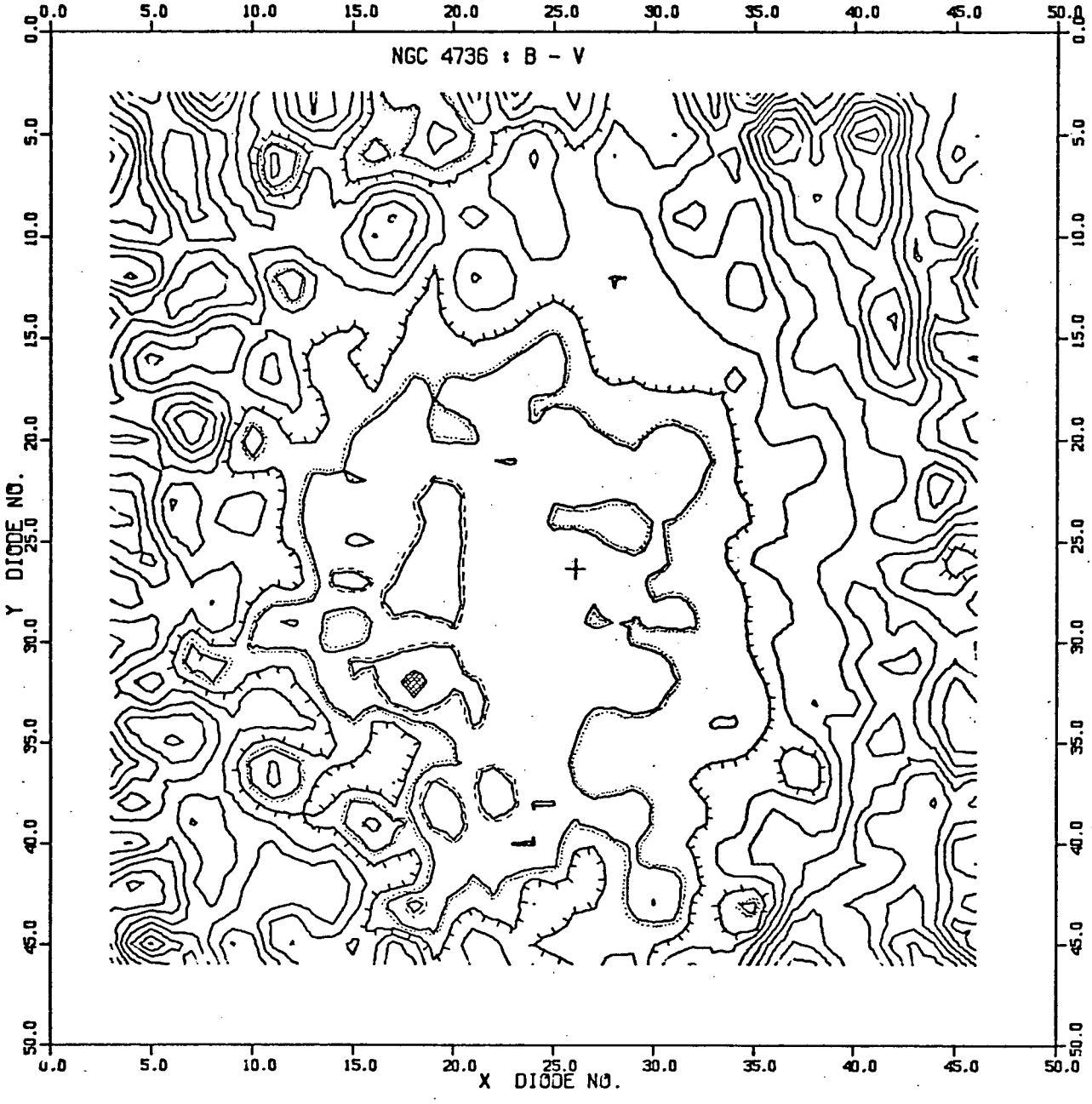

FIGURE 36. NGC 4736: B - V colour map. Instrumental system. Contours separated by 0.05 magnitudes. Highest level (reddest) marked by shading, second highest by broken line on low side of contour, third highest by dotted line, fourth highest by tick marks. Signal to noise ratio lower near edges, highest near nucleus.

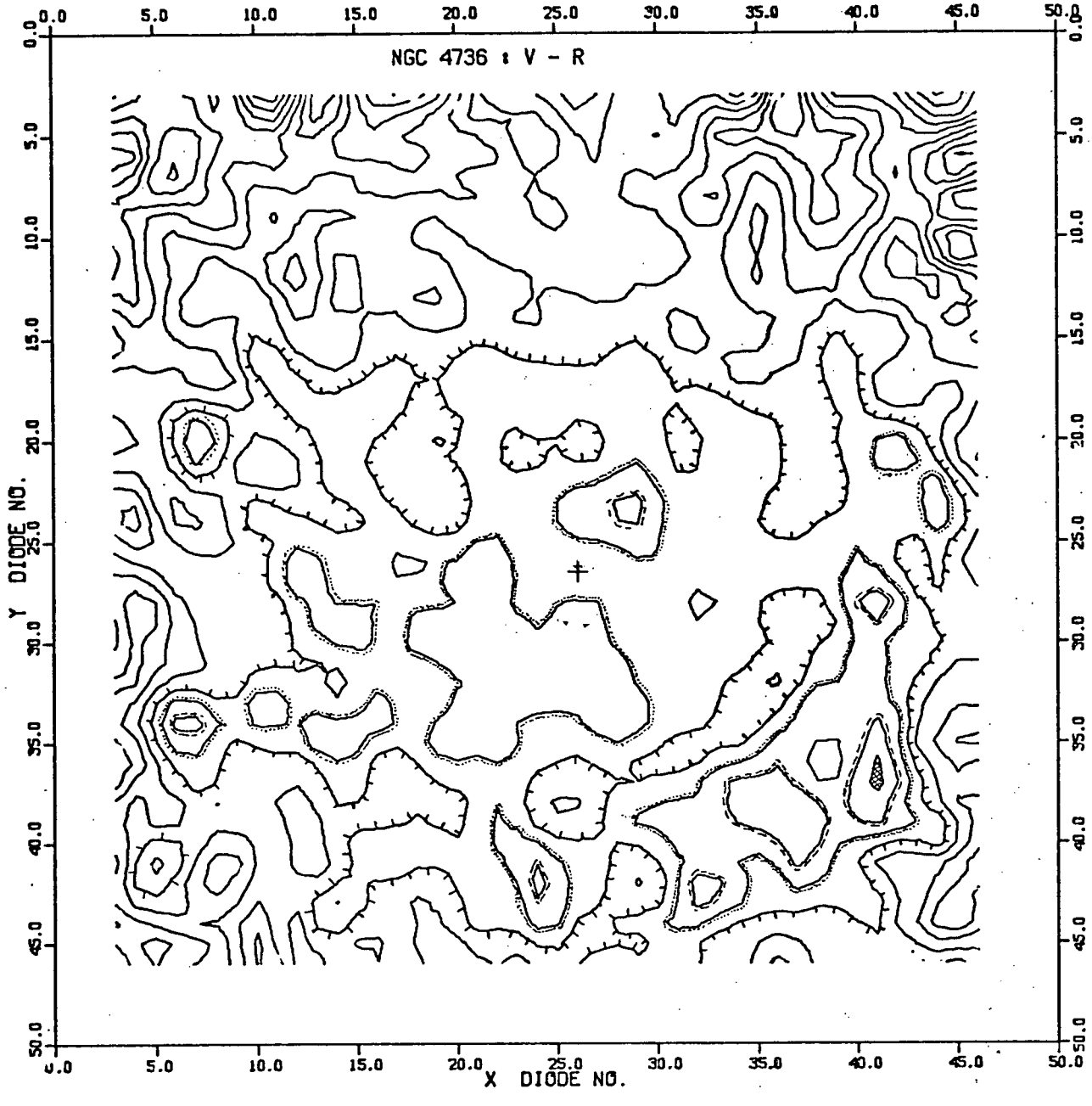

FIGURE 37. NGC 4736: V - R colour map. Instrumental system. Contours separated by 0.05 magnitudes. Highest level (reddest) marked by shading, second highest by broken line on low side of contour, third highest by dotted line, fourth highest by tick marks. Signal to noise ratio lower near edges, highest near nucleus.

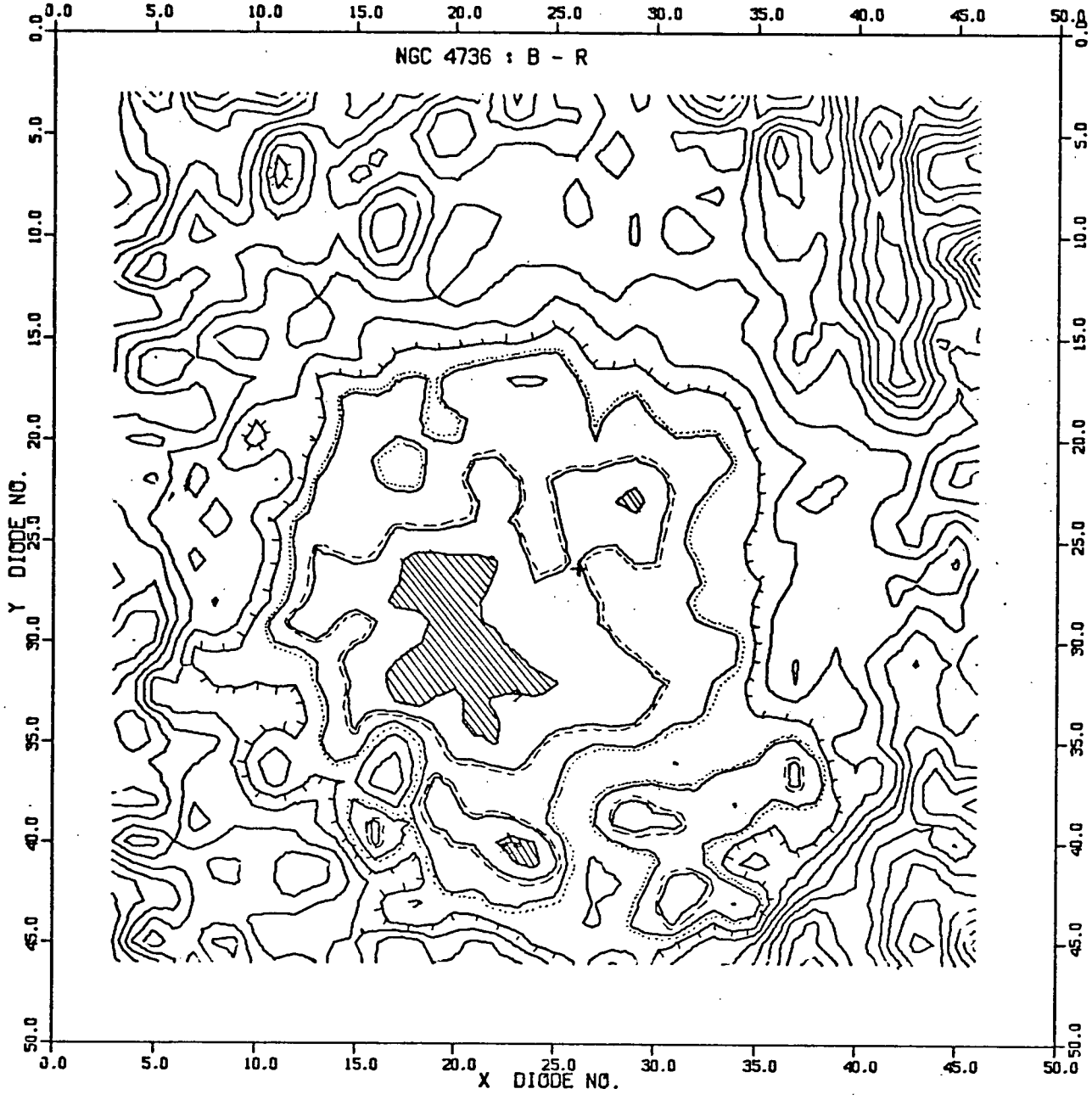

FIGURE 38. NGC 4736: B - R colour map. Instrumental system. Contours separated by 0.05 magnitudes. Highest level (reddest) marked by shading, second highest by broken line on low side of contour, third highest by dotted line, fourth highest by tick marks. Signal to noise ratio lower near edges, highest near nucleus.

TABLE XIV . Nuclear positions for NGC 4736 derived from smoothed images (A= 2.5 diodes). Errors are standard deviations.

Record	Filter	x	y
F13R36	b	25.44±0.02	26.54±0.01
F13R37	v	26.21±0.02	26.26±0.02
F13R40	r	28.58±0.01	29.02±0.01

The most striking features of the colour maps are a strong radial colour gradient at about 10 to 15 arc seconds radius, with a flattening out within that radius, while the nucleus does not stand out at all in the colour map. The negative residual areas are actually the reddest areas, especially the patch in the south-east quadrant. These results will be discussed in the next section.

Simulated line scans computed using the SECTION command in FIRM are presented for two orientations: 30 degrees and 120 degrees true position angle, passing through the nucleus. Figures 39 and 40 show the variation of the residuals and the colours approximately along the "bar" (30 degrees) and perpendicular to it (120 degrees).

4.6 NGC 4736: Simple Models.

The bar-like structure and spiral arm-like features reported here blend smoothly into the features photographed by Chincarini and Walker(1967). Although a complete survey with a larger panoramic detector is obviously required, the results to date allow some interesting ideas to be considered.

I assume that the distribution of matter in a spiral galaxy such as NGC 4736 can be represented by two dynamical components: a spheroidal bulge and a flat, thin disk. I also assume that the density $\rho(r)$ in the bulge component can be represented by equation (43),

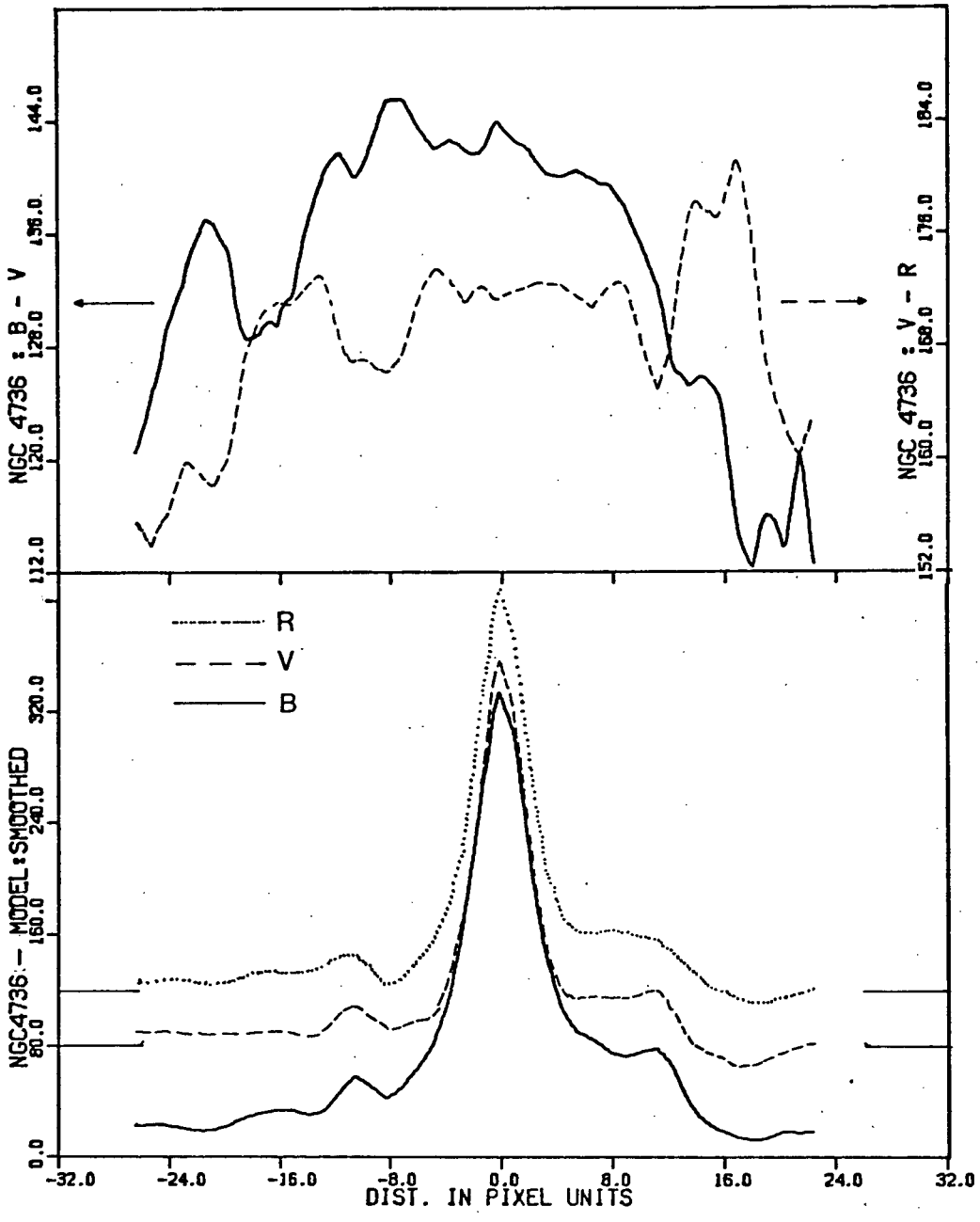

FIGURE 39. Colours and residuals along bar-like structure (true position angle 30°). Residuals scaled by average brightness in each filter before model subtracted. Instrumental colours in hundredths of a magnitude, offset by one magnitude.

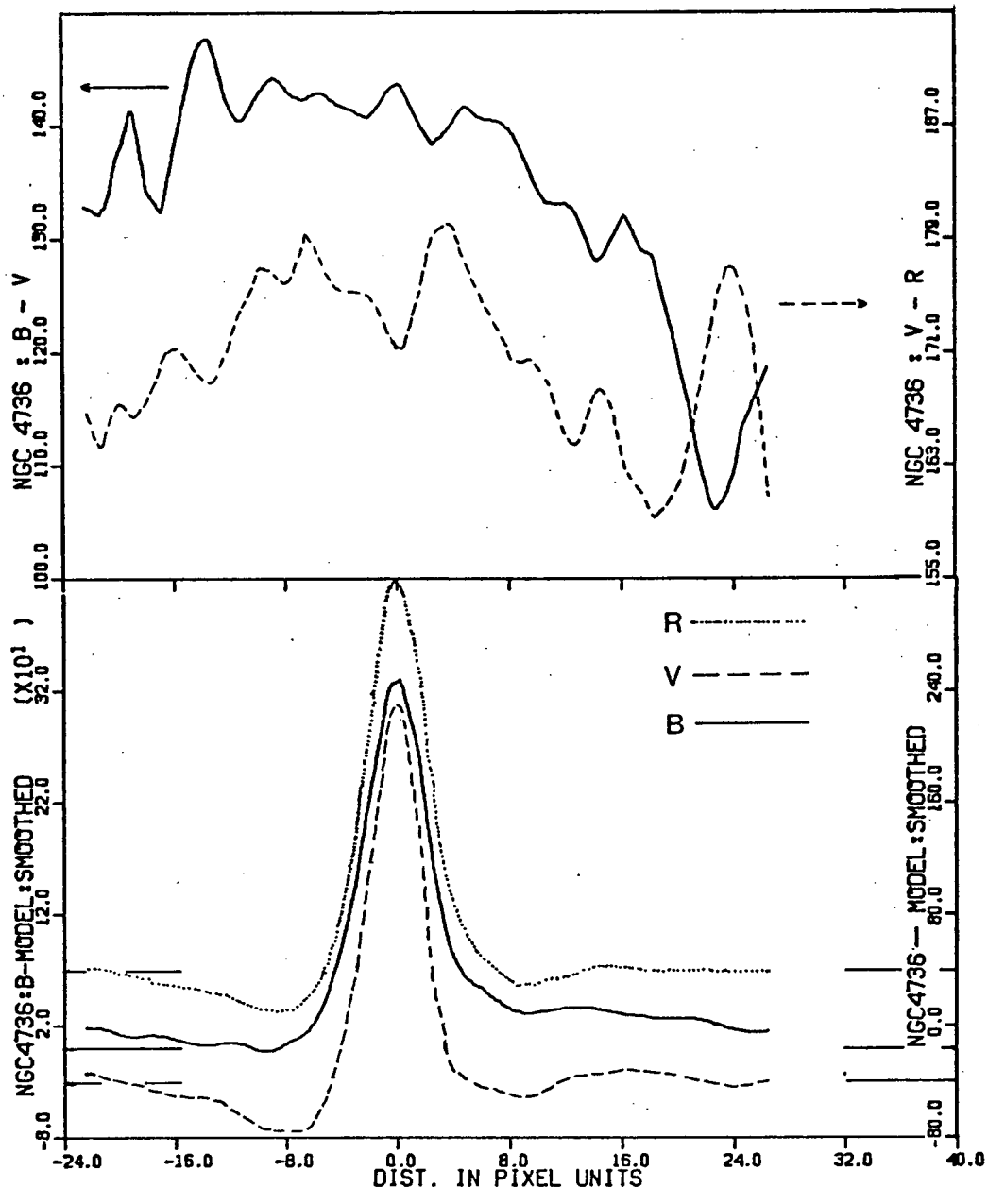

FIGURE 40. Colours and residuals perpendicular to bar-like structure (scan at true position angle 120°). Residuals scaled by average brightness in each filter before model subtracted. Instrumental colours in hundredths of a magnitude, offset by one magnitude.

$$\rho(r) = \frac{\rho(0)}{\left\{1 + \left(\frac{r}{r_c}\right)^2\right\}^{3/2}} , \qquad (53)$$

where r_c is the core radius. The use of this spherically symmetrical distribution has been justified in section 4.3. Perek (1962) describes methods for obtaining force laws from simple analytical <u>spheroidal</u> density distributions. A force law has been derived for the flattened form , but the spherical approximation will be retained here. I assume an exponential distribution of surface density $\mu(r)$ in the disk,

$$\mu(r) = \mu(0) \exp(-\alpha r) , \qquad (54)$$

where $\alpha^{-1} = a_d$ is the disk scale length. The properties of such a disk have been discussed by Freeman (1970). Its existence is supported by photometry (e.g. Schweizer 1976), but it has been seriously questioned by Kormendy (1976), who suggests that the exponential behaviour of surface brightness may be an illusion caused by the superposition of the outer bulge on the optical image. While it may be more accurate to use the de Vaucouleurs surface brightness law and its density distribution together with an exponential disk (e.g. Monnet and Simien, 1977), or to use King's isothermal cluster models with an exponential disk (e.g. Yoshizawa and Wakamatsu, 1975), I use the simpler model expressed by equations 53 and 54. The photometry presented in this chapter suggests that for the innermost regions this simple model may be quite accurate. I neglect the central cusp or nucleus, since its

total contribution, even within a small radius, is quite small.

Starting with first principles, following the clear summary of Yoshizawa and Wakamatsu (1975), the circular orbital velocity (r) can be written as

$$\Theta(r) = \left[r \left\{ F_s(r) + F_d(r) \right\} \right]^{\frac{1}{2}}, \qquad (55)$$

where r is the radius, F_s and F_d are the forces at r due to the spheroidal and disk components respectively. Thus,

$$\Theta^2(r) = \Theta_s^2(r) + \Theta_d^2(r) \qquad (56)$$

where Θ_s and Θ_d are the components of circular orbital velocity due to the spheroid and disk respectively. The spheroidal component has a simple force law,

$$F_s = \frac{G\,\mathcal{M}(r)}{r^2} \qquad (57)$$

Thus, using the density law of equation 53 , we have,

$$\Theta_s^2(r) = 4\pi G \rho(0)\, r_c^2 \left[\frac{\log\left(r/r_c + \sqrt{1+(r/r_c)^2}\right)}{r/r_c} - \frac{1}{\sqrt{1+(r/r_c)^2}} \right] \qquad (58)$$

For the disk component, Freeman (1970) has shown that

$$\Theta_d^2(r) = \pi G\, \mu_d(0) \cdot \frac{r^2}{a_d} \left(I_0 K_0 - I_1 K_1 \right), \qquad (59)$$

where I ,K ,I ,K are modified Bessel functions evaluated at $r/(2a_d)$. Dimensionless squared velocities can be defined,

$$V_s^2\left(\frac{r}{r_c}\right) = \frac{\log\left\{r/r_c + \sqrt{1+(r/r_c)^2}\right\}}{r/r_c} - \frac{1}{\sqrt{1+(r/r_c)^2}}, \tag{60}$$

$$V_d^2\left(\frac{r}{a_d}\right) = \frac{1}{2}\left(\frac{r}{a_d}\right)^2\left[I_0\left(\frac{r}{2a_d}\right)K_0\left(\frac{r}{2a_d}\right) - I_1\left(\frac{r}{2a_d}\right)K_1\left(\frac{r}{2a_d}\right)\right]. \tag{61}$$

Thus,

$$\Theta^2(r) = 4\pi G\rho_s(0)\, r_s^2 \cdot V_s^2\left(\frac{r}{r_c}\right) + 2\pi G\mu_d(0)\, a_d \cdot V_d^2\left(\frac{r}{a_d}\right). \tag{62}$$

This equation can be re-written after defining two constants,

$$\left.\begin{aligned} k_a &= \frac{r_c}{a_d} \\ k_\mu &= \frac{\mu_s(0)}{\mu_s(0)+\mu_d(0)} \end{aligned}\right\}, \tag{63}$$

where,

$$\mu_s(0) = 2\rho_s(0)\, r_c = k_\mu\left(\mu_s(0)+\mu_d(0)\right), \tag{64}$$

and,

$$\mu_d(0) = \left(1-k_\mu\right)\left(\mu_s(0)+\mu_d(0)\right). \tag{65}$$

The parameter k_a is the ratio of scale lengths, and k_μ is the ratio of the projected central spheroid density to the total projected central density.

Thus equation (62) can be written as

$$\Theta^2(r) = 2\pi G a_d \left(\mu_s(0) + \mu_d(0)\right) \cdot \left\{ k_a k_\mu V_s^2\left(\frac{r}{r_c}\right) + (1-k_\mu) V_d^2\left(\frac{r}{a_d}\right)\right\} . \quad (66)$$

The model depends on the two dimensionless parameters k_a , k_μ and the physical scale length r_c or a_d . This is in agreement with the idea that there are two fundamental galactic parameters, one of which is scaled by a physical dimension (Roberts, Roberts and Shu 1975). The definitions used here are similar to those of Yoshizawa and Wakamatsu (1975) and Monnet and Simien (1977), except that these authors use the de Vaucouleurs effective radius rather than the King core radius. Since the simple bulge model given by equation 53 does not have a finite mass when integrated to infinite radius, total mass concepts are not used here. (the exponential disk, of course, has a finite mass, $\mathcal{M}_d = 2\pi\mu_d(0)a_d^2$). This leaves open the possibility of a massive outer spheroidal halo , which does not affect the inner rotation curve. On the other hand, a non-exponential disk in the outer regions could affect dynamics closer to the centre, a point well made by Mestel (1963) and often not understood.

If it is assumed that the mass to luminosity ratios of the bulge and of the disk do not change with radius, photo-

metry can give the mass distribution. On the other hand, if it is assumed that the rotation curve obtained from radial velocity measurements represents the true circular orbital velocities in the system the mass distribution can be inferred from the rotation curve, the photometric and dynamical results can then be compared.

There is no published photometry of NGC 4736 which extends out well into the disk, and only the inner bulge has been observed using the RETICON camera. To obtain a "photometric" model, I use the observations reported here to determine the core radius (section 4.4), and adjust the density ratio k_μ and the disk scale length a_d to reproduce the <u>outer</u> HI rotation curve published by Schommer and Sullivan (1976). I then compare the theoretical <u>inner</u> rotation curved derived from this model with the rotation curves of Chincarini and Walker (1967) and van der Kruit (1976). Since a_d is at present unknown but may be available from new observations currently being reduced by other workers (Schommer and Sullivan 1976, van der Kruit 1976), the model derived here is only an approximate one, and a detailed least squares fit is not attempted. Similarly the outer bulge is not well observed, although there is published line scan photometry by Simkin (1967). The inner results are extrapolated outwards in the present work.

Firstly, a model was constructed using the photometrically-derived bulge core radius $r_c = 6''.0 \pm 0''.5$. The

fitting procedure was by eye, which was quite sensitive in this case since the shape of the rotation curve for an Sb galaxy varies strongly with respect to the bulge to disk scale length ratio and the density ratio (see, for example, Yoshizawa and Wakamatsu 1975, and Roberts and Rots 1973).

Secondly, a model was constructed by fitting to the entire rotation curve. The dynamically-derived core radius, assuming that the density law of equation 53 is a good approximation, is about 8 seconds of arc. Models for r_c = 6, 8 and 10 arc seconds are shown in Figures 41, 42 and 43, at three different scales. The observational points of the rotation curve are taken from the graphs of Schommer and Sullivan (1976) and van der Kruit (1976), based on the observations of these authors and those of Chincarini and Walker (1967) and Bosma, van der Hulst and Sullivan (1977).

For the model with r_c=6", a reasonable fit is obtained at radii larger than 12", but the inner rotation curve is not as well predicted. Either the observed inner rotation curve does not represent the true circular orbital velocity, or the mass to luminosity ratio varies in the inner regions of NGC 4736. The model for r_c =8" gives a closer fit at small r and is quite good at all radii. The model for r_c =10" fits well at small radii but has a negative slope for r=40", whereas the radio observations show a negative slope beginning at r=240". It is interesting that the theoretical rotation curves are higher than the observations around 300" radius. The

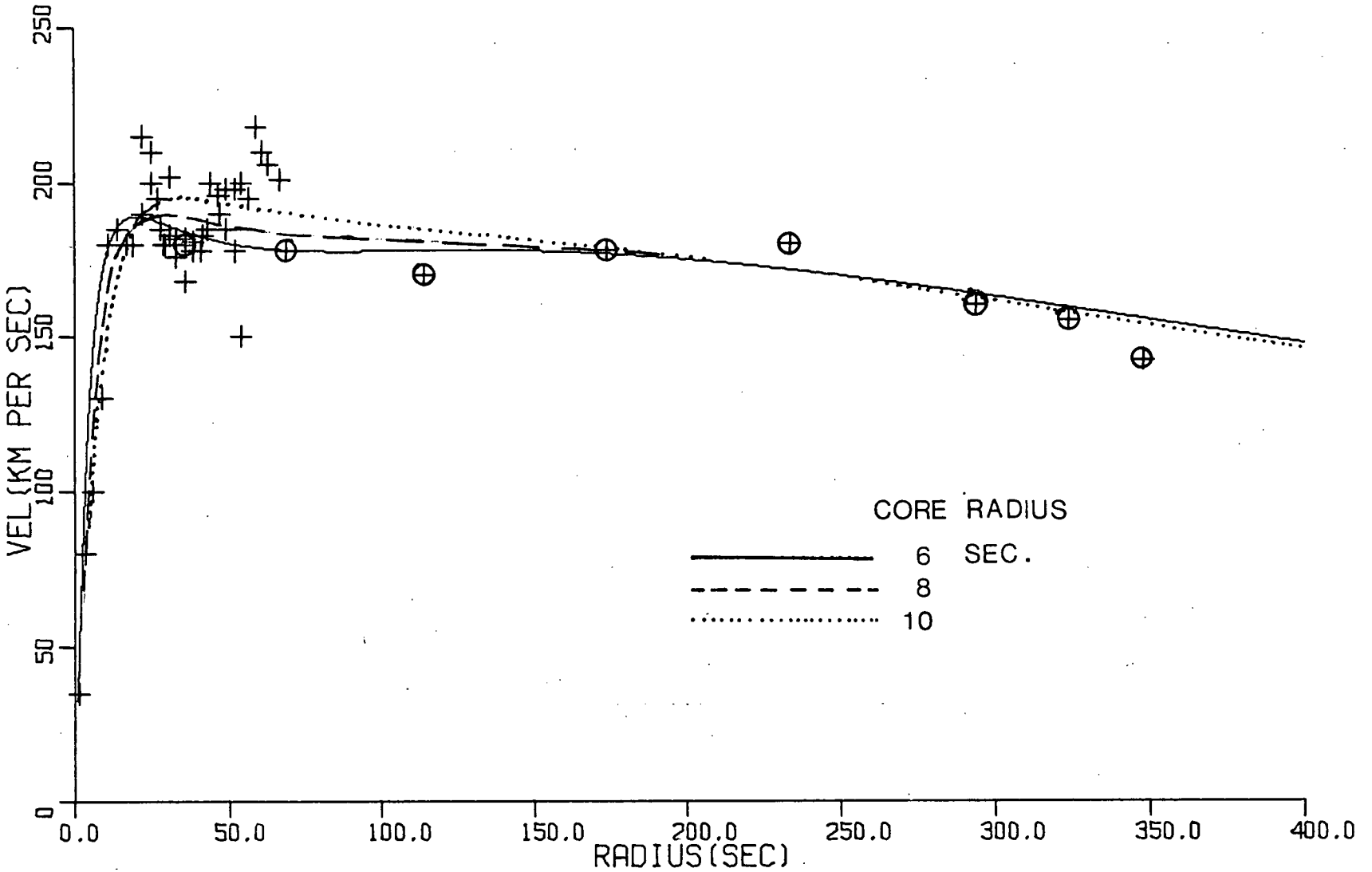

FIGURE 41. NGC 4736: Full rotation curve and models. Circled points are HI measurements, from graphs of Schommer and Sullivan (1976) and van der Kruit (1976).

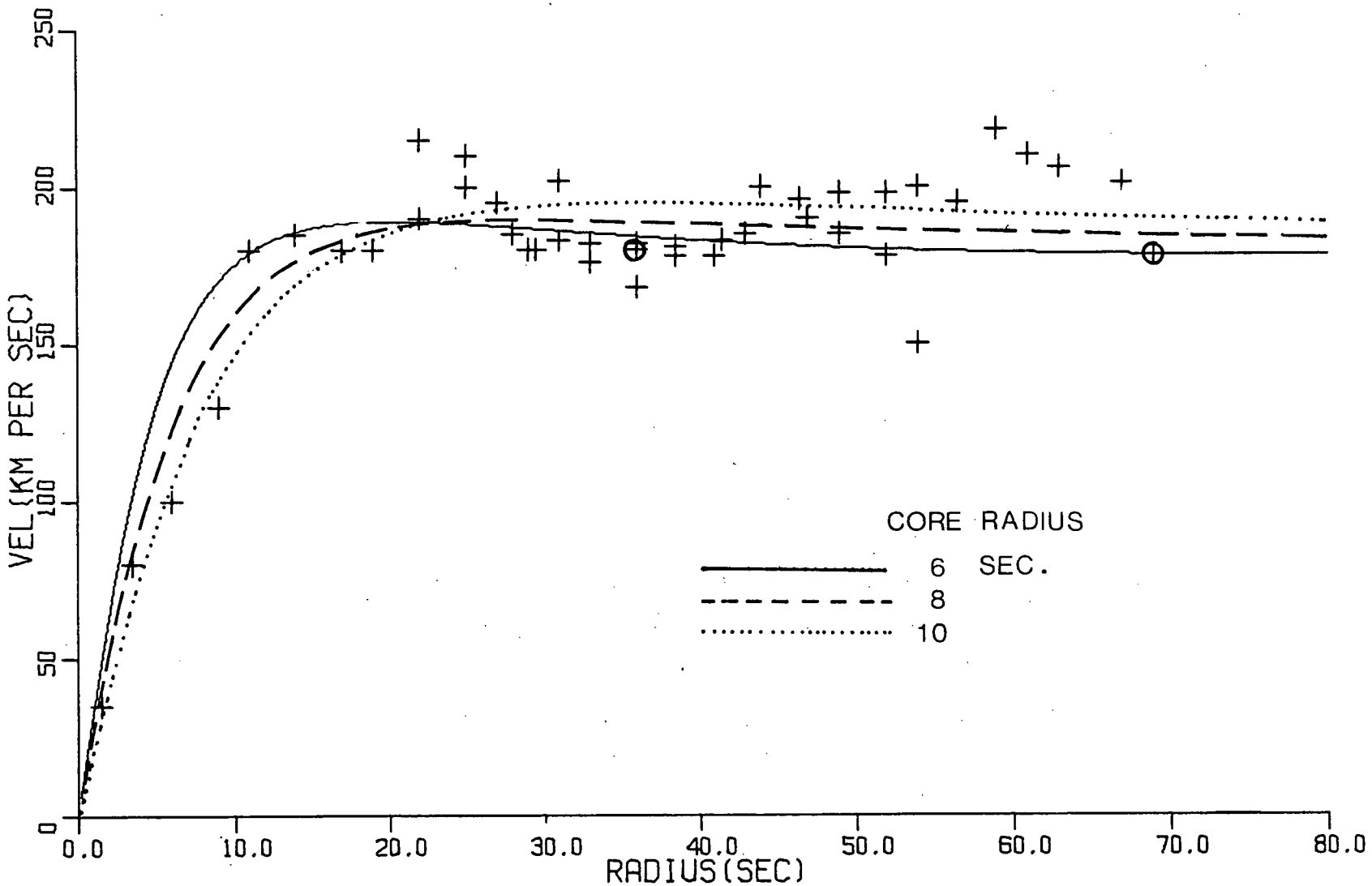

FIGURE 42. NGC 4736: Rotation curve and models to 80". Circled points are HI measurements, from graphs of Schommer and Sullivan (1976) and van der Kruit (1976).

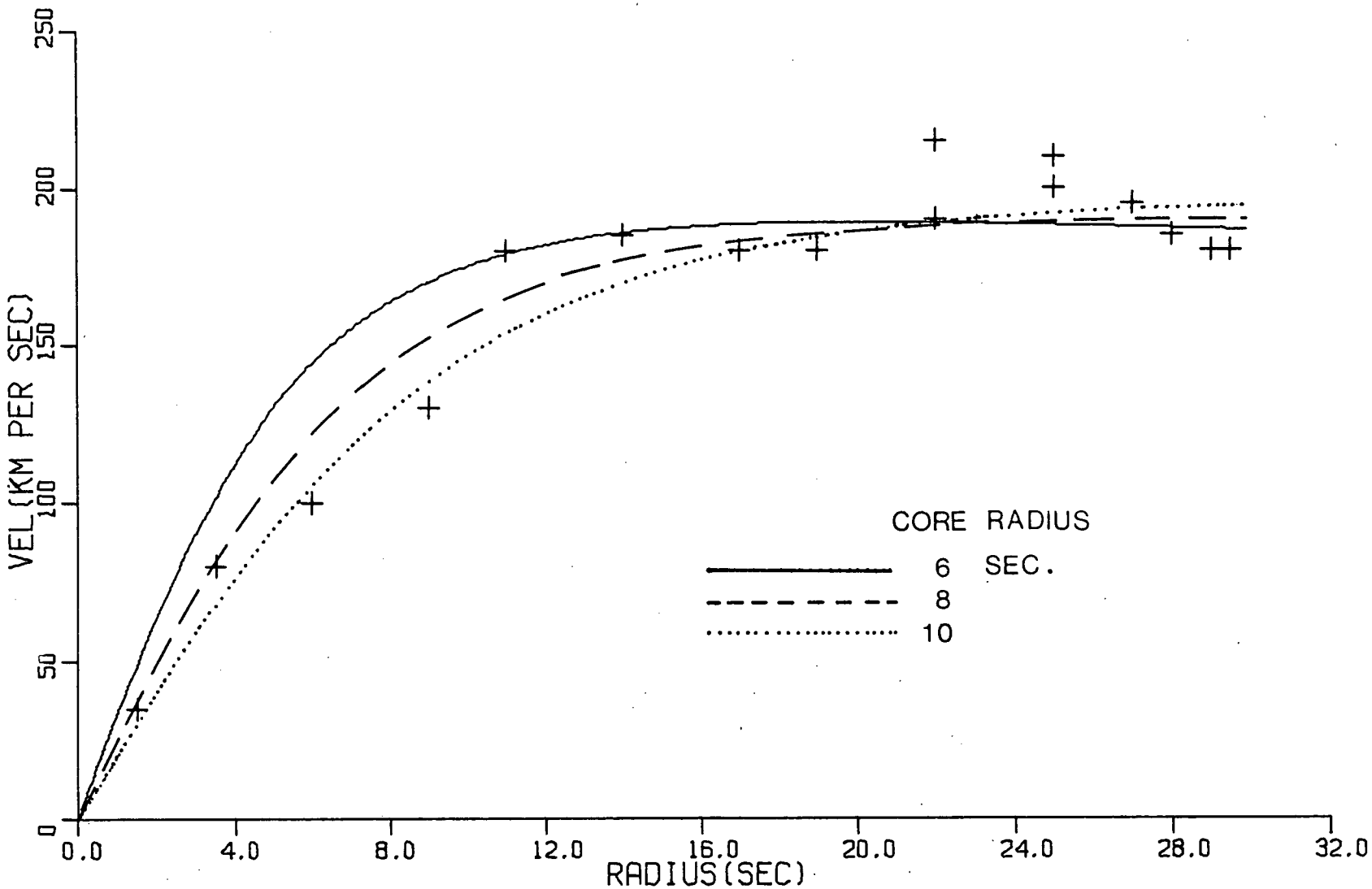

FIGURE 43. NGC 4736: Rotation curve and models to 32". Spectrographic measurements as plotted by van der Kruit (1976).

parameters of all three models are listed are listed in Table XV . The bulge to total mass ratios should not be taken too seriously, since the model has been enormously extrapolated. The value of the disk scale length a_d is uncertain since it has been inferred using the model and not measured directly.

Bearing in mind the difficulty of measuring the true circular rotation curve close to the nucleus, and that the HI observations are more accurate than the emission-line measurements (Schommer and Sullivan 1976), the model with r_c = 6" is acceptable, although r_c = 8" gives a better fit for distances less than 10" from the nucleus. Given the simplicity of the spherical bulge and exponential disk model used here, the consistency between the photometric surface brightness distribution and the rotation curve is reasonably good.

Mass to luminosity ratios were computed using the models in Table XV and the photmetry of Chincarini and Walker (1967). The integral of the surface brightness law of equation (42) is given by,

$$L(R) = I(0)\pi r_c^2 \ln\left(1 + R^2/r_c^2\right), \qquad (67)$$

where L(R) is the luminosity enclosed within an aperture of radius R. Assuming that the disk contribution to the central luminosity and projected density is negligible, the central surface brightness I(0) can be found given L(R), R and r_c . From this, the central mass to blue luminosity ratio M/L_B is

TABLE XV . Parameters for models of NGC 4736.

Parameter Model =	I	II	III
Core radius r_c (arcsec)	6.0	8.0	10.0
Central projected density ratio k_μ.	0.975	0.97	0.97
Disk scale length a_d (arcsec)	100	100	100
Central surface density $\mu(0)$ ($M_\odot pc^{-2}$)	2.48×10^4	1.83×10^4	1.53×10^4
Central disk density $\mu_d(0)$ ($M_\odot pc^{-2}$)	6.19×10^2	5.50×10^2	4.60×10^2
Central bulge density $\rho_s(0)$ ($M_\odot pc^{-3}$)	67.0	37.0	24.8
Mass inside 10Kpc $\mathcal{M}_{10}$ ($M_\odot$)	4.8×10^{10}	4.8×10^{10}	4.9×10^{10}
Mass inside 25Kpc $\mathcal{M}_{25}$ ($M_\odot$) (*)	5.8×10^{10}	5.9×10^{10}	6.1×10^{10}
Total disk mass $\mathcal{M}_d$ ($M_\odot$)	3.5×10^{10}	3.1×10^{10}	3.6×10^{10}
Bulge mass /Total mass (inside 10 Kpc)	0.38	0.46	0.55
Bulge mass / Total mass (inside 25 Kpc) (*)	0.39	0.48	0.57

(*) : Extrapolation of density model.

given by,

$$M/L_B = \mu(0)/I_B(0) \quad , \tag{68}$$

where (0) is the projected central surface density. Mass to luminosity ratios obtained using equations (67) and 68) with models I, II and III are presented in Table XVI . The slightly lower ratio for Model I with the smallest aperture (ccmpared with the value derived from the larger apertures) shows the effect of the nuclear "cusp". The "semi-stellar" nucleus contributes about 10% of the light through the smallest aperture used by Chincarini and Walker (1967).

Bosma, van der Hulst and Sullivan (1977) find a total mass of 5.3×10^{10} M within a radius of 9.6kpc, and a total mass to luminosity ratio $M/L_B = 2.5$. The dynamical model of Nordsieck (1973) was used. The total mass to luminosity ratio is very similar to the nuclear mass to luminosity ratio found in this work. This would suggest that the bulk of the light in the galaxy comes from a population with a mass to luminosity ratio which is roughly the same throughout the galaxy.

TABLE XVI . Mass to blue luminosity ratios using models from Table XV and photometry of Chincarini and Walker (1967). Units are M(sun)/L_B(sun).

Aperture radius	Model I	II	III
5.5"	3.3	2.7	2.4
8.5"	3.6	3.2	2.9
14.0"	3.6	3.5	3.5

4.7 NGC 4736: Spiral Patterns And Resonance Phenomena.

The radii of features described in section 4.1 are listed in Table XVII . Some of these features have been identified by various authors as evidence of Lindblad resonances (e.g. Lindblad 1974, Schommer and Sullivan 1976). In particular, the features around 60 arc seconds radius are thought to be associated with an inner Lindblad resonance at $R=R_{inner}$ where

$$\Omega(R) - \frac{\kappa(R)}{2} = \Omega_p \tag{69}$$

The angular velocity of the stars in circular orbits is $\Omega(R)$ while the angular velocity of the two-armed spiral pattern is Ω_p . The quantity κ is the epicyclic frequency, which is the rate at which a perturbed star will oscillate about its mean circular orbital path (see Wielen 1974 for a lucid review).

The epicyclic frequency κ is given by

$$\kappa^2 = 4\Omega^2\left(1 + \frac{R}{2\Omega}\frac{d\Omega}{dR}\right), \tag{70}$$

and is calculated by simple numerical differentiation.

The outer edge of the main visible disk is also the inner boundary of the low-luminosity "gap". It is thought to be near the corotation radius R_c , at which,

TABLE XVII . Radii of Visible and Radio Features Adopted for NGC 4736.

Feature	Radius	Source
Outer edge of central "intense region".	16"	(1)
Ends of small "bar".	17"	*This Work
Inner edge of observable HII emission.	37"	(2)
Outer edge of bright radio continuum inner disk.	50"	(4)
Peak of HI surface density.	40-60"	(3)
outer edge of HII emission ring.	58"	(2)
Outer edge of optical "second zone".	60"	(1)
Outer edge of main visible disk ("third zone").	200"	(1)
Inner edge of outer visible ring.	260"	(1)
Outermost published HI radial velocity.	360"	(3)

* Corrected for inclination i=35°.
1. Sandage (1961).
2. van der Kruit (1976).
3. Bosma *et al.* (1977)
4. de Bruyn (1977).

$$\Omega(R_c) = \Omega_p \quad . \tag{71}$$

Spiral structure is not seen outside this radius, but there is a faint outer ring (Sandage 1961). The outer Lindblad resonance is thought to be in or beyond this outer ring (Schommer and Sullivan, 1976).

At the outer Lindblad resonance radius $R=R_{outer}$, we have

$$\Omega(R) + \frac{\kappa(R)}{2} = \Omega_p \tag{72}$$

It has been shown by Barbanis (1970) that density-wave spiral arms should not propagate beyond the co-rotation radius. Contopoulos (1974) has demonstrated that only a bar may exist inside the inner Lindblad resonance radius. In NGC 4736, spiral arms indeed are not seen outside the assumed corotation radius of about 200", but there is a spiral pattern defined by dust lanes within the inner 60" ring (Chincarini and Walker 1967). The present work discloses a bar-like inner structure extending to a de-projected radius of 17" (assuming that the bar-like structure lies in the plane of the disk).

Adopting R = 200", the Lindblad resonances have been computed for Models I, II and III, and are listed in Table XVIII . The angular velocities Ω , $\Omega - \kappa/2$ and $\Omega + \kappa/2$ are shown in Figure 44. A spiral pattern angular speed of 29 km s^{-1} kpc^{-1} is found for R_c = 200", using a scale of 30

TABLE XVIII . Main Disk Model Resonance Parameters.

Parameter	Model = I	II	III	SS
Pattern Speed ($km\ s^{-1}\ kpc^{-1}$).	29±1*	29	29	33
Inner Lindblad Resonance (arcsec).	62	64	68	66
Corotation Radius (arcsec).	200**	200	200	210
Outer Lindblad Resonance (arcsec).	300	299	296	270**

* : Corresponds to V_{rot} = 175±5 km s^{-1}.

** : Adopted.

SS : Model of Schommer and Sullivan (1976).

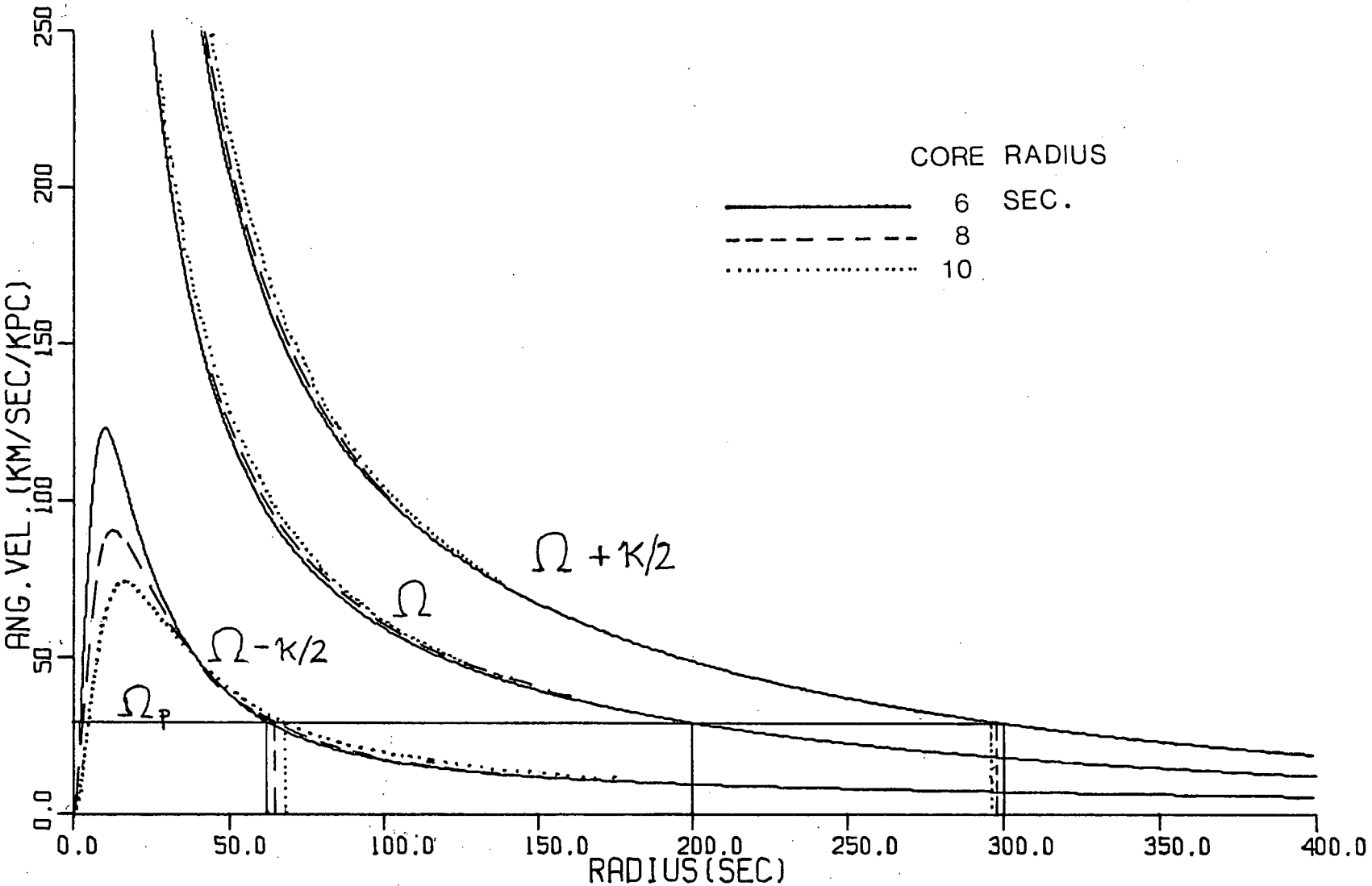

FIGURE 44. Model angular velocities for NGC 4736. Pattern velocity for model with r =6" shown.

parsecs per arc second. For each model , the inner Lindblad resonance is well defined and lies between 60 and 70 arc seconds.

Also listed in Table XVIII is the empirical model of Schommer and Sullivan (1976). Their resonance radii were derived from the epicyclic frequency which they computed directly by applying equation 70 to a polynomial fitted to the rotation curve observations. Agreement with the present work is good.

A Two-Spiral Model.

How can the spiral dust pattern and the small bar inside the inner Lindblad resonance be explained? I shall propose a model which involves a separate spiral pattern inside the inner Lindblad resonance of the main spiral of NGC 4736. This inner spiral has a higher angular speed than the main spiral.

In addition to NGC 4736, several other galaxies have distinct inner patterns. The barred spiral NGC 4314 (SBa(s)pec) has a very distinct little two-armed spiral well inside its main bar (Sandage 1961, Matsuda and Nelson 1977). The early barred systems NGC 1291 and 1236, classified by de Vaucouleurs as (R)SB(s)0/a, have small bars inside their main bars (de Vaucouleurs 1974). The existence of inner patterns or sub-structures may be a fairly common phenomenon. If these inner sub-structures are to obey the same rules as are thought to govern the principal spiral structure, their pattern speeds

must be higher than or equal to the local value of $\Omega - \kappa/2$.

I assume that a non-axisymmetric disturbance of the gravitational potential in the central bulge gives rise to a spiral pattern which is probably a gaseous spiral rather than a true stellar density wave. Of course, the idea of central bars generating the spiral patterns in SA galaxies is not new (e.g. Lindblad 1956, 1959, 1974; Holmberg 1958; Simkin 1970; Marochnik and Suchkov 1974), but it is only recently that hydrodynamical calculations have been carried out using a realistic mass model. Sanders and Huntley (1976) have shown that a slight oval deformation of the gravitational potential in a galaxy can generate trailing gas spiral waves. Sorensen, Matsuda and Fujimoto (1976) have demonstrated a similar effect for a bar-like, rapidly-rotating strong gravitational deformation. Shock waves and non-circular gas motions are predicted by both models. An attempt to explain the principal large-scale spiral system in galaxies has met with limited success (Matsuda and Nelson 1977).

However, I now assume that a rapidly rotating central deformation could possibly lead to a corresponding small spiral pattern in the disk inside the inner Lindblad resonance of the main spiral system. It is beyond the scope of this work to carry out a full hydrodynamical calculation to test this hypothesis, but a check on its consistency can be obtained from area photmetry and the mass model.

Assuming that the ends of the small central "bar" correspond to the inner resonance of the inner spiral, the parameters listed in Table XIX are obtained. The corresponding angular velocity diagram is shown in Figure 45.

4.8 NGC 4736: Discussion.

The model adopted in the previous section involves two spiral patterns, one inside the other, rotating at different angular speeds. The two spirals each have their own particle resonances, which are deduced by combining a model for the mass distribution with some assumptions derived from optical images.

It can be seen from Figure 45 that adopting a different inner Lindblad resonance radius for the inner spiral will not greatly change the conclusions. The mass model with r = 6" gives a more consistent set of resonance radii for both the main spiral system and for the postulated inner system. This is especially true for the phenomena around 60" radius, the position of which has been left as a free parameter to be determined from the models themselves.

The inner spiral which starts at the ends of the small bar has corotation near the inner Lindblad resonance radius of the main spiral system. The bar-driven gas spiral models of Sanders and Huntley (1976) and Sorensen, Matsuda and Fujimoto (1976) have spiral arms extending beyond the corotation radius

TABLE XIX . Inner Disk Model Resonance Parameters.

Parameter	Model = I	II	III	
Pattern speed ($km\ s^{-1}\ kpc^{-1}$).	102	87	74	
Inner Lindblad Resonance (arcsec).	17	17	17	(*)
Corotation radius (arcsec).	58	70	84	
Outer Lindblad Resonance (arcsec).	99	117	123	

* : Adopted from area photometry, corrected for inclination $i=35^{o}$.

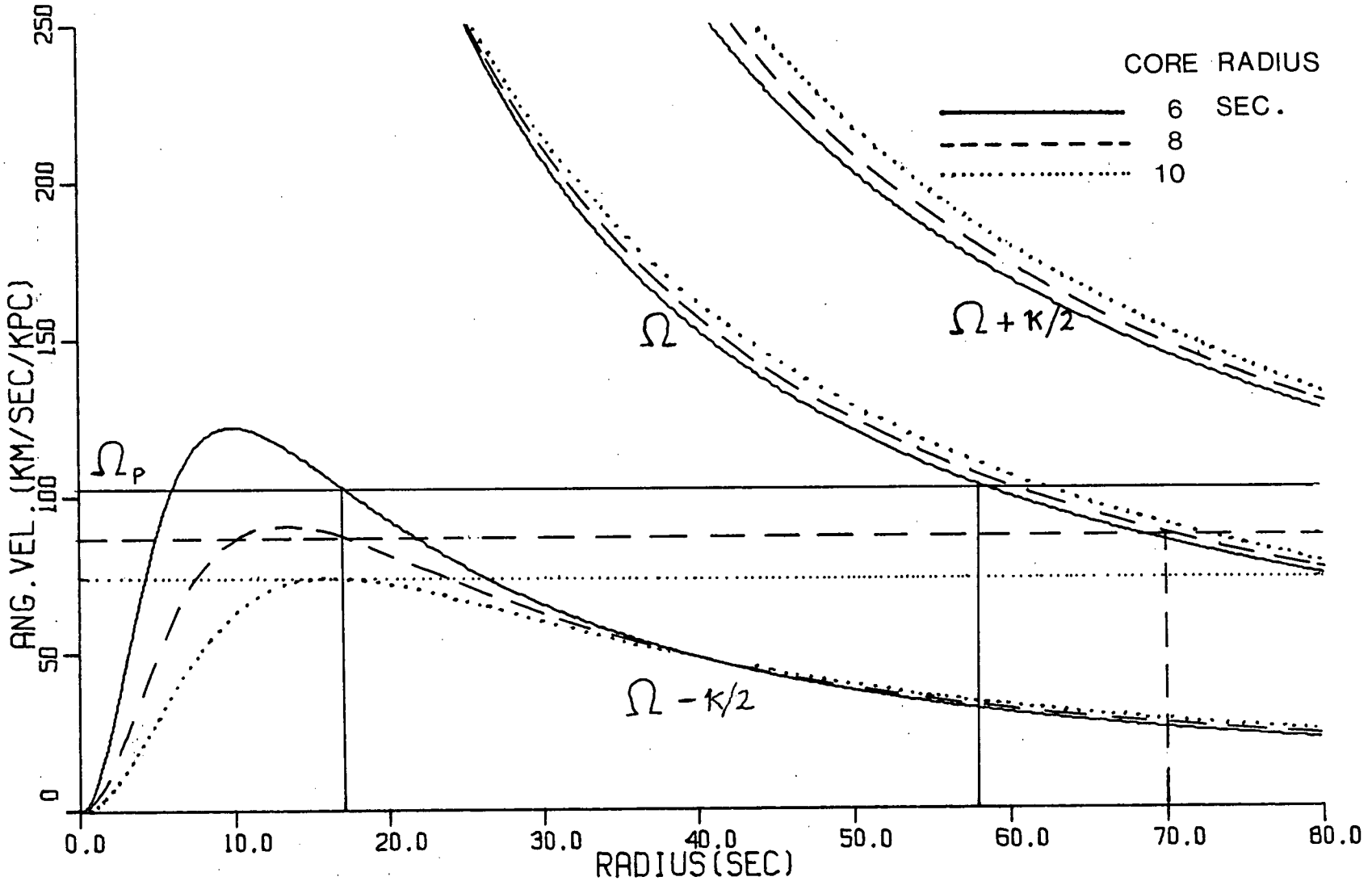

FIGURE 45. Inner model angular velocities for NGC 4736. Model pattern speeds shown.

to the outer Lindblad resonance of the model. If such a model is true for the inner spiral system, the inner system's outer parts would lie in the main system itself. There is little published data on the structure of the spiral arms in the main disk. It is known that the main spiral system appears to be very broken and tightly wound (Sandage 1961; van der Kruit 1974). Schommer and Sullivan (1976) refer to unpublished surface photometry revealing a faint but distinct two-armed spiral in the main disk. The broken structure of the spiral in the main disk may be partly due to interference between the inner gas spiral and the main spiral. The main spiral presumably is evidence of a stellar density wave.

According to the two spiral model, the diffuse H emission and enhanced star formation is caused by the shocks experienced by gas moving in a disk within the bulge of NGC 4736. The very high surface brightness and rather low mass to luminosity ratio in the central regions would also be caused by this spiral activity. The radio continuum emission studied by van der Kruit (1971) and de Bruyn (1977), and the somewhat anomalous gas velocities obtained by van der Kruit (1974, 1976) can qualitatively be associated with the inner spiral, especially as there may be complex interactions between the two spiral systems at about 60 arc seconds radius.

It is very difficult at present to decide whether the small central "bar" is really a bar composed of stars or whether it is the portion of the inner spiral which lies

inside its inner Lindblad resonance. The presence of dust complicates the interpretation of optical images. Thus one cannot at present decide whether the inner spiral pattern is caused by a strong bar-like perturbation or by a slight oval non-axisymmetry of the bulge mass distribution. Is the observed "bar" the cause or an effect of the inner spiral system?

Some N-body calculations have demonstrated the formation of bars in the central regions of galaxies (Miller 1972, Hohl 1972, Quirk 1972). These results are interpreted by Contopoulos (1971) to mean that the short bars at the centre do not produce spirals themselves, but evolve due to instabilities. Ostriker and Peebles (1973) find that a massive halo is needed to prevent such instabilities, and in the case of NGC 4736 the central disk is indeed inside a massive bulge. Table XV shows that the bulge contains between 38% and 57% of the total mass, with about 45% being the most likely figure. As noted before, these figures are not well determined. Hohl (1976) showed that a centrally concentrated core-halo system (i.e. "bulge") must contain 60% or more of the total mass in order to stabilize the disk against the formation of a bar, while a uniform density halo need only contain 40% of the total mass. Thus NGC 4736 does not appear to satisfy the Ostriker-Peebles stability criterion, although the disk-to-bulge ratio is close enough to suggest a marginal case. The paradox of stable disks in galaxies with an

apparently small bulge has led to the suggestion of massive outer halos in spiral galaxies. Since the rotation curve of NGC 4736 appears to have a distinct "turnover", with a decrease of circular velocity at large radii, it is less likely that there exists an extensive outer halo of the type postulated by Ostriker, Peebles and Yahil (1974). Is a central bar-like or oval distortion caused by the bar instability, or is it caused by the more subtle spiral resonance effects considered by, among others, Contopoulos (1970, 1975), and Mertzanides (1976) ? The bar-like or oval distortion is probably not due to the "disk-heating effect" as discussed by Ostriker and Peebles, but rather may be caused by the more subtle spiral resonance effects considered by Contopoulos (1970, 1975).

The semi-stellar nucleus may itself be caused by the non-axisymmetry of the central bulge. Matsuda and Nelson (1977) have suggested that shocks experienced by gas moving through galactic bars may lead to the loss of angular momentum by the gas and its eventual infall into the nucleus. However, the globular cluster accretion model of Tremaine, Ostriker and Spitzer (1975) provides another attractive explanation for the formation of galactic nuclei.

Implications of the Model.

Inner spirals and bars may exist in galaxies other than those mentioned in section 4.7. Holmberg (1958) has suggested that all spiral galaxies contain a bar-like distortion in

their central regions. When the inner Lindblad resonance for the main spiral pattern is at a large radius, an inner pattern could exist. Several of the galaxies studied by Roberts, Roberts and Shu (1975) have main pattern inner resonances at radii greater that 2 kiloparsecs, e.g. M31, M81 and our own galaxy. High central mass concentration (hence early Hubble type) and low pattern speeds lead to large resonance radii. The galaxy NGC 4736 is quite similar to M31 and to our own galaxy, with similar structure and similar rotation curve, and it is possible that inner bar-like distortions also exist in the latter two galaxies. There is a variation with respect to radius of ellipticity and position angle for the isophotes of M31 (Peterson, Ford and Rubin 1977), and faint dust spiral structure is observed to within 6" of the nucleus (Johnson and Hanna 1972). Anomalous gas motions exist in the central bulge (Rubin and Ford 1971). Similar phenomena have been found in M81 (Goad 1976). Peculiar velocities in the central regions of our own galaxy have been known for a long time, and a bar has been suggested as the cause (Johnson 1957, Lindblad 1959, Cohen and Davies 1976).

Matsuda and Nelson (1977) have suggested that an inner bar could provide the driving force for the main spiral system in our galaxy. However, such a bar would have to rotate at the same angular speed as the main pattern. Roberts, Roberts and Shu (1975) found a pattern speed Ω_p of 13.5 Km s^{-1} Kpc^{-1} for the Galaxy, whereas the strong perturbation model of

Sorensen, Matsuda and Fujimoto (1976) requires a much higher pattern speed. Matsuda and Nelson (1977) do, however, propose the alternative idea that the inner bar does not co-rotate with the main spiral pattern. The high non-circular velocities found inside 3 kpc by Cohen and Davies (1976) suggest that a rapidly rotating pattern or density perturbation exists in the centre of our galaxy.

4.9 NGC 4736: Conclusions

The disclosure of a bar-like central structure and the construction of dynamical models from area photometry strongly suggest that a double spiral pattern exists in NGC 4736. This model can qualitatively be associated with the emission and the slightly anomalous velocities observed in this galaxy. The explosion models of van der Kruit (1974) and Sanders and Bania (1976) are therefore not as necessary to explain these anomalies. Similar conclusions may apply to other galaxies such as M31, M81 and our own galaxy.

CHAPTER 5

THE GLOBULAR CLUSTER NGC 7078

5.1 Background

The bright, high-latitude globular cluster NGC 7078(=M15) is notable because its centre lies within one arc minute of an X-ray source (Giacconi et al. 1974; Clark, Markert and Li 1975), and because it has an unusual central excess, or "cusp", of surface brightness (King 1975). Stars have been counted directly to within 0.45 arc minutes radius of the centre by King et al. (1968) and to within 0.12 arc minutes by Bahcall, Bahcall and Weistrop(1975). Leroy, Aurier and Laques (1976) have taken a series of standard and electronographic plates in exceptionally good seeing (0.7"), and within a field of 25" x 25" they have measured the positions and V magnitudes of 120 stars down to V=18, which contribute 30 percent of the total light in that field. They find a distinct unresolved concentration at the centre with a radius of about 2".

Integrated aperture photometry has been published for apertures of 0.093 to 0.905 arc minutes radius (King 1966b). Integrated surface brightness profiles have been obtained from electronographic plates by Kron and Papiashvili(1967) and by Newell, da Costa and Norris (1976). The latter group has also obtained UBV integrated colours (Newell, private communi-

cation), showing that the cusp is not significantly bluer than the unresolved population of the cluster.

High-resolution blue and red plates of the nuclear region are being reduced by Feibelman(1977), who suggests a high central concentration of red giants. Illingworth and King(1977) have proposed that a central "black hole" is not needed, and that a modest number of 1.5 to 2.0 solar mass objects (such as old neutron stars) would be sufficient to produce the observed central cusp. These objects are more massive than the probable present red giant mass of 0.8 solar masses, and would long ago have migrated to the centre of the cluster (Spitzer 1969).

Hills and Day(1976) have calculated that NGC 7078 may have experienced about 1500 collisions between its main sequence stars, one of the highest such numbers for their sample of globular clusters (the median value is 92 collisions per cluster). NGC 7078 has a fairly short relaxation time of about 10^8 years , and a high escape velocity of about 40 km s^{-1} (Peterson and King 1975).

In the light of ideas discussed in the first chapter regarding the possibility of unusual phenomena in the cores of "X-ray" globular clusters, the central region of NGC 7078 was observed using the RETICON area photometer mounted at the Cassegrain focus of the 1.8 metre telescope of the Dominion Astrophysical Observatory.

5.2 NGC 7078: The Observations

The observations listed in Table XX were taken on two unusually good nights at Victoria, sharing time with A.Condal. Since little time was available for my observations, and because photometric conditions and good seeing are rare at Victoria, the observations were made in a differential mode, in the same fashion as the observations at Mauna Kea. The second night (1976 September 16) was definitely superior, and only the observations from the second night were analysed in detail.

Since the exposures were of different durations, care had to be taken with subtraction of the dark current. The average dark current was about 0.3 instrumental units per diode per minute, but a few diodes, about 3 percent, had dark currents of between 0.6 and 5.2 units per diode per minute. Summing over a selection of these "hot" diodes showed that up to the half-hour exposure time used here the dark current was very accurately a linear function of the exposure time. A composite dark current corresponding to an effective integration time of 59 minutes was computed by summing the 31 minute, 20 minute and 11 minute dark currents, each minus a one minute integration. The linearity of dark current versus time allows the dark current for any exposure time during the same night to be computed by a simple scaling. This requires the assumption that the dark current rate did not vary signif-

TABLE XX . Log of Observations for NGC 7078 (=M15), taken using the 1.8m reflector of the Dominion Astrophysical Observatory, Victoria.

Permanent File&Record	Object	Filter	Exp. Time	Time at End (U.T.)
File 30				1976 Sept.15
records				
140	NGC7078	v	5m	8h 17m
141	Dk	-	1m	8h 19m
142	NGC7078	v	10m	8h 32m
143	Dk	-	1m	8h 36m
144	NGC7078	r	10m	8h 52m
145	Dk	-	1m	8h 54m
146	Dk	-	1m	8h 55m
148	Dk	-	1m	8h 56m
150	Sky	r	1m	8h 57m
152	Sky	v	1m	8h 59m
154	Sky	v	1m	9h 00m
156	Dk	-	1m	9h 03m
276	Dk	-	5m	12h 47m
278(2)288	Dk	-	1m	12h 54m
310	Flat Field	r	1m	13h 21m
312	Flat Field	v	1m	13h 24m
313	Dk	-	1m	13h 25m
314	Flat Field	b	1m	13h 27m
360	Dk	-	11m	14h 53m
362(2)366	Dk	1m	15h 02m	
file 31				1976 Sept. 16
226(2)232	HD172323	r	20s	4h 20m
233(1)235	Dk	-	20s	4h 22m
238(2)246	HD172323	v	20s	4h 26m
248	Dk	-	20s	4h 27m
250(2)260	HD172323	b	20s	4h 30m
262	HD172323	b	1m	4h 31m
263	Dk	-	1m	4h 34m
264(2)266	Dk	-	20s	4h 35m
350	NGC7078	r	20m	7h 41m
352(2)356	NGC7078	r	1m	7h 44m
358	NGC7078	r	6m	7h 50m
360(2)362	NGC7078	r	1m	7h 52m
363	Dk	-	1m	7h 53m
364	NGC7078	b	20m	8h 16m
366(2)368	NGC7078	b	1m	8h 18m
369	Dk	-	1m	8h 21m
370	NGC7078	v	11m	8h 35m
372(2)376	NGC7078	v	1m	8h 38m
377	Dk	-	1m	8h 40m

File 32				1976 Sept. 16
42	Sky	r	6m	12h 14m
44(2)48	Sky	r	1m	12h 17m
50	Sky	v	6m	12h 25m
52(2)56	Sky	v	1m	12h 28m
58	Sky	b	6m	12h 36m
60(2)64	Sky	b	1m	12h 39m
66	Dk	-	6m	12h 46m
68(2)72	Dk	-	1m	12h 49m
74	Dk	-	6m	12h 55m
76(2)80	Dk	-	1m	12h 58m
92	Flat Field	b	1m	13h 22m
93	Dk	-	1m	13h 24m
94	Flat Field	r	1m	13h 26m
95	Dk	-	1m	13h 28m
96	Flat Field	v	1m	13h 29m
97	Dk	-	1m	13h 31m
116	Dk	-	6m	14h 14m
117	Dk	-	1m	14h 15m
118	Dk	-	11m	14h 26m
120(1)123	Dk	-	1m	14h 30m
124	Dk	-	20m	14h 50m
126(2)138	Dk	-	1m	14h 56m
140	Dk	-	31m	15h 28m
142	Dk	-	1m	15h 29m
144(1)148	Dk	-	1m	15h 34m

Notation

i(j)k : Records i, i+j, i+2j,... to k.

The INTERDATA Model 4 was used for data recording.

icantly during the night. Although long dark currents were not measured at the beginning of the night, the linearity of the measurements spread over three hours towards the end of the night of September 16 (U.T.) suggests that the dark current rate was stable. In addition, half-hour exposures taken by A.Condal of planetary nebulae throughout the same night (Sept.16) showed that the dark current rate was very stable, and that the "hot" diodes were always adequately corrected for. The temperature inside the cold-box was checked from time to time and was not seen to vary from some point between -75° and -76° Celsius.

The sky background measurements were made just after the beginning of astronomical dawn, and so may be somewhat excessive. However, the dominant source of error was the baseline fluctuation. The scaled observed per diode sky brightnesses were still very low: 2.3±1.4, 3.0±0.7, 1.6±0.4 instrumental units respectively for the blue (20m), visual (11m) and red (6m) exposures. The errors were computed from the r.m.s. fluctuation of the baseline records F32R68-72 and F32R76-80. The sky brightness values were not much larger than the peak-to-peak baseline fluctuation, even with the moon up and dawn coming.

The reduced images of NGC 7078 are presented as isophotal contours in Figures 46, 47 and 48.

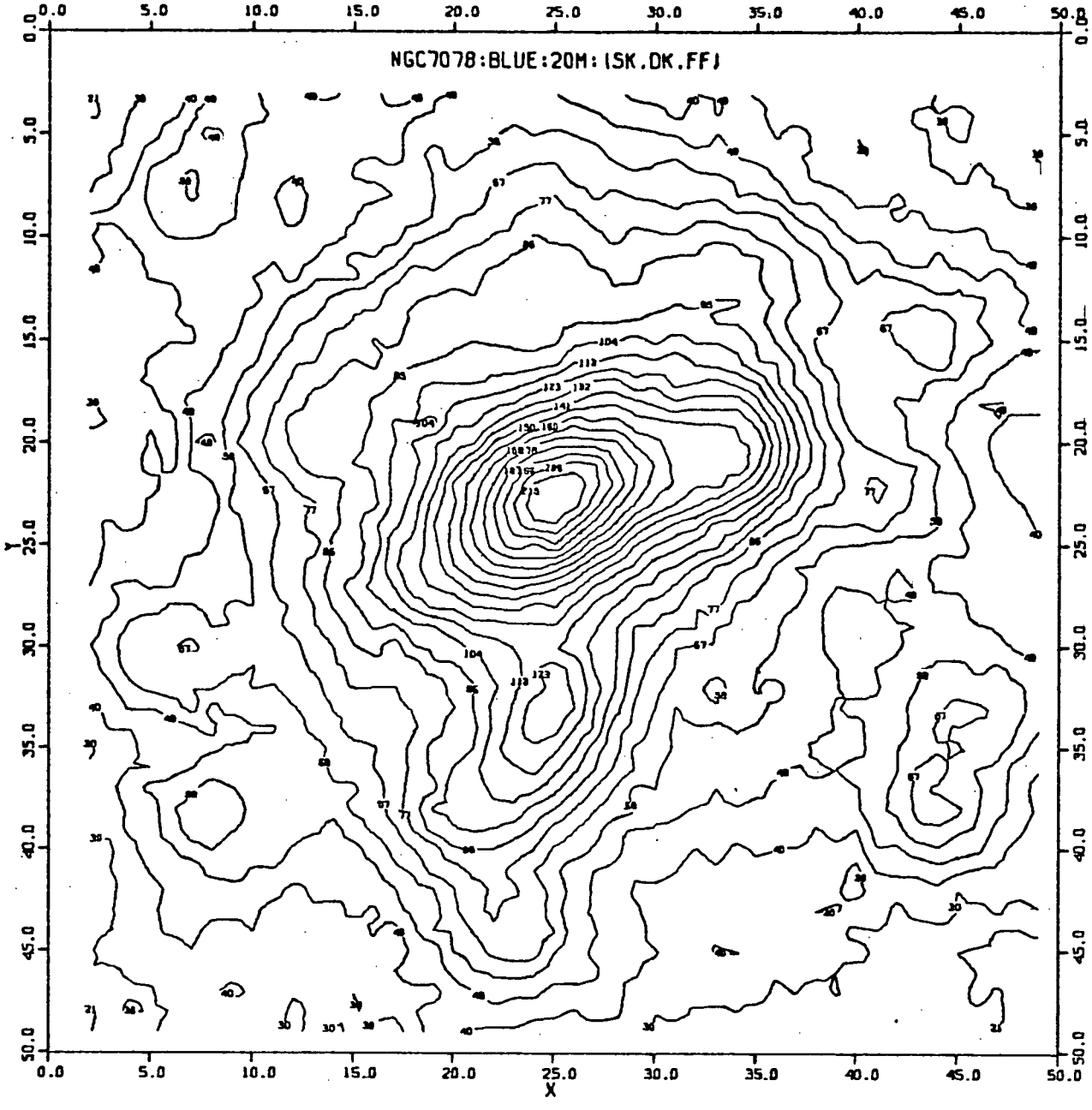

FIGURE 46. NGC 7078: Blue image contour map.

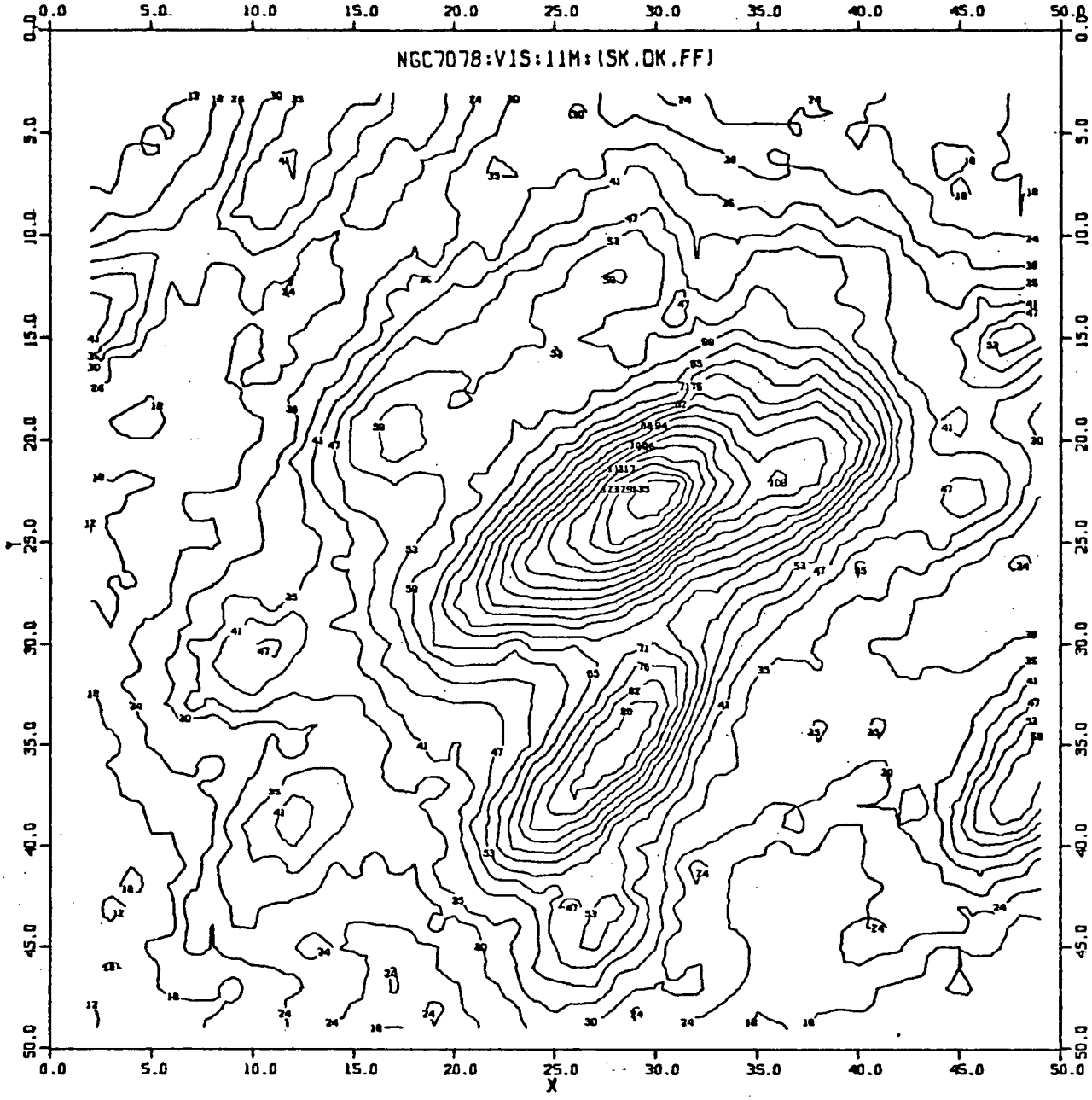

FIGURE 47. NGC 7078: Visual image contour map.

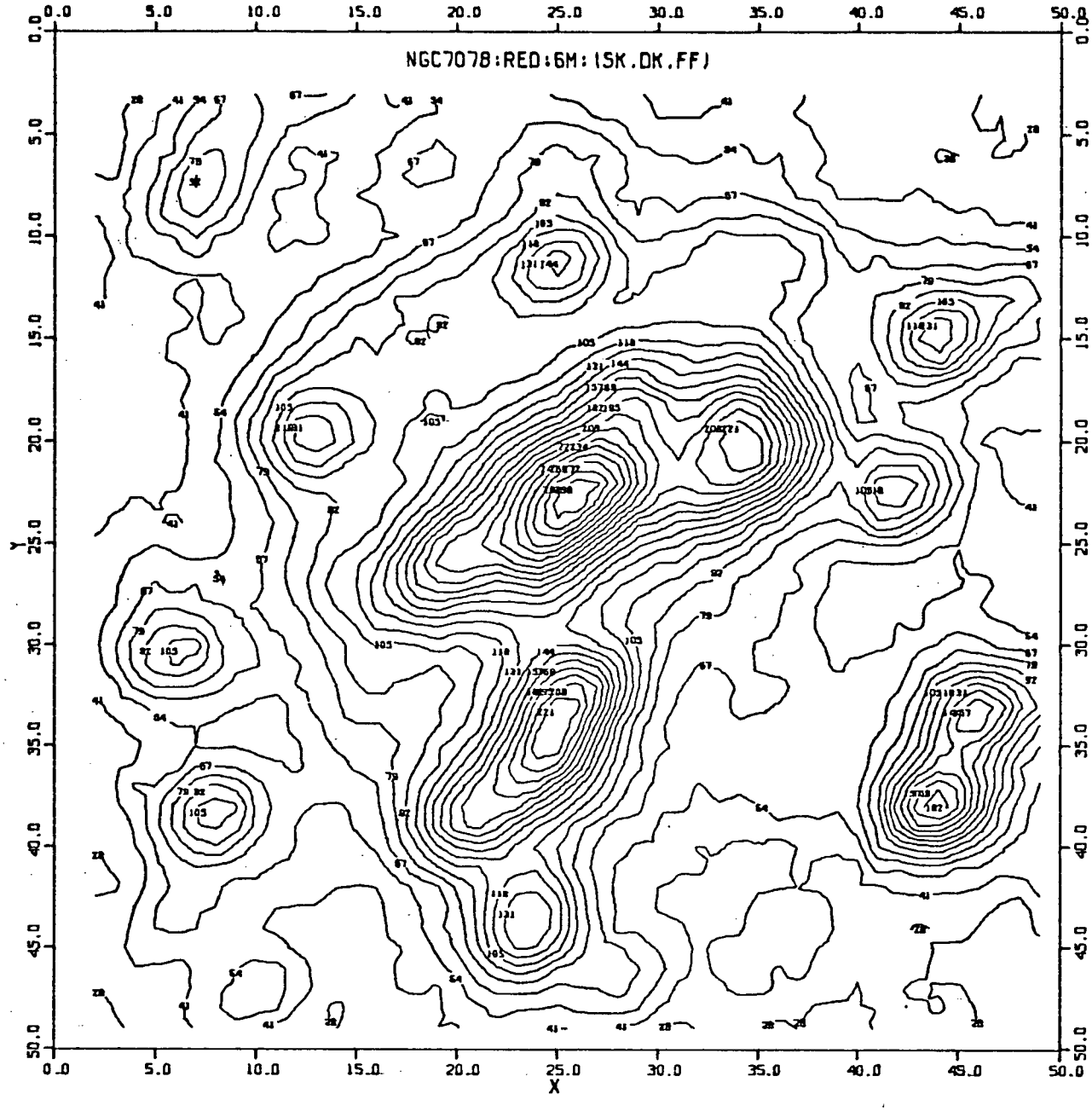

FIGURE 48. NGC 7078: Red image contour map.

5.3 NGC 7078: Scale and Orientation

The lack of very compact (30" x 30") calibrated star fields required the choice of suitably spaced, well measured faint visual doubles. In principle, observing a selection of such doubles and faint single standards in photometric conditions could give a full photometric tie-in as well as a calibration of the plate scale and detector orientation. The time available allowed observations of only one double, HD 172323(=ADS 11503), listed in Table XX . Astrcmetry listed by Aitken(1932) gives a mean separation of 19.83±0.15 arc seconds, at a position angle of 25.0±1.1 degrees (errors are standard deviations). Averaging over the 1 minute blue and 20 second visual and red exposures of HD172323 gives a separation of 31.94±0.03 diode units, at a position angle of -73.8±0.1 degrees in the instrumental system. This yields a plate scale of 0.621±-.005 arc seconds per diode, with the orientations as in Figure 49. It should be noted that the RETICON data gives more consistent spacings and orientations than the published visual micrometry.

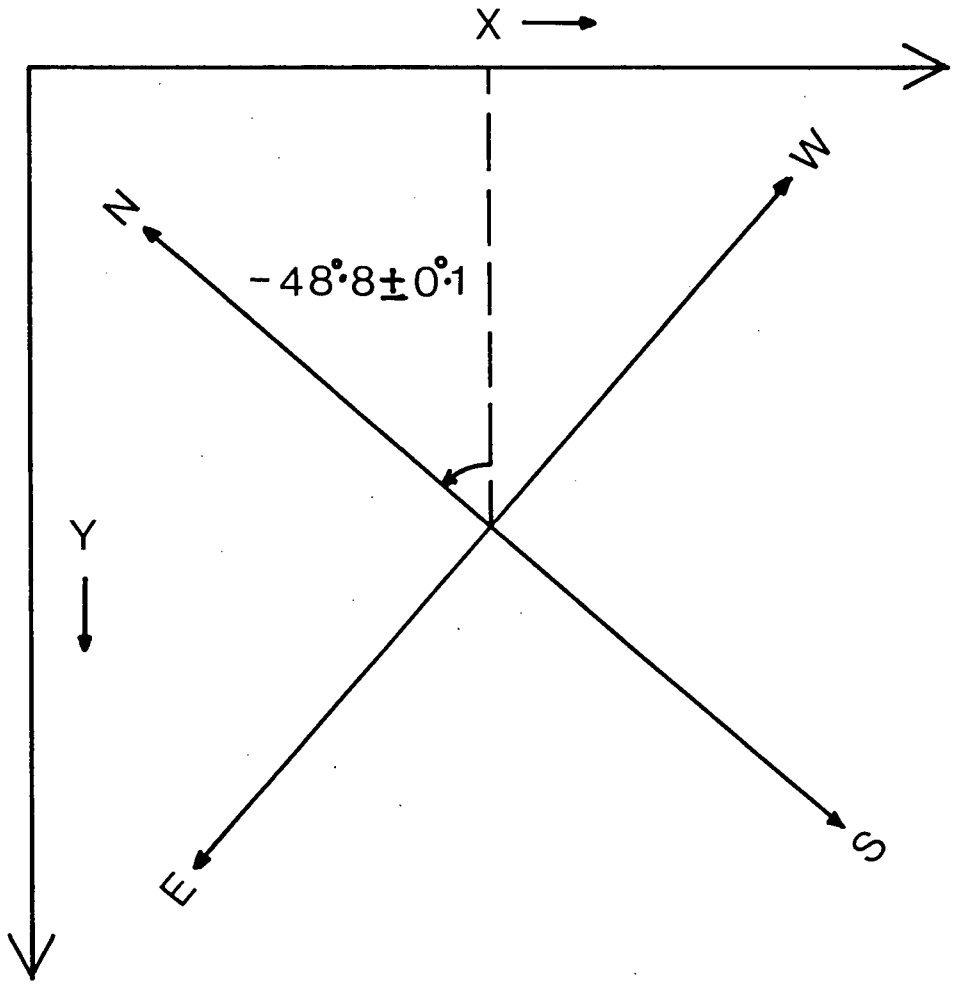

FIGURE 49. Orientation of RETICON camera on D.A.O. 1.8 metre telescope.

5.4 NGC 7078: Approximate Photometric Calibration

Photometry for this double has been published by Roman(1955) and by Eggen(1963). Only Eggen has a separate magnitude and colour for each component: V = 8.08, 10.70, and B-V = 0.58, 1.10, for components A and B respectively.

Isophotal contours were computed for the stellar seeing images. The contour intensities are plotted versus effective radius in Figure 50 using Gaussian scales. The Gaussians defined by the linear portions of the curves in Figure 50 were used to compute the observed magnitude differences between HD-172323 A and B, using the relationship for integrated intensity,

$$I = i(0,0) \int_{-\infty}^{+\infty}\int_{-\infty}^{+\infty} \exp\left\{-\frac{4}{A^2}\left(x^2+y^2\right)\right\} dx\,dy = \frac{\pi A^2}{4}\, i(0,0). \quad (73)$$

The intercepts of Figure 50 are equal to log i(0,0) and the slopes correspond to $-1.737/A^2$, where A is the seeing disk diameter defined by the isophote for 1/e of the central intensity i(0,0). The commonly used seeing definition of Full Width at Half-Maximum (FWHM) corresponds to A multiplied by $\sqrt{-\ln(0.5)} = 0.8325546$. The short exposures for HD172323 gave A= 2.65, 2.67 and 2.33 arc seconds for the b, v, and r filters respectively.

Estimating stellar magnitudes by fitting Gaussians to the seeing disks gave differences between the components δv= 2.68, $\delta(b-v)$= 0.27 and $\delta(v-r)$= 0.28. Using the FIRM square

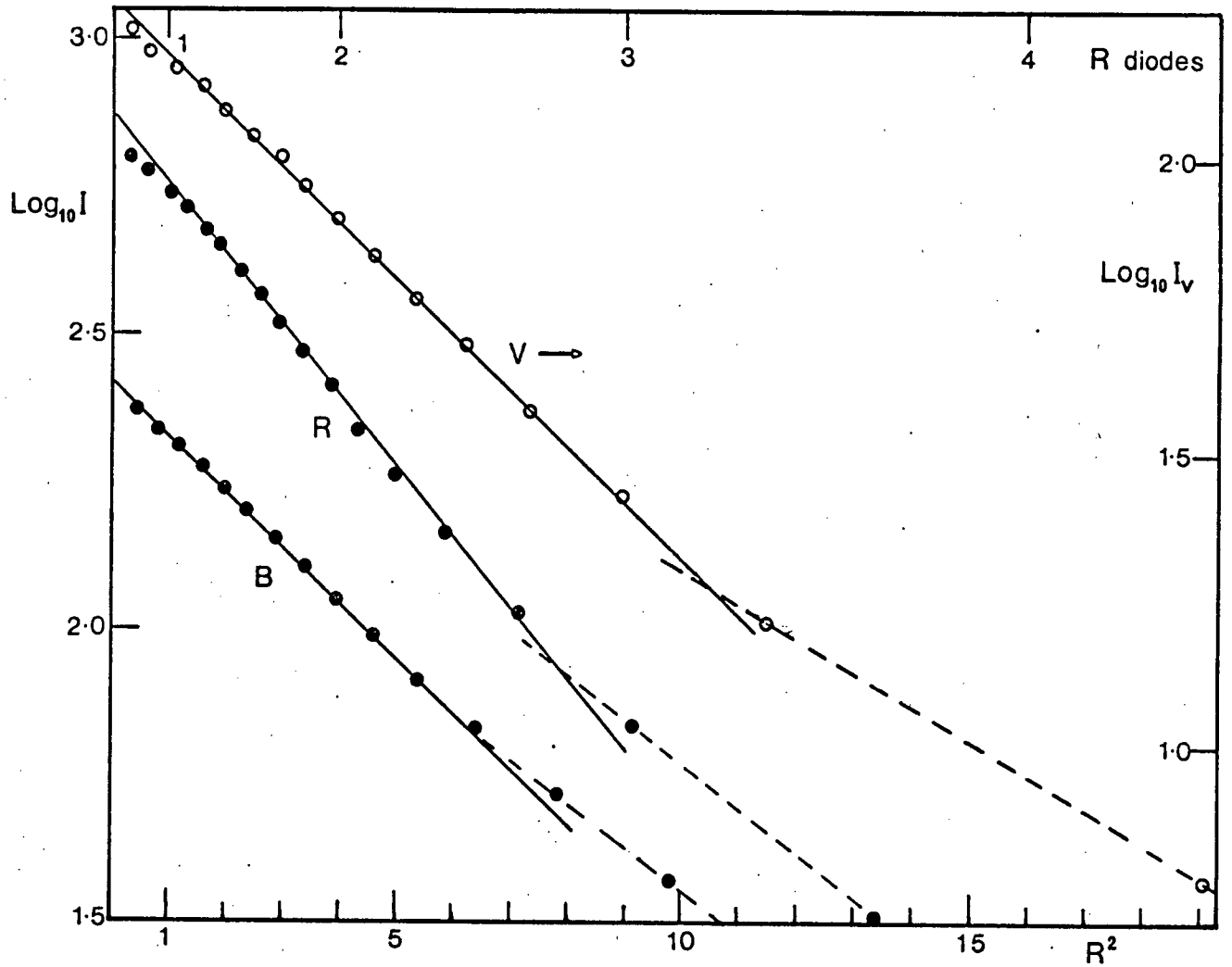

FIGURE 50. Stellar image intensity curves.

aperture instruction APERTURE , with a 15 x 15 diode maximum aperture, the following were obtained: $\delta v = 2.74$, $\delta(b-v) =$ 0.09 to 0.62 (very uncertain due to the proximity to th edge of the field of component A and the faintness of component B in the blue exposures), and $\delta(v-r) = 0.34$. Extensive observations would be needed to establish the photometric validity of the two methods.

Eggen's data correspond to $\delta V = 2.62$, $\delta(B-V) = 0.52$ (in the sense of star B - star A). While the agreement between δv and δV is reasonable, more data was needed to obtain even a rough calibration.

To obtain an approximate colour calibration of the RETICON camera, observations were undertaken using the 30cm Cassegrain reflector of the Department of Geophysics and Astronomy, at UBC. Observations were taken on three nights of unusual clarity (for Vancouver, that is), but only one night could be described as being potentially photometric. Subsequent reductions showed that the transparency or the response varied widely but slowly, allowing some colour measurements to be used. Single stars were chosen from the Arizona-Tonantzintla Catalogue of bright stars in UBVRI (Iriarte et al. 1965). Since the plate scale on the 30cm telescope was about 5 arc seconds per diode, the stars were defocussed to an apparent diameter of about 10 diodes. A direct summation of intensity was performed to obtain a measure of stellar magnitude, the outer regions of the field being used to measure the sky back-

ground. This is in contrast to the Gaussian fitting method for star images at high magnification.

The reductions were performed using a variety of assumed plausible extinction coefficients. Although the zero-points of the transformations could not be accurately evaluated, the scale factors did not vary greatly for different sets of extinction coefficients.

Formally,

$$\left.\begin{aligned} \delta(B-V) &= (1.12 \pm 0.02)\,\delta(b-v) \\ \delta(V-R) &= (1.18 \pm 0.02)\,\delta(v-r) \end{aligned}\right\}, \tag{74}$$

where the errors are estimated from the variations of the coefficients using different extinction coefficients. Allowing for the fact that a different telescope was used for the observations of NGC 7078, I take the following approximate transformations,

$$\left.\begin{aligned} \delta V &= 1.0\ \delta v \\ \delta(B-V) &= 1.1\ \delta(b-v) \\ \delta(V-R) &= 1.2\ \delta(v-r) \end{aligned}\right\} \tag{75}$$

The zero-points can be evaluated by comparison with circular aperture photometry of NGC 7078 (King 1966b). There is little knowledge of the colour dependence of V, but the results for HD172323, which has components of rather different colours, suggest that it may not be large.

5.5 NGC 7078: Centred Aperture Photometry.

Until the advent of panoramic detectors, photometry of the integrated light through apertures of different sizes centred on the nucleus, or by using a small aperture and making spot measurements of different parts of the cluster. NGC 7078 has been observed in either or both these ways by Kron and Mayall(1960), King(1966b), van den Bergh(1967) and Chun(1976). The observations of King(1966b) are the only available data taken through apertures small enough to fit into the field of view of the RETICON camera on the 1.8 metre telescope.

Synthetic circular apertures were computed using the ELLIPSE instruction of FIRM in the aperture mode (MODE=A). The integrated signal, scaled down, is listed in Table XXI . Apertures corresponding to King's two smallest apertures are included. The errors quoted are those for an uncertainty of ±1 unit in the baseline level of each exposure, and are most serious for the larger apertures. Each aperture was centred at the apparent position of the nucleus in each exposure, this

TABLE XXI . Centred circular aperture measures of NGC 7078.

Aperture dia."	b (20 min)	v (11 min)	r (6 min)	Baseline error
5.0	4.28	2.57	5.24	0.02
7.5	8.32	5.00	9.85	0.05
10.0	13.06	7.86	15.34	0.09
11.16*	15.58	9.32	18.30	0.11
12.5	18.50	11.13	21.74	0.14
15.0	24.37	14.67	28.81	0.19
17.5	30.38	18.41	36.02	0.28
20.0	36.35	22.13	42.91	0.36
21.60*	40.13	24.43	47.19	0.42
22.5	42.20	25.73	49.60	0.46
25.0	47.98	29.29:	56.21	0.56

* : Apertures corresponding to those of King (1966b).

: : Aperture touches edge of field.

Integrated intensities have been divided by 2256 (number of live diodes).

Errors correspond to ±1 unit baseline error per diode.

position having an uncertainty of about 0.3 diode units distance.

Instrumental colours and magnitudes are listed in Table XXII , with no corrections for exposure time or extinction since the photometry reported here is differential. Each individual B and V exposure can be calibrated directly using the relevant observations of King(1966b), listed in Table XXIII . Using the transformation equation,

$$B - V = K_0 + K_1 (b - v) \tag{76}$$

with $K_1 = 1.1$ and averaging King's results, we get $K_0 = 1.27$ for the data in Table XXIII .

The immediate result of these measurements is that centred apertures do not show any significant integrated colour variations for different aperture diameters. The slight central reddening in (b-r) is probably due to the better seeing in the r exposure. This effect must be corrected for before colour maps in two dimensions can be computed, and is the subject of the next section.

TABLE XXII . Circular aperture instrumental magnitudes and colours for NGC 7078. Scaling as for Table XXI.

Aperture dia."	v	b-v	b-r
5.0	-1.03±0.01	-0.55±0.01	0.22±0.01
7.5	-1.75	-0.55	0.18
10.0	-2.24	-0.55	0.18
11.16	-2.42	-0.56	0.18
12.5	-2.62	-0.55	0.18
15.0	-2.92±0.013	-0.55±0.02	0.18±0.015
17.5	-3.16	-0.54	0.19
20.0	-3.36	-0.54	0.18
21.60	-3.47	-0.54	0.18
22.5	-3.53	-0.54	0.18
25.0	-3.67:±0.02	-0.54:±0.03	0.17±0.02

TABLE XXIII . Published centred aperture photometry of inner region of NGC 7078 (from King 1966b). Errors are mean errors.

Aperture Dia."	V	B-V
11.16	9.90±0.12	0.64±0.05
21.60	8.94±0.08	0.68±0.03

5.6 NGC 7078: Seeing Analysis And Colour Maps

In order to form a colour map or ratio map from two images, it is necessary that:

(1) the images be in geometrical registration, and,

(2) the combined seeing and instrumental profiles be the same for each image.

An attempt was made to use the spatial power spectra of the images to determine the seeing, but the results were inconclusive. A much simpler method was to use the FIRM instruction SECTION in line mode (MODE=L) to plot the intensity along a line passing through a given point at a specified orientation in the image. The effective diameter of star images was obtained by manually measuring the profiles. The b exposure was found to have a 1/e seeing diameter of 4.0". The v seeing was 3.1" (in a roughly North-South direction perpendicular to the East-West distortion), and the r seeing was 3.2".

The red image therefore had to be smoothed so that its seeing could be degraded to that of the blue image. The diameter of the convolving Gaussian was 2.4", or 3.9 diode spacing units.

The b and v images were brought into registration with the r image by computing the positions of a set of eight stars

in each image, and finding the mean displacement of these stars relative to their positions in the r image. The displacements of the b and v images were corrected for using the Fourier transform shift theorem. A high-pass spatial filter was simulated by convolving each image with a Gaussian of effective "seeing" diameter A= 6 diodes, and subtracting the strongly smoothed image from a lightly smoothed image (A= 1.5 diodes). Only sharp features such as star images were retained, while the underlying distribution of light was removed. The positions of the residual star images were obtained by computing the centroids of their isophotal contours. The registration corrections are listed in Table XXIV .

An alternative registration technique is to compute the correlation function between two images, iterating until a displacement is found which maximizes the correlation (Arp and Lorre 1976). However, this is somewhat time-consuming, whereas the contour-centroid method is quick and gives very consistent positions for images of isolated stars such as the components of wide doubles. The presence of an underlying surface brightness and the crowding of star images alters the contour positions, even after high-pass filtering. This introduces a scatter which appears as the standard deviation in Table XXIV .

Figure 51 is the map of b-r in the instrumental system. Line scans using the SECTION command are shown in Figure 52 for two different orientations, one of which (193.°8) avoids

TABLE XXIV . Positional registration corrections for images of NGC 7078.

Record	Filter	x	y
F31R364	b	0.43±0.31	-0.12±0.14
F31R370	v	-3.67±0.24	-0.25±0.20
F31R358	r	0.	0.

Errors are standard deviations. Eight stellar images (including nucleus) used in each picture. Blue and visual images registered with red image.

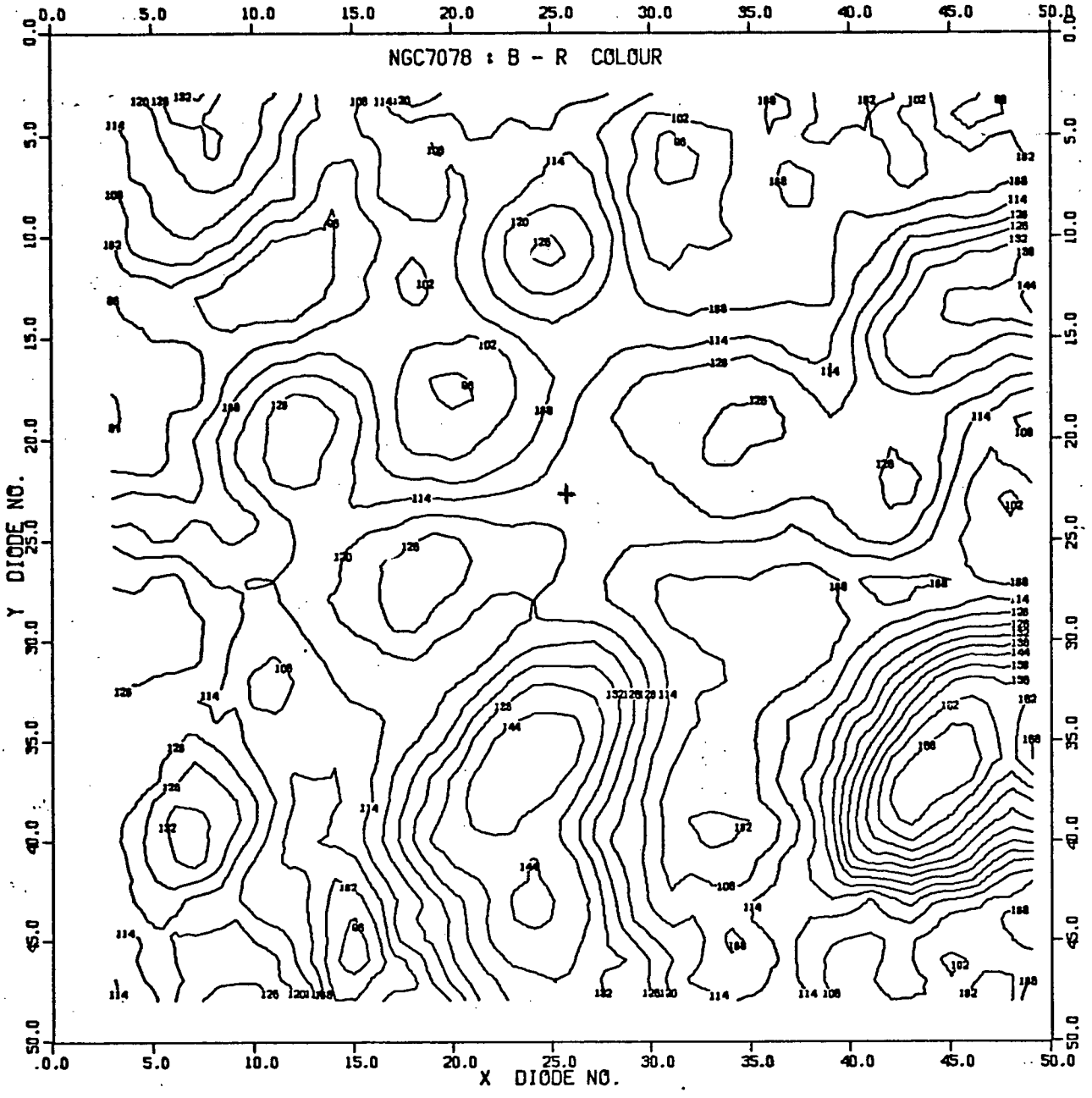

FIGURE 51. NGC 7078: Instrumental B - R colour map. Magnitude difference between smoothed images. 'X' marks nucleus.

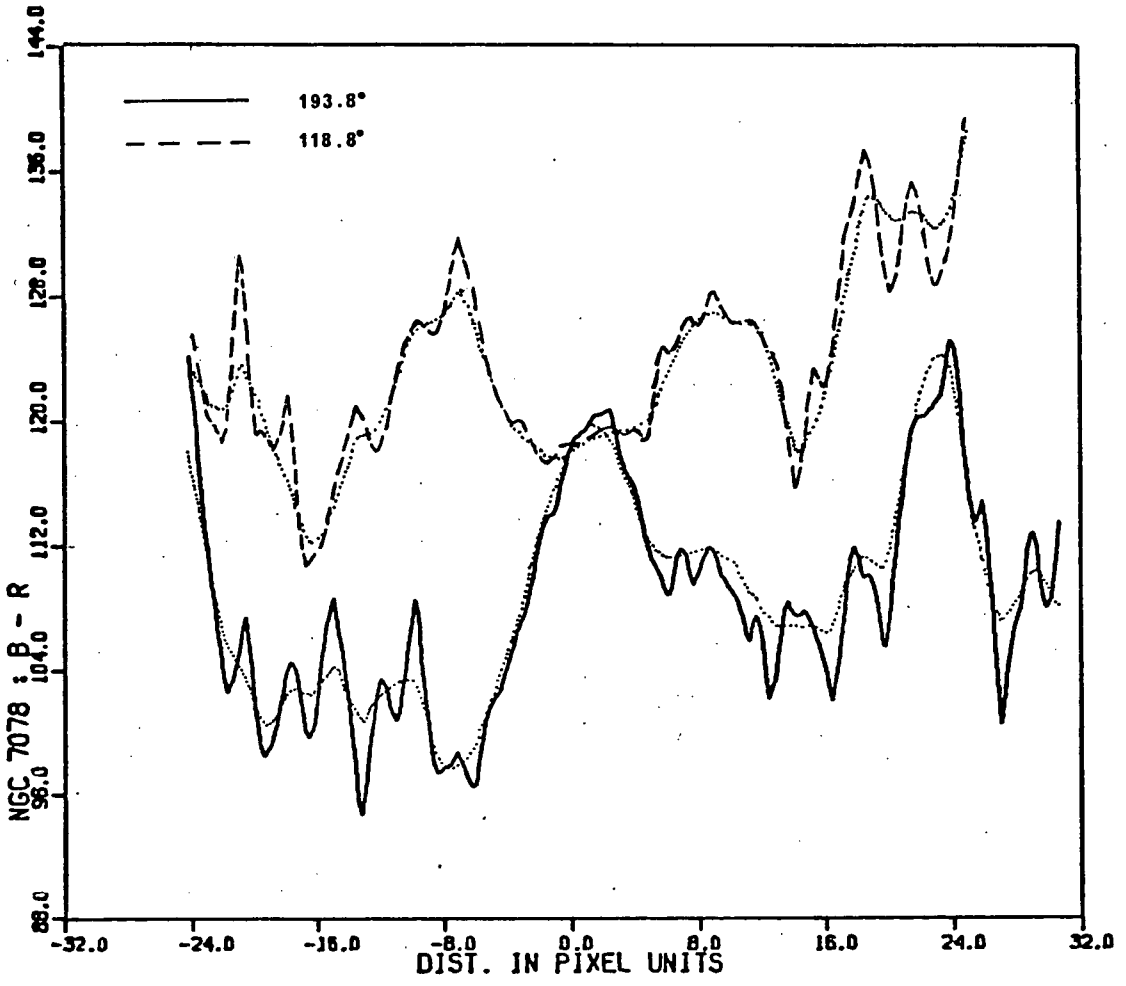

FIGURE 52. Line scans across colour map for two different position angles. Dotted line is for magnitude difference between smoothed images as plotted in Fig. 51. Solid line for unsmoothed images.

bright stars as much as possible. The blue image was convolved with a Gaussian of 2.0 diodes effective diameter, and the red image was convolved with a Gaussian of 4.35 diodes diameter. The effective seeing was therefore about 6.7 diodes.

To obtain a colour-magnitude diagram for even the brightest stars in this object, much better seeing and photometric calibrations are required. An analysis of the star images to extract more information about the makeup of the core region of NGC 7078 has therefore not been attempted.

5.7 NGC 7078: Discussion and Conclusions.

The colour map and sections of Section 5.6 show that most of the bright stars in the field of view are red, and that the nuclear region appears to be slightly redder but not as red as the brightest red giants. Whereas circular aperture photometry shows no average radial colour gradient, a full two-dimensional display shows distinct colour variations, with the underlying unresolved stellar population being much bluer than the red giants and slightly bluer than the nuclear region. However, the poor seeing, about 4 seconds, is such that it is impossible to tell whether the slightly redder nucleus is due to individual red giants of moderate luminosity or to a redder underlying population of lower luminosity stars toward the centre. Leroy, Auriere and Laques (1976), with much better

seeing, find a pair of intensity maxima in the unresolved nuclear region. They choose one of these peaks as the cluster centre. There may therefore be a moderately luminous star within 1" of of the "true" cluster centre, and the colour distribution obtained in this work may be affected by it. However, it is apparent that at the resolution and bandpasses of the observations reported here, no radically unusual colour index variation is to be found in the nuclear region of NGC 7078. This is consistent with the spectroscopic observations of Newell, da Costa and Norris (1976) .

The red exposure in particular shows the importance of separating out the red giants from the less luminous underlying population if a better understanding of the density distribution is to be obtained. Red and infrared images taken using the RETICON camera or with charge-coupled devices are extremely valuable in identifying red giants. Given much better seeing, horizontal branch stars should also be identifiable through a blue filter. The present work demonstrates the effectiveness of the RETICON camera as a tool for exploring the central regions of globular clusters. Standard photographic and photometric techniques are very difficult to use for such work.

CHAPTER 6

SUMMARY AND CONCLUSIONS

6.1 Conclusions.

In this thesis, I have described the development of a multi-diode array area photometer, and its application to an investigation of the central regions of the dynamically interesting galaxy NGC 4736 and the X-ray emitting globular cluster NGC 7078.

The RETICON camera has a rather high effective noise figure of about 8000 electrons. New charge-coupled devices may have effective noise figures of 100 electrons or less, giving about 5 magnitudes improvement in sensitivity. However, the superior performance of the RETICON at high signal levels may continue to make useful the camera developed here. Charge-coupled devices have problems of "blooming" and incomplete charge transfer at high charge levels. A detailed analysis of CCD detection of stellar images is needed to make a quantitative comparison with the RETICON camera.

A theoretical analysis has shown that for a seeing diameter $A \geq 2.5$, (defined at 1/e of I(0)), aliasing is of no consequence at any spatial frequency. photometry of stars is feasible for $A \geq 2.0$ diode spacings. Analysis of double-star observations shows that relative positional accuracies of astrometric standard are possible with this instrument,

provided that there are no serious geometric irregularities in the diode array.

Area photometry of NGC 4736 showed that the surface brightness has an inverse square dependence on radius. The simple empirical King law, originally obtained for the cores of globular clusters (King 1962), was found to give a good approximation for the surface brightness, with a probably unresolved central peak deviating from it. Subtraction of circularly symmetric distributions of intensity reveals a small central bar-like structure, the ends of which meld into the inner spiral structure photographed by Chincarini and Walker (1967). Simple bulge and disk models strongly suggest that two spiral systems exist in NGC 4736, one inside the other, with the inside system rotating perhaps two or three times as rapidly as the outer or main spiral pattern. This involves the assumption that both spirals are two-armed spirals.

Colour maps show that beyond 10 arc seconds there is a strong decrease of colour index with decrease of radius. Inside the central region, the reddest areas are not at the nucleus but rather in the areas where the differences between the observed and calculated surface brightnesses are the most negative. This probably is caused by dust. It appears that dust also defines the inner spiral structure on photographs. This fact and the symmetry of the bar-like structure found in this work strongly suggest a systematic origin for the inner

structure.

A central mass to luminosity ratio of 2.4 to 3.6 was obtained, which is very similar to the value of 2.5 found for the whole galaxy by Bosma, van der Hulst and Sullivan (1977).

Images of the X-ray emitting globular cluster NGC 7078 were recorded in too poor a seeing to allow resolution of the central cusp. An analysis of a colour map of the cluster showed that there exist spatial colour differences, mostly associated with red giants, and that these colour differences are not revealed by centred circular aperture photometry. (A similar effect was noted for the galaxy NGC 4736, in which there probably exist young stars and dust patches). Better resolution is needed to fully separate the effects of the relatively few luminous stars from the "underlying background" of much more numerous lower luminosity stars. The area photometry supports the conclusions based on spectroscopy of Newell, da Costa and Norris (1976) that there is no radical difference between the cusp and the "underlying" population.

6.2 Problems for Future Work.

The RETICON camera should be compared in detail with cameras which employ charge-coupled devices (CCD's). Is the RETICON camera still superior despite its high noise level for the observation of galactic nuclei, globular clusters and stellar positions ? This comparison needs more results from CCD cameras.

The image processing code FIRM should be extended to carry out the following: (i) fit ellipses, including quadrupole terms, to contours using least squares Fourier series fitting, in the manner of Crane (1975),
(ii) produce output in a form suitable for the new COMTAL graphics system to be installed at UBC,
(iii) register images by correlation of complete images,
(iv) accomodate images from larger arrays,
(v) assemble macros (i.e. subroutines) in the FIRM language.

The INTERDATA observing programmes have already been modified by C. Pritchet to include input and output via a visual display unit. A most useful addition, involving extended-precision arithmetic, would be to compute a sharpness criterion for focussing the telescope. Muller and Buffington (1974) have shown that the sum of squares, $\sum I_{ij}^2$ is the most suitable quantity to define focussing in real-time. Allowing for transparency fluctuations, a <u>normalized</u> criterion would be:

$$S = \frac{\Sigma I_{ij}^2}{\left(\Sigma I_{ij}\right)^2} \quad . \tag{77}$$

The most exciting prospects are suggested by the results for the galaxy NGC 4736. The combination of area photometry with rotation curves from optical and radio spectroscopy opens up many possibilities. Not only does area photometry measure projected emissivity and, hopefully, density, but also it can reveal features which photographic methods do not show easily. The information content is azimuthal as well as radial. The importance of this has been demonstrated effectively by Schweizer (1976).

The model for the nuclear region of NGC 4736 strongly suggests that similar structures may exist in galaxies which are morphologically and dynamically similar to NGC 4736, e.g. M31, M81 and our own Galaxy. It would be most interesting to observe a number of galaxies to see whether they contain structure inside the radius where their inner Lindblad resonance is thought to lie.

Data has been obtained for NGC 5194 (= M51) and NGC 4258, although not of as good quality as the data for NGC 4736. This and the polarimetry of NGC 4736 should be reduced in the near future.

It is also very important that a whole galaxy be

observed, not just the inner region. It is most important that some understanding of the run of mass to luminosity ratio within galaxies be gained. Photometry over a much larger region of NGC 4736 and other galaxies is needed.

The vexing question of galactic halos could be resolved if much better knowledge of the distribution of matter in the disks of galaxies could be obtained. While the results of area photometry suggest that mass to luminosity ratios do not vary by much in the inter-arm regions of spiral galaxies (Schweizer 1976), rotation curve data suggests the opposite (Roberts 1975), at least in the outer regions. The high red sensitivity of silicon diode based devices should be very useful in observing the outer reaches of galaxies, since it has been suggested that an outer halo may consist largely of red dwarfs. Low noise and low magnification are required.

Diode array and CCD detectors used at low magnification may also have a cosmological application: the measurement of the isophotal diameters of galaxies. An f/0.8 lens in front of the RETICON has been tried by R.B.Tully and this author, but various problems prevented useful data from being obtained. Great care has to be taken to avoid scattering through multiple reflections and refractions when using such a strongly convergent lens with a multi-diode array. A halo around sharp images was found with the f/0.8 arrangement.

The idea of the two-spiral model needs to be investigated

theoretically. A hydrodynamical rather than particle kinematic model is needed. The work of Sanders and Huntley (1976) and of Sorensen, Matsuda and Fujimoto (1976) represents the starting point for more extensive hydrodynamical calculations. The problem of interaction between the inner pattern and the main disk is probably extremely difficult to treat theoretically, but it could be associated with the problem of the energy source for driving or triggering the main spiral pattern. A possibility which has not been explored in this thesis is that of spirals involving one, three or four arms. One-armed spirals may be contra-rotating, with a negative pattern angular velocity. This is because the inner Lindblad resonance frequency for one-armed spirals is $\Omega - \kappa$, which is negative.

The structure of spheroidal systems such as elliptical galaxies and the bulges of spiral galaxies will be better understood once highly accurate surface brightness and colour maps are available. Development of models and techniques along the lines of the work of Wilson (1975) and Hunter (1975) could allow a determination of the phase distribution function as well as the density distribution. This in turn should shed light on the formation and relaxation processes of galaxies. King (1975) and Wilson (1975) have shown that present knowledge is inadequate to explain the radial variation of isophotal ellipticity in elliptical galaxies. A combined theoretical and observational attack is most desirable.

Work on globular clusters using the RETICON camera is already being undertaken by others. Multi-colour imaging of cluster cores may reveal evidence of a central massive object, the effects of stellar collisions and coalescence, or the presence of close binaries which would accumulate at the centre. These topics were reviewed in Chapter 1. Good seeing is essential if the central regions are to be resolved. Data of unfortunately poor quality has been obtained for a number of globular clusters using the 0.6 metre and 2.2 metre telescopes at Mauna Kea.

Finally, the RETICON camera may be useful as a tool for measuring the separations, orientations and magnitude differences of visual double and multiple stars. Careful observing techniques could make attainable positional accuracies of 0.01 diode spacing units, unless limited by the geometrical uniformity of the detector. A trial programme of observations and measurements is recommended. The rigid mounting and automated data processing of the camera system could make the RETICON a convenient "micrometer" as well as photometer.

REFERENCES

Aarseth, S. J., and Saslaw, W. C. 1972, Ap.J., 172, 17.

Ables, H. D., and Ables, P. G. 1972, Astron. J., 77, 642.

Aitken, R. G. 1932, "New General Catalogue of Double Stars", (Washington: Carnegie Inst.).

Alloin, D., Pelat, D., and Bijaoui, A. 1976, Astr. and Ap., 50, 127.

Altena, W. F. van, and Auer, L. H. 1975, in "Image Processing Techniques in Astronomy", ed. C. de Jager and H. Nieuwenhuijzen (Dordrecht: D. Reidel), p. 411.

Anger, C. D., Fancott, T., McNally, J., and Kerr, H. S. 1973 Appl. Optics 12, 1753.

Antcliffe, G. A. 1975, "Development of CCD Imaging Sensors for Space Applications". Report No. 08-75-41 (Dallas: Texas Instruments).

Arp, H., and Lorre, J. 1976, Ap.J., 210, 58.

Babcock, T. A., Sewell, M. H., Lewis, W. C., and James, T. H. 1974, Astron. J., 79, 1479.

Bahcall, J. N., Bahcall, N. A., and Weistrop, D. 1975, Ap. Lett., 16, 159.

Bahcall, J. N., and Ostriker, J. P. 1975, Nature 256, 23.

Bahcall, J. N., and Ostriker, J. P. 1976, Nature 262, 37.

Baldwin, J. E. 1975, "Dynamics of Stellar Systems", I.A.U. Symp. No. 69, ed. A. Hayli (Dordrecht: D. Reidel), p. 341.

Barbanis, B. 1970, in "The Spiral Structure of Our Galaxy", I.A.U. Symp. No. 38, ed. W. Becker and G. Contopoulos (Dordrecht: D. Reidel), p. 343.

Beaver, E. A., Burbidge, E. M., McIlwain, C. E., Epps, H. W., and Strittmatter, P. A. 1972, Ap.J., 178, 95.

Bergh, S. van den. 1967, Astron. J., 72, 70.

Bergh, S. van den. 1975, Ann. Rev. Astr. and Ap., 13, 217.

Blackman, R. B. and Tukey, J. W. 1959, "The Measurement of Power Spectra", (New York: Dover Publ.)

Bosma, A., van der Hulst, J. M., and Sullivan, W. T. III. 1977, Astr. and Ap., 57, 373.

Bracewell, R. 1965, "The Fourier Transform and its Applications", (New York: McGraw-Hill).

Brandt, J. C. 1960, Ap.J., 131, 293.

Bruyn, A. G. de. 1977, Astr. and Ap., 54, 491.

Buchholz, V. 1972, M. Sc. Thesis, Univ. of B. C.

Buchholz, V. 1974, Unpubl. : "Report On Reticon RL512C Diode Array System".

Buchholz, V., Walker, G. A. H., Auman, J. R., and Isherwood, B. 1973, in "Astronomical Observations with Television-Type Sensors", ed. J. W. Glaspey and G. A. H. Walker (Vancouver: UBC), p. 199.

Burbidge, E. M. 1975, in "Structure and Evolution of Galaxies", NATO Advanced Study Institutes Series, ed. G. Setti (Dordrecht: D. Reidel),

Burbidge, E. M., Burbidge, G. R., and Prendergast, K. H. 1959, Ap.J., 130, 26.

Campbell, B. 1976, Ph. D. Thesis, Univ. of Toronto.

Chandrasekhar, S. 1942, "Principles of Stellar Dynamics", (Chicago: Univ. of Chicago Press). Reprinted 1960 (New York: Dover).

Chincarini, G., and Walker, M. F. 1967, Ap.J., 147, 407.

Chun M.S. 1976, Ph. D. Thesis, Aust. Nat'l. Univ.

Clark, G. W. 1975, Ap.J.(Letters), 199, L143.

Clark, G., Markert, T. H., and Li, F. K. 1975, Ap.J.(Letters), 199, L93.

Cohen, R. J., and Davies, R. D. 1976, M.N.R.A.S., 175, 1.

Contopoulos, G. 1970, in "The Spiral Structure of Our Galaxy", I.A.U. Symp. No. 38, ed. W. Becker and G. Contopoulos (Dordrecht: D. Reidel), p. 303.

Contopoulos, G. 1971, Earth and Extraterr. Sci., 1, 185.

Contopoulos, G. 1975, in "La Dynamique des Galaxies Spirales", ed. L. Weliachew (Paris: CNRS), p. 21.

Crane, P. 1973, in "Astronomical Observations with Television-Type Sensors", ed. J. W. Glaspey and G. A. H. Walker (Vancouver: UBC), p. 391.

Crane, P. 1975, Ap.J., 197, 317.

Cudworth, K. M. 1976, Astron. J., 81, 519.

Da Costa, G. S., and Freeman, K. C. 1976, Ap.J., 206, 128.

Dainty, J. C., and Shaw, R. 1974, "Image Science", (New York: Academic Press), p. 220.

Davis, M. 1975, Astron. J., 80, 188.

Devinney, E. J., Fischel, D., and Klinglesmith, 1975. in "Image Processing Techniques in Astronomy", ed. C. de Jager and H. Nieuwenhuijzen (Dordrecht: D. Reidel), p. 135.

Dravins, D. 1975, in "Image Processing Techniques in Astronomy", ed. C. de Jager and H. Nieuwenhuijzen (Dordrecht: D. Reidel), p. 97.

Eggen, O. J. 1963, Astron. J., 68, 483.

Emerson, D. T., and Baldwin, J. E. 1973, M.N.R.A.S., 165, 9P.

Faber, S. M. 1971, Ph. D. Thesis, Harvard University.

Faber, S. M. and Gallagher, J. S. 1976, Ap.J., 204, 365.

Faber, S. M. and Jackson, R. E. 1976, Ap.J., 204, 668.

Fairchild Corp. 1976, "CCD211: 244x190 Element Area Image Sensor", Preliminary Data Sheet (mountain View: Fairchild Corp.)

Feibelman, W. A. 1977, Bull. A.A.S., 9, 343.

Fischel, D. 1976, Astron. J., 81, 285.

Frank, J., and Gisler, G. 1976, M.N.R.A.S., 176, 533.

Frank, J., and Rees, M. J. 1976, M.N.R.A.S., 176, 633.

Freeman, K. C. 1970, Ap.J., 160, 811.

Freeman, K. C. 1975, "Dynamics of Stellar Systems", I.A.U. Symp. No. 69, ed. A. Hayli (Dordrecht: D. Reidel), p. 367.

Geary, J. C. 1975, Ph. D. Thesis, Univ. of Arizona.

Geary, J. C. 1976, in "Applications Astronomiques des Recepteurs a Reponse Lineaire", I.A.U. Coll. No. 40, ed. M. Duchesne And G. Lelievre (Paris: Obs. de Paris-Meudon), Section 28.

Giacconi, R., Murray, S., Gursky, H., Kellogg, E., Schreier, E., Matilsky, T., Koch, D., and Tananbaum, H. 1974, Ap. J. Suppl., 27, 37.

Goldberg, B. 1973, Ph. D. Thesis, Univ. of B. C.

Gott, G. J. III. 1975, "Dynamics of Stellar Systems", I.A.U. Symp. No. 69, ed. A. Hayli (Dordrecht: D. Reidel), p. 271.

Gott, G. J. III, and Thuan, T. X. 1976, Ap.J., 204, 649.

Harris, W. E. 1976, Astron. J., 81, 1095.

Hills, J. G., and Day, C. A. 1976, Ap. Lett., 17, 87.

Hog, E., and Wiskott, P. 1974, ESO Tech. Report 5.

Hohl, F. 1972, in "Gravitational N-Body Problem", I.A.U. Coll. No. 10, ed. M. Lecar (Dordrecht: D. Reidel), p.231

Hohl, F. 1976, Astron. J., 81, 30.

Holmberg, E. 1958, Medd. Lunds. Astron. Obs. Ser. II, No. 136.

Horlick, G., and Codding, E. G. 1973, Anal. Chem., 45, 1490.

Hubble, E. 1930, Ap.J., 71, 231.

Humason, M. L., Mayall, N. U., and Sandage, A. R. 1956, Astron. J., 61, 97.

Hunter, C. 1975, Astron. J., 80, 783.

Hunter, C. 1977, Astron. J., 82, 271.

Huntley, J. M., and Saslaw, W. C. 1975, Ap.J., 199, 328.

Illingworth, G., and Freeman, K. C. 1974, Ap.J.(Letters), 188, L83.

Illingworth, G., and Illingworth, W. 1976, Ap. J. Suppl., 30, 227.

Illingworth, G. D., and King, I. R. 1977, Bull. A.A.S., 9, 343.

Iriarte, B., Johnson, H. L., Mitchell, R. I., and Wisniewski, W. K. 1965, Sky and Telescope, 30, 21.

Johnson, H. L. 1965, Comm. Lunar and Plan. Lab., 3, 79, (No. 54).

Johnson, H. M. 1957, Astron. J., 62, 19.

Johnson, H. M., and Hanna, M. M. 1972, Ap.J.(Letters), 174, L71.

Kadla, Z. I., Richter, N., Strugatskaya, A. A., and Hogner, W. 1976, Sov. Astron. 20, 49.

Kamp, P. van de. 1975, Ann. Rev. Astr. and Ap., 13, 295.

King, I. R. 1962, Astron. J., 67, 471.

King, I. R. 1965, Astron. J., 70, 376.

King, I. R. 1966a, Astron. J., 71, 64.

King, I. 1966b, Astron. J., 71, 276.

King, I. R. 1975, "Dynamics of Stellar Systems", I.A.U. Symp. No. 69, ed. A. Hayli (Dordrecht: D. Reidel), p.99 (see p. 112).

King, I., Hedemann, E. Jr., Hodge, S. M., and White, R. E. 1968, Astron. J., 73, 456.

Klinglesmith, D. A. 1975 in "Image Processing Techniques in Astronomy", ed. C. de Jager and H. Nieuwenhuijzen (Dordrecht: D. Reidel), p. 271.

Kormendy, J. 1973, Astron. J., 78, 255.

Kormendy, J. 1976, Ph. D. Thesis, Cal. Tech.

Kron, G. E., and Mayall, N. U. 1960, Astron. J., 65, 581.

Kron, G. E., and Papiashvili, I. I. 1967, P.A.S.P., 79, 9.

Kruit, P. C. van der. 1971, Astr. and Ap., 15, 110.

Kruit, P. C. van der. 1974, Ap.J., 188, 3.

Kruit, P. C. van der. 1976, Astr. and Ap., 52, 85.

Krumm, N., and Salpeter, E. E. 1977, Astr. and Ap., 56, 465.

Landolt, A. U. 1969, P.A.S.P., 81, 443.

Lara, E. de, Chavarria, K. C., Johnson, H. L., and Moreno, R. 1977, Revista Mex. de Astron. y Astrofis., 2, 65.

Larson, R. B. 1975, "Dynamics of Stellar Systems", I.A.U. Symp. No. 69, ed. A. Hayli (Dordrecht: D. Reidel), p. 247.

Leroy, J. L., Auriere, M., and Laques, P. 1976, Astr. and Ap., 53, 227.

Light, E. S., Danielson, R. E., and Schwarzschild, M. 1974, Ap.J., 194, 257.

Lin, C. C. 1975, in "Structure and Evolution of Galaxies", NATO Advanced Study Institutes Series, ed. G. Setti (Dordrecht: D. Reidel), p. 119.

Lindblad, B. 1956, Stockholm Ob. Ann., 19, No. 2.

Lindblad, B. 1959, Handbuch der Phys., 53, 21.

Lindblad, P. O. 1974, in "The Formation and Dynamics of Galaxies", I.A.U. Symp. No. 58, ed. J. R. Shakeshaft (Dordrecht: D. Reidel), p. 399.

Livingston, W. C. 1973, Ann. Rev. Astr. and Ap., 11, 95.

Livingston, W. C. 1975, in "Image Processing Techniques in Astronomy", ed. C. de Jager and H. Nieuwenhuijzen (Dordrecht: D. Reidel), p. 21.

Livingston, W. C. 1976, in "Applications Astronomiques des Recepteurs a Reponse Lineaire", I.A.U. Coll. No. 40, ed. M. Duchesne And G. Lelievre (Paris: Obs. de Paris-Meudon), Section 22.

Livingston, W. C., Harvey, J., Slaughter, C., and Trumbo, D. 1976, Appl. Opt., 15, 40.

Lorre, J. 1975, Ap.J., 202, 696.

Lowrance, J. L., Zucchino, P., and Williams, T. B. 1976, in "Applications Astronomiques des Recepteurs a Reponse Lineaire", I.A.U. Coll. No. 40, ed. M. Duchesne And G. Lelievre (Paris: Obs. de Paris-Meudon), Section 18.

Lynden-Bell, D. 1967, M.N.R.A.S., 136, 101.

Lynds, B. T. 1974, Ap. J. Suppl., 28, 391.

Marochnik, L. S. and Suchkov, A. A. 1975, Sov. Phys.-Usp., 17, 85.

Matsuda, T., and Nelson, A. H. 1977. Nature, 266, 607.

McCord, T. B., Kinnucan, P. F., and Fawcett, G. 1975, in "Image Processing Techniques in Astronomy", ed. C. de Jager and H. Nieuwenhuijzen (Dordrecht: D. Reidel), p. 329.

Mertzanides, C. 1976, Astr. and Ap., 50, 395.

Mestel, L. 1963, M.N.R.A.S., 126, 553.

Michie, R. 1963a, M.N.R.A.S., 125, 127.

Michie, R. 1963b, M.N.R.A.S., 126, 499.

Miller, R. H. 1972, in "Gravitational N-Body Problem", I.A.U. Coll. No. 10, ed. M. Lecar (Dordrecht: D. Reidel), p.213.

Monnet, G., and Simien, F. 1977, Astr. and Ap., 56, 173.

Morton, D. C., and Chevalier, R. A. 1972, Ap.J., 174, 489.

Muller, R. A., and Buffington, A. 1974. J.O.S.A., 64, 1200.

Newell, B., da Costa, G. S., and Norris, J. 1976, Ap.J.(Letters), 208, L55.

Newell, B. 1977, Private Communication.

Nieuwenhuijzen, H. 1975, in "Image Processing Techniques in Astronomy", ed. C. de Jager and H. Nieuwenhuijzen (Dordrecht: D. Reidel), p. 285.

Nordsieck, K. H. 1973a, Ap.J., 184, 719.

Nordsieck, K. H. 1973b, Ap.J., 184, 735.

Nozawa, Y., and Davis, R. J. 1971, in "Astronomical Use of Television-Type Image Sensors", ed. V. R. Boscarino (Springfield, VA: National Technical Information Service), p. 13.

O'Connell, R. W. 1974, Ap.J.(Letters), 193, L49.

O'Connell, R. W. 1976, Ap.J., 206, 370.

Ogorodnikov, K. F. 1965, "Dynamics of Stellar Systems" (Oxford: Pergamon Press).

Oort, J. H., and Plaut, L. 1975, Astr. and Ap., 41, 71.

Ostriker, J. P., Peebles, P. J. E., and Yahil, A. 1974, Ap.J.(Letters), 193, L1.

Peebles, P. J. E. 1972, Ap.J., 178, 371.

Pellet, A. 1976, Astr. and Ap., 50, 421.

Perek, L. 1962, Adv. in Astron. and Astrophys. 1,165.

Peterson, C. J. 1976, Astron. J., 81, 617.

Peterson, C. J., Ford, W. K. Jr., and Rubin, V. C. 1977, Astron. J., 82, 32.

Peterson, C. J., and King, I. R. 1975, Astron. J., 80, 427.

Poveda, A. 1958, Bol. Obs. Ton. y Tacubaya, No. 17.

Poveda, A., Iturriaga, R., and Orozco, I. 1960, Bol. Obs. Ton. y Tacubaya, No. 20.

Prendergast, K. H. and Tomer, E. 1970, Astron. J., 75, 674.

Pritchet, C. 1975, Ph. D. Thesis, University of Toronto.

Pritchet, C. 1977, Ap. J. Suppl., (publ. pending).

Quirk, W. J. 1972, in "Gravitational N-Body Problem", I.A.U. Coll. No. 10, ed. M. Lecar (Dordrecht: D. Reidel), p.250.

Roberts, M. S. 1975, "Dynamics of Stellar Systems", I.A.U. Symp. No. 69, ed. A. Hayli (Dordrecht: D. Reidel), p. 331.

Roberts, M. S., and Rots, A. H. 1973, Astr. and Ap., 26, 483.

Roberts, W. W. 1974, IAU Highlights in Astronomy, 3, ed. G. Contopoulos.

Roberts, W. W., Roberts, M. S., and Shu, F. H. 1975, Ap.J., 196, 381.

Roman, N, G. 1955, Ap. J. Suppl., 2, 195.

Rots, A. H. 1975, Astr. and Ap., 45, 43.

Rubin, V. C. and Ford, W. K. 1971, Ap.J., 170, 25.

Ruiz, M. T. 1976, Ap.J., 207, 382.

Ruiz, M. T., and Schwarzschild, M. 1976, Ap.J., 207, 376.

Sandage, A. R. 1961, "The Hubble Atlas of Galaxies", (Washington: Carnegie Institution).

Sandage, A. R. 1970, Ap.J., 162, 841.

Sanders, R. H., and Bania, T. M. 1976, Ap.J., 204, 341.

Sanders, R. H., and Huntley, J. M. 1976, Ap.J., 209, 53.

Sargent, W. L. W., Schechter, P. L., Boksenberg, A., and Shortridge, K. 1977, Ap.J., 212, 326.

Sargent, W. L. W., and Tinsley, B. M. 1974, M.N.R.A.S., 168, 19P.

Schmidt, M. 1956, B.A.N., 13, 15.

Schmidt, M. 1975, Ap.J., 202, 22.

Schommer, R. A. and Sullivan, W. T. III. 1976, Ap. Lett., 17, 191.

Schweizer, F. 1976, Ap. J. Suppl., 31, 313.

Shu, F. H., Stachnik, R. V., and Yost, J. C. 1971, Ap.J., 166, 465.

Silk, J., and Arons, J. 1975, Ap.J.(Letters), 200, L131.

Simkin, S. M. 1967, Astron. J., 72, 1032.

Simkin, S. M. 1970, Ap.J., 159, 463.

Sorensen, S. A., Matsuda, T., and Fujimoto, M. 1976, Ap. Sp. Sci., 43, 491.

Spitzer, L., and Harm, R. 1958, Ap.J., 127, 544.

Toomre, A. 1963, Ap.J., 138, 385.

Tremaine, S. D., Ostriker, J. P. and Spitzer, L. Jr. 1975, Ap.J., 196, 407.

Tremaine, S. D., 1976a, Ap.J., 203, 72.

Tremaine, S. D., 1976b, Ap.J., 203, 345.

Tull, R. D., and Nather, R. E. 1973, in "Astronomical Observations with Television-Type Sensors", ed. J. W. Glaspey and G. A. H. Walker (Vancouver: UBC), p. 171.

Tully, R. B. 1972, Ph. D. Thesis, University of Maryland.

Tully, R. B. 1974a, Ap. J. Suppl., 27, 415.

Tully, R. B. 1974b, Ap. J. Suppl., 27, 437.

Tully, R. B. 1974c, Ap. J. Suppl., 27, 449.

Turner, E. L. 1976, Ap.J., 208, 304.

Turnrose, B. E. 1976, Ap.J., 210, 33.

Vaucouleurs, G. de. 1959, Handbuch der Phys., 53, 311.

Vaucouleurs, G. de. 1963, Ap. J. Suppl., 8, 31.

Vaucouleurs, G. De. 1974, in "The Formation and Dynamics of Galaxies", I.A.U. Symp. No. 58, ed. J. R. Shakeshaft (Dordrecht: D. Reidel), p. 335.

Vaucouleurs, G. de, Corwin, H. G. Jr., and Bollinger, G. 1977, Ap. J. Suppl., 33, 229.

Vaucouleurs, G. de, and Freeman, K. C. 1972 Vistas in Astronomy, 14, 163.

Vaucouleurs, G. de, and Vaucouleurs, A. de. 1964, "Reference Catalogue of Bright Galaxies", (Austin: Univ. of Texas Press).

Walker, G. A. H., Buchholz, V. L., Camp, D., Isherwood, B., Glaspey, J., Coutts, R., and Condal, A. 1974, Rev. Sci. Instr., 45, 1349.

Walker, G. A. H., Buchholz, V., Fahlman, G. G., Glaspey, J., Lane-Wright, D., Mochnacki, S., and Condal, A. 1976, in "Applications Astronomiques des Recepteurs a Reponse Lineaire", I.A.U. Coll. No. 40, ed. M. Duchesne And G. Lelievre (Paris: Obs. de Paris-Meudon), Section 24.

Warner, P. J., Wright, M. C. H., and Baldwin, J. E. 1973, M.N.R.A.S., 163, 163.

Weckler, G. P. 1967, IEEE J. Solid-State Circuits, SC-2, 65.

Weckler, G. P. 1976, in "Solid State Imaging", ed. P. G. Jespers, F. van de Wiele and M. H. White (Leyden: Noordhoff), p. 131.

Wells, D. C. 1975, in "Imaging in Astronomy", Technical Digest, Meeting June 18-21, 1975, Cambridge, Mass. Section SA2.

White, M. H. 1976a, in "Solid State Imaging", ed. P. G. Jespers, F. van de Wiele and M. H. White (Leyden: Noordhoff), p. 3.

White, M. H. 1976b, in "Solid State Imaging", ed. P. G. Jespers, F. van de Wiele and M. H. White (Leyden: Noordhoff), p. 165.

White, M. H. 1976c, in "Solid State Imaging", ed. P. G. Jespers, F. van de Wiele and M. H. White (Leyden: Noordhoff), p. 485.

Wielen, R. 1974, P.A.S.P., 86, 341.

Williams, T. B. 1975, Ap.J., 199, 586.

Williams, T. B. 1976, Ap.J., 209, 716.

Williams, T. B. 1977, Ap.J., 214, 685.

Wilson, C. P. 1975, Astron. J., 80, 175.

Wolfe, A. M., and Burbidge, G. R. 1970, Ap.J., 161, 419.

Worden, S. P. 1974, P.A.S.P., 86, 92.

Yoshizawa, M. and Wakamatsu, K. 1975, Astr. and Ap., 44, 363.

Zucchino, P., and Lowrance, J. 1971, in "Astronomical Use of Television-Type Image Sensors", ed. V. R. Boscarino (Springfield, VA: National Technical Information Service), p. 27.

APPENDIX I

FIRM

FORTRAN Interactive Record Manipulation.

A Manual By

S.W.Mochnacki

Dept. of Geophysics and Astronomy,

University of British Columbia.

A Reduction Programme For Data For The RETICON RA50x50

Two-dimensional Camera.

For IBM 370/168 Under MTS.

October 1977.

FIRM: Fortran Interactive Record Manipulation.

Purpose:

A programme to process data from a 50 x 50 two-dimensional image detector, using a simple language to specify the records to be reduced and the operations to be performed. It can be used either in batch mode or interactively, but the hard output from batch mode is more valuable in certain cases.

How to Use:

1. Mount the necessary tapes. The tapes are optional (e.g. a theoretical model may be the purpose of a FIRM run), and either input, output or both tapes can be used. In completeness:

```
$MOUNT
input tape rack no., *IN* SIZE =5040 VOL=label
output tape rack no., *OUT* SIZE=20000 { VOL=label RING=IN }
$ENDFILE
$CONTROL *IN* POSN =*2*
```

N.B. The $CONTROL command is <u>essential</u> if the input tape is being used.

2. Run Command:

$RUN SM71:FIRM 2={status file} 3=*IN* 4=*OUT*
{5=commands 6=printfile}

Followed by source cards in the FIRM language. At the end of the deck (or terminal commands), we have:

END

$ENDFILE

Run parameters:

2={ status file}: specifies name of an MTS line file containing the labels of the records on the output tape. The file is organized as follows:

line no.	contents
1.000	label for first record on output tape.
1.500	label for this file and tape.
2.000	label for second record.
3.000	" " third "
(etc)	(etc).

N.B. See Tape Procedures about setting up this file.

3=*IN* :input tape "pseudo device name".

=*DUMMY* if not using a raw data input tape.

Always mount *IN* with RING=OUT (i.e. never specify RING=IN).

4=*OUT* :output tape "pseudo device mame".

=*DUMMY* if no reduced output to be retrieved from or written on the "out" tape.

5= COMMANDS : input commands to FIRM (defaults to *SOURCE*)

6= printfile : printed output from FIRM (defaults to *SINK*)

9=PLOTFILE :name of plot output file for UBC plotting routines (see UBC PLOT). This can be a temporary file, e.g. -PLOTF . In such a case, the following must be placed before $SIGNOFF if the plots are wanted:

```
$RUN PLOT:Q PAR=-PLOTF
```

Notes:

1. The output status file (FORTRAN unit 2) is used to keep track of the number of records on the output tape. The output tape is automatically positioned using the data stored in the output status file, while a new record number for the output record is automatically allocated by FIRM , and returned to the user.

A complete listing of record labels is automatically printed at the end of any FIRM run involving the output tape.

2. The output tape *OUT* can be mounted with RING=IN if WRITE is to be used, and RING=OUT if RETRIEVE but not WRITE is being used.

FIRM conventions in this description:

1. Notation in description:

(a) { } : brackets around parameter or string means that each enclosed parameter is optional and has a default value, usually 0.0 or 1.0 if a real number, and 1 or 6 if an array index, or the current value if a file index (in LOAD, AVERAGE etc.).

(b) [ ] : one of the enclosed parameter names or values must be included.

(c) PAR=XX : such parameters can be in any order, except MODE= , which must be first in a list if required.

2. Operands for internal operations:

Operations of the form:

OPER IA, IB

mean that array IB operates upon IA and the result is stored in array IA, e.g. ADD IA,IB means that array IB is added to array IA, the result being stored in array IA.

Delimiters and lengths:

(i) Operation code.

The operation code (e.g. LOAD, RETRIEVE, LABEL) can have up to 8 characters, but only the first two characters are necessary and significant (e.g. LO, RE, LA). Blank in the first column causes the card to be ignored.

(ii) Array specification:

There are six (6) storage or "register" arrays in core memory, labelled 1 to 6. The array operands always follow the operation code unless not needed. The array operands always follow the operation code unless not needed. The array numbers must be separated from the operation code and from each other by a blank, a comma or both.

(iii) parameters:

Parameters must be separated by a blank, or a comma. Parameters of the MODE=NAME type must be first in the parameter list following the register array specification. Parameters of the PAR=XX type can be in any order, and are optional or mandatory as specified in the command descriptions. The equal

signs are optional, and can be replaced by a blank or comma, e.g.:

PLOT 2,NCONT=20,MIN=2.0

can be written as:

PL 2 MI 2 NC 20

Note that the decimal point is optional in such cases if there is no decimal fraction.

N.B. A fairly verbose and punctuated style is recommended since it allows for errors to be detected more easily and is better practice altogether. The more verbose form of the example above makes more sense to the user.

(iv) Minimum requirements:

The underlined portions of character strings are the minimum requirements for the string to be recognized by FIRM , e.g.

LOAD 5,FILE 9 RECORD 10

can be as terse as:

LO 5, F 9 R 10

Mis-spellings outside the minimum (significant) range do not matter, so long as the maximum string size is not exceeded and the delimiters : blank ' ', dollar '$', equal '=' and comma ',' are not used.

General Example

```
RFS CARD
$SIGNON MYID T=20 PAGES=99
PASSWORD
$MOUNT
RD0678 *IN* VOL=P04071
RF0010 *OUT* SIZE=20000 RING=IN
$ENDFILE
$CONTROL *IN* POSN=*2*
$RUN SM71:FIRM 2=TPSTATUS 3=*IN* 4=*OUT* 9=-PLOTF
ROW 1,0 2,0 50,0
COL 1,0 50,0
LOAD 1,FILE 10 REC 20
AVERAGE 2,REC 21,25
SUBTRACT 1,2
LABEL 1,'NGC 1000:RED:5 MIN:15 OCT'
VIEW 1, 10.
EXAMINE AVERAGE 1
PLOT 1,NCONT=20,MIN=5.0
WRITE 1
PRINT 1
END
$ENDFILE
$RUN PLOT:Q PAR=-PLOTF
$SIGNOFF
```

Notes

1. This example assumes that the input tape is labelled (see UBC TAPE), with volume label P04071.

2. The output tape in this case is unlabelled and on the "floating rack" at the Computer Centre.

3. The file SM71:FIRM contains the contour and Fourier transform routines.

Tape procedures and setting up.

The FORTRAN programme FIRM handles raw data from the UBC RETICON RA50X50 area photometer plus a set of instructions in the FIRM language as input, with output on a variety of devices: line printer, plotter, magnetic tape and disk-resident direct-access MTS line file. Reduced data can be retrieved from the output tape using FIRM itself for further processing. However, certain procedures must be carried out before this processing can be done.

(1). Raw data tape copying:

All observations (which in general will be on several tapes) should first be copied onto a single "library" tape, which should itself be immediately duplicated so that there is a back-up tape with the same observations on it. The original tape should only be re-used after the copying procedure has been proven to be complete and successful. Checking can be done using the UBC routines TAPEDUMP or TAPESNIFF, or a user-written routine. The tape copying is done using UBC TAPECOPY.

Example

```
$MOUNT
RF0001 *T1* SIZE=5040 MODE=800
RF0002 *T2* SIZE=5040 MODE=800
RD0678 *LIB* SIZE=5040 VOL=P04071 RING=IN
$ENDFILE
$CONTROL *LIB* POSN=*25*
$CONTROL *T1* POSN=*2*
$RUN *TAPECOPY 0=*T1* 1=*LIB* PAR=RECORDS=251,NOREW
$RUN *TAPECOPY 0=*T2* 1=*LIB* PAR=FILES=1,RECORDS=109,NOREW
$CONTROL *LIB* WTM 2
```

Explanation : The case above is for two raw data tapes mounted on pseudo-devices *T1* and *T2*; the tape on *T1* has an end-of-file marker (filemark) at the beginning of the tape, followed by 251 records (each of 5040 bytes maximum length). The second tape, on *T2*, has a filemark at the beginning followed by 109 records. The library tape on *LIB*, has 24 files already written on it. Prior to the copying operation the tape is positioned at the beginning of the 25-th file. The 251 records of *T1* are written as the 25-th file on the library tape, and the contents of *T2* as the 26-th file. The filemark at the beginning of *T2* serves as the tape-mark between the 25-th and 26-th files on *T1*.

(2). Setting up the output tape status file.

Example

```
$CREATE TPSTATUS
$GET TPSTATUS
1.0,
1.5,   0   0  TPSTATUS: FIRM OUTPUT TAPE STATUS
$CREATE BACKUP
$COPY FROM TPSTATUS TO BACKUP
```

Explanation:

Lines 1.0 and 1.5 at least must exist in TPSTATUS prior to using the WRITE instruction in FIRM . A file (here called BACKUP) and a backup tape should be set up and periodically updated as TPSTATUS and the output tape data expand. Every time a new record is written on the output tape using FIRM , a line is added to TPSTATUS . In the "general example" near the beginning of this appendix the following line would be added to TPSTATUS :

```
__20xxxx__0__1__3_10NGC1000:RED:5 MIN:15 OCT
      | "new" record number
        =line number in TPSTATUS
```

The format is 2I4, 4I3, 14A2 where an array of twenty (20) halfwords is used as output for a single line of TPSTATUS.

Line 1.5 contains two integers in format 2I4, followed by up to 40 characters for the user's own labelling, e.g.

```
__50___0TPSTATUS: FIRM OUTPUT TAPE ON RF 0010
```

means that there are 50 records on the user's output tape

which is mounted from rack RF0010. The integer "0" indicates the tape is "open", i.e. Can be written onto. If this integer is set to 1, the operation WRITE will be inhibited.

<u>Note</u> : Lines in the output tape status file can be changed using UBC EDIT or UBC NEWEDIT.

Operations performed using FIRM

Operation		Function
APERTURE		Integrate over a square aperture in the field of view.
ADD		Add two images.
AI		Add constant to each element of an image.
AVERAGE		Read from tape and average two or more raw images.
COLUMN		Specify which columns "dead" or "live".
DIVIDE		Divide an image by another.
ELLIPSE		Generate a model ellipsoidal distribution or generate a circular aperture.
END		End processing and exit to MTS.
EXAMINE	AVERAGE	Print averages and extreme values,
	LABELS	print labels,
	HIST	plot a histogram, or
	CATLG	print the output file catalogue.
FT		Smoothing and/or shifting via the FFT.
GRAPH		Graph the value at each element of one picture versus the value of each corresponding element of a second picture.
INT		Convert magnitudes to intensity.
LABEL		Label a picture already in core memory.
LOAD		Read a raw data record from magnetic tape and load into core.
MAG		Convert intensity into magnitudes.
MI		Multiply each element of picture by constant.

MOVE	Move an image into a different array in core. Six arrays are available. Optionally, registration of images is performed using bi-linear interpolation.
MULT	Multiply two images.
PLOT	Plot a CALCOMP or printer contour map of an image. Print closed contour centroids and areas.
PRINT	Print the contents of an image array using the line printer.
RETRIEVE	Read back a reduced image from the output tape.
ROW	Define dead or live rows.
SECTION	Plot a graph of the cross-section of an image along a straight line or along an elliptical locus.
SHIFT	(Synonym for MOVE)
SMOOTH	Convolve a picture with a conical filtering profile.
STAR	Compute a Gaussian "star image" intensity distribution.
SUB	Subtract an image from another image.
VIEW	Print a 10x10 matrix of numbers corresponding to a 50x50 image averaged in 5x5 blocks.
WRITE	Write an image as a record on the output tape. Enter label into catalogue.
YY	An operation to be defined by the user.

Summary of FIRM Operations

Input/Output

```
LOAD IA, {FILE II} RECORD II
WRITE IA
RETRIEVE IA, REC II
AVE IA, {FILE II} REC II,JJ{,KK}
VIEW IA,{X.X}
APERTURE IA, NSIZE=II
PRINT IA,{X.X}
PLOT IA,[NCONT=II, INC=X.X],{MIN=X.X,MAX=X.X}
GRAPH IB,IA {MINY=X.X,MINX=Y.Y}
EXAMINE [ LABELS,AVERAGES,HIST,CATLG ] {IA IB}
SECTION IA, MODE=[L,E,ED], {X0=X.X,Y0=X.X,
            A=X.X,EPS=X.X,B=I, DELTA=X.X,GAMMA=X.X}
```

Internal operations and manipulations.

```
MOVE IA,IB {X1=X.X, Y1=X.X, X2=X.X, Y2=X.X,
          DX=X.X, DY=X.X}
LABEL IA,' Characters '
ADD IA,IB
AI IA,X.X
SUB IA,IB
DIV IA,IB
MULT IA,IB
```

```
MI IA,X.X

MAG IA, {X.X}

INT IA

ROW I,K I,K ...

APE IA, N=II

FT IA, {INV=±II, ASEE=X.X, DX=X.X, DY=X.X}

COL I,K I,K ...

SMOOTH IA

SHIFT ...   ( same as MOVE ).
```

Model distributions.

```
STAR IA,MODE=[NEW,ADD], X0=X.X, Y0=X.X, DIA=X.X,
        [INT=X.X,I0=X.X] {$}
ELLIPSE IA,MODEL=[KING,GEN,DEVAU,XPO], X0=X.X,
            Y0=X.X, {EPS=X.X,DELTA=X.X,} A=X.X,B=X.X,
            {C=X.X,GAMMA=X.X} {$}
```

Termination.

```
END
```

ADD

Prototype:

ADD IA,IB

Action:

Add image in array IB to image in array IA, element by element. The result is stored in array IA.

Examples:

ADD 3,1

AD 3,1

AI

Prototype:

AI IA, X.X{,NOISE}

Action:

Add "immediate" constant X.X to every element of image in array IA. If 'NOISE' is specified, a normal distribution simulated noise, with mean value zero, is added. The RMS or sigma value is then X.X.

Examples:

AI 2, 5.6

AI 3, -100.

AI 4, 3.0 NOISE

Note: This instruction is also used to subtract a constant.

APERTURE

Prototype:

APERTURE IA,NSIZE=II

Action:

To use the 2-D detector as a single-channel photometer with a square aperture NSIZE x NSIZE pixels in area. The square "aperture" is centred on the centroid of the intensity distribution with values greater than 10% of the maximum value in the array. The area outside the aperture is used as a background (sky), to be scaled and subtracted from the sum of intensities in the aperture. The aperture is clipped and scaled appropriately if too near an edge.

N.B. $1 \leq$ NSIZE < 50,
with NSIZE odd , for the RETICON RA50x50.

Examples:

APE 2,N=21

AVERAGE

Prototype:

AVERAGE IA, {FILE NN} REC II,JJ{,KK}

Action:

Average raw data records II to JJ in file NN, with increment KK between records, in the same sense as the FORTRAN DO instruction:

DO ... I=II,JJ,KK

(The default of KK is 1; NN defaults to the currently active input raw data file, declared in an earlier AVERAGE or LOAD).

The result of the averaging is stored in array IA.

Examples:

AVE 1, FILE 5 REC 10, 20, 2

AVE 3, REC 6,10

COLUMN and ROW

Prototype:

COLUMN I1,K I2,K ...

ROW J1,K J2,K ...

Action:

Columns In or rows Jn are "killed" (K=0) or "brought back to life" (K=1). All rows and columns are "live" at the start of the computer run, and their status can be changed during processing.

Examples:

```
ROW 1,0 2,0 50,0
COL 1,0 50,0
...
...
...
ROW 2,1
COL 2,0 3,0 4,0 50,1
```

Note: This instruction is needed to exclude faulty rows and columns, and to allow for clipping around the borders when image registration is performed.

DIVIDE

Prototype:

DIVIDE IA,IB

Action:

Divide image in array IA by image in array IB. The result is stored in array IA. Elements divided by zero are set to zero, and a warning message is printed.

Examples:

DIV 2,3

ELLIPSE

Prototype:

ELLIPSE IA,MODEL=[K,G,D,X,A],

{X0=X.X,Y0=X.X,EPS=X.X,DELTA=X.X,A=X.X,B=X.X,C=X.X,GAMMA=X.X}

Action:

Compute surface brightness distribution with elliptical isophotes:

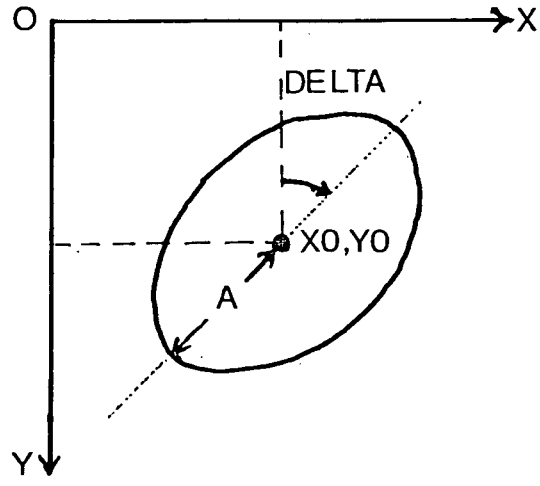

Coordinate System

P = (X0,Y0) = centre of distribution.

= DELTA = position angle of major axis

EPS = ellipticity of isophotes = 1 - b/a

A,B,C,GAMMA = parameters for model distributions.

The MODEL parameter must come first in the list.

Examples:

```
ELL 1,M=A X0=25.8,Y0=30.1 A=10.0 $
```

This produces a circular aperture. The '$' can be used to terminate the list, but should not be necessary unless most of the card is filled up.

MODEL parameter:

K : A simple King model is computed:

$$I(x,y) = \frac{A}{1 + \frac{a^2}{B^2}},$$

where a = semi-major axis of ellipse.

G : A generalized Hubble-law model is computed:

$$I(x,y) = \frac{A}{1 + Ba + Ca^2 + GAMMA\,a^3}.$$

D : A de Vaucouleurs model is computed:

$$\log_{10} I(x,y) = A + Ba^{1/4}$$

X : An exponential model is computed:

$$I(x,y) = A \exp\left(-\frac{a}{B}\right).$$

A : A circular aperture is computed:

$I(x,y) = 1.0$ if $\sqrt{x^2+y^2} \leq A$,

$= 0.$ If $\sqrt{x^2+y^2} > A$.

EXAMINE

Prototype:

EXAMINE [AVERAGES,LABELS,HIST,CATLG] {II} {JJ}

Action:

Print:

AVERAGES : averages, maxima and minima, or,

LABELS : array labels, or,

HIST : a histogram or histograms, or,

CATLG : list the output tape status file,

for arrays II to JJ inclusive. All arrays are included if no array index at all specified. Only II specified if a single array is to be considered.

Examples:

EX AVE 1 3

EX AVE

EX HIST 4

EX LABELS

FT

Prototype:

FT IA, {INV=±I, ASEE=X.X, DX=X.X, DY=X.X, SIGMA=X.X}

Action:

Transform array IA using the discrete Fourier transform routine FOUR2 (see UBC FOURT). If INV ≥ -1 (default = 0), filter using Gaussian with equivalent "seeing" diameter ASEE (in diode spacing units). If:

$$-6 \leq INV \leq -2,$$

a 50 x 50 subset of the absolute values of the 64 x 64 discrete Fourier transform is stored in array |INV| prior to filtering. The 32 by 32 subset with one corner at the first element is the square root of the power spectrum of the image.

The transform is inverted back into real space and stored in array IA.

If SIGMA is specified, Wiener filtering is performed, with a Gaussian instrumental profile of diameter ASEE and noise level SIGMA.

Examples:

FT 2, ASEE=2.7, DX=-3.6, DY=1.1

Note: the crude Wiener filtering option has not been very successful. More development is needed.

GRAPH

Prototype:

GRAPH IY,IX {MINY=X.X,MINX=X.X}

Action:

Plot a scatter diagram of the values of elements in array IY versus the values of corresponding elements in IY.

Parameters:

MINY = (optional) minimum value of elements in array IY to be included.

MINX = (optional) minimum value of elements in array IX to be plotted.

Examples:

GRAPH 2,3 MINY=20.0, MINX=100.

Caution: Choose minima so that the plotting time will not be excessive due to too many points being included. Beware of holes being drilled by the plotter pen !

INT

Prototype:

INT IA

Action:

The image in array IA is converted from magnitude measure to intensity measure. A warning is printed if the image has not been previously converted to magnitude measure.

Examples:

INT 5

LABEL

Prototype:

LABEL IA,' characters '

Action:

Array IA is labelled with up to 28 characters (excluding apostrophes).

Examples:

LABEL 2,'NGC 5914: RED: 5 MIN.'

Note: Original record number and file number are preserved in the header of the label (see instruction LOAD for a description). The apostrophes must be used if there are blanks in the label

LOAD

Prototype:

LOAD IA,{FILE I} RECORD J

Action:

Record J in file I of tape (FORTRAN unit 3) is loaded (read) into array IA.

Examples:

LOAD 2,FILE 11 RECORD 29

LO 2, F 11 R 3

This causes record 29 in file 11 to be loaded into array 2. The file is on the input (tape) unit 3, with 5040 bytes of data per record, consisting of the following: 6 halfword integers, 28 characters of labelling information, and 2500 halfword (2 byte) integers of raw data from the RETICON system:

NREC	= no. Of record in file.
(NEWREC)	= (unused) : space for output record number.
(command)	= (unused on 7/16) : command bits.
OBJECT	= object index (set during observation).
FILTER	= filter (set during observation).
(file no.)	= (unused) : file no. since start of observing.

(LABEL)	= (unused) : characters for label, set using FIRM . 28 bytes.
ARRAY	= data array. 2500 halfwords.

LOAD 2,REC 29

Same as first example, but FILE assumed to be the <u>current file number</u>, set previously using LOAD or AVE.

MAG

Prototype:

MAG IA,{X.X}

Action:

Convert image in array IA to magnitude measure, using the equation:

$$m(x,y) = -2.5\log I(x,y)$$

The optional parameter X.X is the minimum allowed value for the intensity. The default minimum is 0.001. Intensities below the minimum are converted to zero magnitude. Intensities should be scaled or offset before using this instruction if very small or negative values are present.

Examples:

MAG 2

Note: The third integer of the six label integers for array IA is set to 1 to serve as a flag.

MI

Prototype:

MI IA, X.X

Action:

Multiply image in array IA by constant X.X.

Examples:

MI 3, 10.5

MI 3, 0.995

Note: there is no corresponding divide by constant instruction, therefore multiply by the reciprocal.

MOVE

Prototype:

MOVE IA,IB { X1=X.X, Y1=X.X,X2=X.X, Y2=X.X }

or MOVE IA,IB DX=X.X, DY=X.X

Action:

Move data in array IB into array IA without destroying contents of array IB. If the parameters in curly brackets are specified, the picture is moved by interpolation, so that old reference point (X1,Y1) corresponds to the new reference point (X2,Y2). Alternatively one can specify DX, DY where:

DX = X2 - X1

DY = Y2 - Y1

(SHIFT and MOVE are equivalent).

Examples:

```
MOVE 4,2
SHIFT 4,2
MOVE 4,2 DX=0.32,DY=5.1
MOVE 4,2 X1=20.01,X2=20.33,Y1=24.9,Y2=30.
```

Note: The Fourier Transform command FT can be used to move an image using the Shift Theorem. In comparison, MOVE/SHIFT uses bilinear interpolation. The Fourier method should normally be used unless there are very sharp "spikes" in the image due to "hot" diodes, etc.

MULTIPLY

Prototype:

MULTIPLY IA,IB

Action:

Multiply image in array IA by image in array IB. Store result in array IA.

Examples:

MULT 3, 2

PLOT

Prototype:

PLOT IA,[NCONT=I,INC=X.X] {,MIN=X.X,MAX=X.X}

Action:

To produce a contour plot of the image in array IA. The parameters are as follows:

NCONT = number of contour levels.

INC = increment between contour levels.

MIN = minimum contour level to be plotted

MAX = maximum contour level to be plotted.

Examples:

```
PLOT 5,NCONT=20,MIN=10.0
PL 5 NC=20 MIN=10
PLOT 2,INC=10.0 MAX=120.
PLOT 1,NCONT=30, MAX=120., MIN=10.
```

Notes: If INC is specified, the contours are not labelled (i.e. use INC as a non-labelling option).

If MIN, MAX, INC or any combination of them not specified, the corresponding values are automatically computed using the minimum, maximum values found in the array. The intensity increment between contours is computed using these values and NCONT if INC not specified.

N.B.: Negative values are not permitted for contour levels. Offset or multiply appropriately before plotting, or specify the MIN option.

PRINT

Prototype:

PRINT IA {, X.X}

Action:

The 50 x 50 image is printed out as four consecutive pages on the line printer, each page consisting of a 25 x 25 quadrant of the image. The order is : top left, bottom left, top right, bottom right. The original record number (if any) is printed along the border, with an asterisk on each line. Each element is in format I5.

Each element is multiplied by a scale factor X.X for printing out. The scale factor allows small numbers to be scaled up, and vice versa, before rounding to integer form. If omitted or zero, the default value of 1.0 is assumed. Elements rounded to zero appear as blanks.

Examples:

```
PRINT 5, 10.0
PR 5
PR 5 100
PR 2 0.001
```

RETRIEVE

Prototype:

RETRIEVE IA,RECORD I

Action:

Record I on the output tape (FORTRAN unit 4) is retrieved (read) and loaded into array IA. The labels in the tape status file and on the tape are printed out.

Examples:

RETRIEVE 2,RECORD 50

RE 2,REC 50

RETR 2,R 50

ROW

See instruction COLUMN.

SECTION

Prototype:

SECTION IA,MODE=[L,E,ED], {

XO=X.X,YO=X.X,A=X.X,B=X,DELTA=X.X,EPS=X.X,GAMMA=X.X }

Action:

MODE=L

Produce graph of values along a straight line inclined at DELTA (in degrees) to the vertical axis i.e. a cross-section plot, passing through the point XO,YO. Parameter B defines the type of plot.

MODE=E

Produce graph of values as a function of polar angle along an ellipse centred at XO,YO, with ellipticity EPS= 1 - b/a, and orientation DELTA . The semi-major axis is A pixel units long.

MODE=ED

Same as MODE=E, except that the polar angle is defined in a disk inclined at GAMMA degrees. 0° is face-on. EPS need not be specified, since the locus in the image plane is the projection of a circle in the plane of the disk.

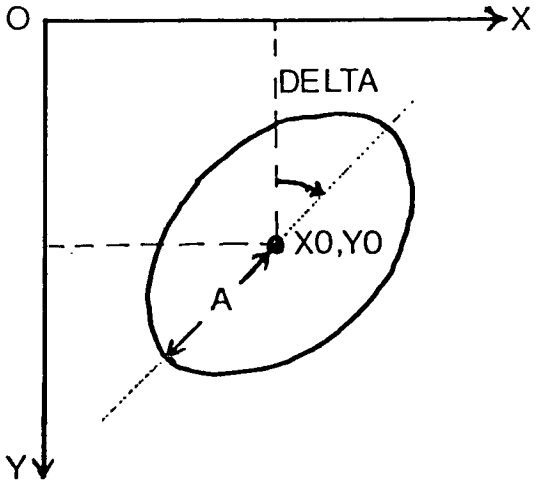

Coordinate Definition

<u>Plot types in MODE=L :</u>

B = 0	(default: data in array IA is plotted directly against distance along the line.
B = 1	King plot (1/I <u>vs</u> r^2)
B = 2	Hubble plot (1/SQRT(I) <u>vs</u> r)
B = 3	de Vaucouleurs plot ($\log_{10}$ I <u>vs</u> $r^{1/4}$)
B = 4	Gaussian plot ($\log_e$I <u>vs</u> r^2)
B = 5	log-log plot ($\log_{10}$ I <u>vs</u> log |r|)

<u>Examples:</u>

```
SECTION 1,MODE=L,X0=25.5,Y0=33.1,
                B=3,DELTA=31.0

SECTION 2,MODE=E X0=25.5,Y0=33.1,
                A=10.0,DELTA=31.0 EPS=0.35

SECTION 2, MODE=ED X0=25.5, Y0=33.1,
                A=10.0 DELTA=31.0 GAMMA=60.
```

SMOOTH

Prototype:

SMOOTH IA

Action:

Smooth image in array IA using a conical convolving filter of base diameter 4.0 diode units.

Examples:

SM 2

Note: The Gaussian smoothing filter in the instruction FT has a variable effective diameter ASEE, and should normally be used rather than SMOOTH . See Chapter 3 of thesis for filter definition.

STAR

Prototype:

STAR IA,MODE=[NEW,ADD],X0=X.X,Y0=X.X,
[INT=X.X,I0=X.X],DIA=X.X

Action:

Compute a Gaussian circular star image at position (X0,Y0), with diameter DIA and integrated intensity INT or central intensity I0. The MODE parameter specifies whether the array IA is to be zeroed (NEW) or not (ADD) prior to computing the star image. The equation is:

$$I(x,y) = I0*\exp\{-4(x^2+y^2)/DIA^2\}$$

Examples:

```
STAR 2,MODE=ADD X0=26.8 Y0=29.2 I0=930.0 DIA=3.5
ST 3 M=N X0=30.1 INT=2500.  DIA=4.0 Y0=5.5
```

SUBTRACT

Prototype:

SUBTRACT IA,IB

Action:

Subtract image in array IB from image in array IA. Result stored in array IA.

Examples:

SUB 1,4

VIEW

Prototype:

VIEW IA {,X.X}

Action:

The 50x50 image in array IA is averaged into 5x5 sub-blocks and printed as a 10x10 matrix. Dead rows and columns are not included in the averaging process. The averages are multiplied by X.X before being printed as rounded integers. If omitted, the default value of X.X is 1.0.

Examples:

```
VIEW 2,100.
VI 2, 100
VIEW 5
```

WRITE

Prototype:

WRITE IA

Action:

Write contents of array IA , with its label, as the next record on the output tape (FORTRAN unit 4).

The label, including the new output record number, is also written into the MTS line file used as the status file for the output tape. (The status file is FORTRAN unit 2). The output tape is automatically positioned by FIRM using the output record counter in line 1.5 of the tape status file. The MTS line-number of the new line is the same as the new record number, and the output record counter in line 1.5 is incremented by 1. (See section on tape procedures and setting up). The written record can be subsequently read back into core using the instruction RETRIEVE

Examples:

WRITE 3

APPENDIX II

DATA TAPES

Raw Data Tapes

RD0678	VOL=P04011	primary tape
RD0677	VOL=P04071	backup duplicate

Output Tapes

RD0906	VOL=P06287	primary tape
RB0908	VOL=P05469	backup
RD0907	VOL=P06263	M15(NGC7078) output
RB0909	VOL=P05466	programmes (SM71)

These are permanent rack numbers for tapes at the Computing Centre at UBC.

Summary of Data Tape Contents

on Next Page

Summary of Data Tape Contents

File	Date	Telescope	Objects Observed.
	1975		
1	-----	---	Null File: Tape Mark.
2	May 9	12"	M87 M63 M13 Stars M57
3	Jun27	72"	Star Sky Dark current
4	Jun28	72"	Stars Sky
5	Nov 3	72"	Observing Programme
6	"	"	M31 Stars : Noisy
7	"	"	N2392 M31 Stars : Noisy
	1976		
8	Feb24	24"	Praesepe N2403 N2903 N4472 M51
9	Feb28	"	N4472 M101
10	Mar 6	"	M87 Star N3556 N4472 N3992
11	Mar 8	"	Star Praesepe N2903
12	"	"	N4472
13	Mar29	88"	Praesepe Stars(satd.) M94 M51
14	Apr 1	"	HR4708 N4258
15	"	"	Star M51 M13 N6441
16	"	"	Darks
17	Apr 2	"	Stars M51 N5195 : f/0.8
18	Apr 3	"	927 consecutive 20sec darks.
19	May 1	"	Dk & Flat Field
20	May 6	24"	Darks
21	"	"	Star N5824 N6441
22	May 7	"	Stars
23	"	"	Stars
24	May 7	"	Stars N5824 N6266 N6441 N6624 N6715
25	"	"	Darks
26	May 8	"	N5824 Stars N6093
28	"	"	N6864 Stars
29	"	"	Darks
30	Sep14	72"	N7027 M15 N7662 M31
31	Sep15	"	HD172323 N7027 M15 N7662
32	"	"	N7662 Sky F.F.
33	Oct16	12"	Defocussed Bright Stars
34	"	"	" " "
35	"	"	" " "
36	Oct17	"	" " "
37	Oct18	"	" " "
38	Mar30	88"	Praesepe stars M87 HR4708 M51